UNIVERSITÀ DEGLI STUDI DI NAPOLI "FEDERICO II"

Department of Pharmacy

In co-advisor with

the Autonomous University of Madrid

PhD in Pharmaceutical Science

XXXII cycle

"Protein dissection approach as a powerful tool to identify new potential drugs"

PhD student

Sara La Manna

Tutor

Dott. Daniela Marasco

Prof. Carmen Gomez-Guerrero

Coordinator: Prof. Maria Valeria D'Auria

I. SUMMARY

Protein-protein interactions (PPIs) play essential roles in biological processes: often proteins interact with each other to exert their functions creating a network of PPIs crucial in metabolism, as well as signaling mechanisms (interaction of messenger molecules, hormones, neurotransmitters and their cognate receptors) and gene expression (protein-DNA interactions). Alterations of these interactions are often at the basis of several pathologies, thus the identification of molecules able to modulate, inhibit or promote PPIs represents a powerful therapeutic approach. Furthermore, small protein domains or secondary structure motifs are often investigated to gain insights into global structure or/and to modulate interactions with external partners. In the last years, synthetic peptides capable to interfere with PPIs are receiving increasing attention. This study is focused on the design, functional and structural characterization of peptides covering active protein fragments that are employed as template to design peptidomimetics with improved drug-like properties. During this thesis, these topics were applied to two projects: i) the miniaturization of the multidomain protein Nucleophosmin 1 (NPM1) to unveil structural determinants of mutations associated with acute myeloid leukemia (AML) disease and ii) the development of new anti-inflammatory compounds as mimetics of suppressors of cytokine signaling (SOCS) proteins involved in the Janus kinase (JAK)/signal of activation (STAT) pathway.

NPM1 is a multifunctional protein involved in the pathogenesis of several human malignancies with peculiar mutations in AML. Its C-terminal domain (CTD) is endowed with a three-helix bundle in its wt form instead it is unfolded in AML mutated forms where the loss of NoLS (Nucleolar Localization Signal) causes an aberrant translocation of NPM1 to the cytosol (NPMc+). On the basis of previous investigations that unexpectedly exhibited a strong amyloid-aggregation propensity of several protein regions of the AML mutated CTD herein, to deepen the molecular mechanisms associated with AML misfolding and the leukemogenic potentials of AML mutations, biophysical features of several protein regions, were investigated. In detail the smallest amyloidogenic stretch of the entire NPM1 sequence encompassing region 264-272 demonstrated able to form amyloid aggregates through helical intermediate and a direct link between AML mutations and amyloidogenicity was assessed in the characterization of peptides covering the 3rd helix of the bundle in its AML mutated sequences. Amyloidogenic hot-spots, differently located into the entire

protein, exhibited cooperative aggregative mechanism when included in the polypeptide deriving from the connection of H2 and H3 in the type A mutated variant, H2MutA.

The employment of protein domains as template for the design of peptidomimetics as potential drugs was carried out in the design and characterization of mimetics compounds of SOCS proteins. In detail, for SOCS1 several analogues of the lead compound named PS5 were designed, structurally and functionally investigated both *in vitro* and *in vivo*. In this study some restricted cyclic peptides, bearing non-natural amino acids, revealed able to mimic SOCS1's biological functions. For SOCS3, the lack of previous studies prompted toward the investigation of linear peptides covering flat protein regions and chimeric sequences connecting not contiguous regions. The *in vitro* and cellular characterization of these compounds revealed, for the first time, that mimetics of SOCS3 can have powerful therapeutic application and pave the way to design macrocycles to inhibit the formation of JAK2/SOCS3 complex.

I. SOMMARIO

Le interazioni proteina-proteina (PPI) svolgono ruoli essenziali nei processi biologici: spesso le proteine interagiscono tra loro per esercitare le loro funzioni creando una rete di PPI cruciali nel metabolismo, nonché meccanismi di segnalazione (interazione di molecole messaggere, ormoni, neurotrasmettitori e loro recettori) ed espressione genica (interazioni proteina-DNA). Le alterazioni di queste interazioni sono spesso alla base di diverse patologie, quindi l'identificazione di molecole in grado di modulare, inibire o promuovere i PPI rappresenta un valido approccio terapeutico. Inoltre, vengono spesso studiati piccoli domini proteici o motivi di strutture secondarie per ottenere approfondimenti sulla struttura globale o/e per modulare le interazioni con partner esterni. Negli ultimi anni, i peptidi sintetici in grado di interferire con gli PPI stanno ricevendo crescente attenzione. Il presente studio è focalizzato sulla progettazione ecaratterizzazione funzionale e strutturale di peptidi derivanti da frammenti proteici funzionali utilizzati anche come strutture “template” per progettare peptidomimetici con proprieta’ piu’simili ai farmaci tradizionali. Sulla base di tali considerazioni,due progetti sono stati sviluppati: i) la miniaturizzazione della proteina multidominio Nucleofosmina 1 (NPM1) per studiare i determinanti strutturali delle mutazioni associate alla leucemia mieloide acuta (LMA) e ii) lo sviluppo di nuovi potenziali farmaci antinfiammatoriquali mimetici delle proteine soppressori dei meccanismi di segnalazione delle citochine (SOCS) coinvolti nella via JAK/STAT.

NPM1 è una proteina multifunzionale coinvolta nella patogenesi di diverse neoplasie umane con peculiari mutazioni nella LMA. Il suo dominio C-terminale (CTD) nella forma nativa è formato da tre eliche cheperde questa struttura terziaria nelle forme mutate di LMA in cui la perdita di NoLS (Segnale di Localizzazione Nucleolare) provoca una aberrante traslocazione di NPM1 nel citosol (NPMc+) . Sulla base di precedenti studi, che hanno inaspettatamente dimostrato una forte propensione all'aggregazione amiloide di diverse regioni proteiche del CTD mutato nellaLMA, nel presente studio, per approfondire i meccanismi molecolari associati al misfolding e i potenziali leucemogeni delle mutazioni LMA, sono state studiate le caratteristiche biofisiche di diverse regioni proteiche. In particolare, il più piccolo tratto amiloidogenico dell'intera sequenza NPM1 che comprende la regione 264-272 ha dimostrato di essere in grado di formare aggregati amiloidi attraverso intermedi elicoidali ed è stato valutato un legame diretto tra le mutazioniLMA e l’amiloidogenicità grazie alla caratterizzazione dei peptidi derivanti dalla 3^{a} elica di NPM1, nelle sue sequenze mutate. Inoltre hot spots amilodogenici hanno dimostrato un meccanismo

cooperativo di aggregazione quando inclusi nel polipeptide derivante dalla connessione di H2 e H3 nella variante mutata di tipo A, H2MutA.

L'impiego di domini proteici come modello per la progettazione di peptidomimetici come potenziali farmaci è stato utilizzato nella progettazione e nella caratterizzazione dei composti mimetici delle proteine SOCS. Nel dettaglio, per SOCS1 sono stati progettati diversi analoghi del peptide PS5 che sono stati studiati strutturalmente e funzionalmente sia *in vitro* che *in vivo*. Alcuni peptidi ciclici, contenenti aminoacidi non naturali, si sono rivelati in grado di mimare le funzioni biologiche di SOCS1. Per SOCS3, la mancanza di studi precedenti ha spinto verso lo studio di peptidi lineari che coprono regioni di proteine contigue e sequenze chimeriche che collegano regioni non contigue. La caratterizzazione in vitro e cellulare di questi composti ha rivelato, per la prima volta, che i mimetici del SOCS3 possono avere una potente applicazione terapeutica e aprire la strada alla progettazione di macrocicli per inibire la formazione del complesso JAK2/SOCS3.

I. RESUMEN

Las interacciones proteína-proteína (PPI) juegan un papel clave en los procesos biológicos: las proteínas interactúan entre sí para ejercer sus funciones creando una red fundamental de PPI en el metabolismo, así como mecanismos de señalización (interacción de moléculas mensajeras, hormonas, neurotransmisores y sus receptores) y expresión génica (interacciones proteína-ADN). Las alteraciones de estas interacciones son a menudo la base de diversas patologías, por lo tanto, la identificación de moléculas capaces de modular, inhibir o promover las IPP representa un enfoque terapéutico válido. Además, los pequeños dominios de proteínas o los motivos de estructura secundaria se estudian para obtener información sobre la estructura global o para modular las interacciones con otras moléculas. Durante los últimos años se ha prestado cada vez más atención a los péptidos sintéticos capaces de interferir con las IPP. Este estudio se centra en el diseño y la caracterización funcional y estructural de péptidos derivados de fragmentos de proteínas activas que se utilizan como modelo para desarrollar peptidomiméticos con propiedades similares a las de los fármacos. Sobre esta base, se han desarrollado dos proyectos: i) la miniaturización de la proteína multidominio Nucleofosmina 1 (NPM1) para estudiar los determinantes estructurales de las mutaciones asociadas con la leucemia mieloide aguda (LMA); y ii) el desarrollo de nuevos potenciales fármacos antiinflamatorios miméticos de las proteínas supresoras de la señal de citoquinas (SOCS) implicados en la vía JAK/STAT.

NPM1 es una proteína multifuncional involucrada en la patogénesis de varios tumores malignos humanos con mutaciones peculiares en la LMA. Su dominio C-terminal (CTD) está formado por tres hélices en su forma nativa mientras pierde esta conformación en las formas mutadas de LMA en las que la pérdida de NoLS (señal de localización nucleolar) provoca una translocación aberrante de NPM1 en el citosol (NPMc +). Con base en estudios previos que, inesperadamente, han demostrado una fuerte propensión a la agregación amiloide de diferentes regiones proteicas de CTD mutadas en la LMA, el presente estudio investigan los mecanismos moleculares asociados con el plegamiento incorrecto en la LMA y los posibles leucemógenos de las mutaciones de LMA, estudiando las características biofísicas de diferentes regiones proteicas. En particular, se ha demostrado que la región amiloidogénica más pequeña de toda la secuencia NPM1 que comprende la región 264-272 puede formar agregados amiloides a través de intermedios helicoidales, y se ha evaluado un enlace directo entre las mutaciones de LMA y la amiloidogenicidad gracias a la caracterización de los péptidos derivados de la tercera hélice de

NPM1, en sus secuencias mutadas. Además, los puntos cruciales para la amiloidogénesis han demostrado un mecanismo de agregación cooperativo cuando se incluye en el polipéptido derivado de la conexión de H2 y H3 en la variante mutada de tipo A, H2MutA.

El uso de dominios de proteínas como modelo para el diseño de peptidomiméticos como fármacos potenciales se ha implementado para el diseño y caracterización de los peptidos miméticos de las proteínas SOCS. En particular, se han diseñado varios análogos de péptidos PS5 para SOCS1, en los que se han estudiado propiedades estructurales y funcionales tanto *in vitro* como *in vivo*. Algunos péptidos cíclicos que contienen aminoácidos no naturales han demostrado ser capaces de imitar las funciones biológicas de SOCS1. En el caso de SOCS3, la falta de estudios previos ha impulsado nuestra investigación hacia el estudio de péptidos lineales que cubren regiones proteicas contiguas y secuencias quiméricas que conectan regiones no contiguas. La caracterización *in vitro* y celular de estos compuestos reveló, por primera vez, que los miméticos SOCS3 pueden tener una aplicación terapéutica poderosa y allanar el camino hacia el diseño de macrociclos para inhibir la formación del complejo JAK2/SOCS3.

II. INTRODUCTION

1. Protein-Protein Interactions

Cell homeostasis is controlled by a fine-tuned network of protein-protein interactions (PPIs)[1]. PPIs are specific physical contacts established between two or more proteins for carried outspecific biological activity (**Figure 1**). Theyregulate either developmental andmetabolic processesin which, for example, enzymes interact each other to produce small compounds or other macromolecules such as polysaccharides and modulate cell-cell interactions[2]. PPIs in muscle contraction exert a major role:here myosin filaments act as molecular motors and the binding to actin enables filament sliding and the transport across membrane where a protein can be located close to another protein[3].

Based on their structural and functional properties, PPIs are classified in several groups: for the stability they can be called as obligate or nonobligate,for the persistence, they may be transient or permanent and depending upon their interaction surface, they may be homo-oligomeric and/or hetero-oligomeric[4]. A PPI may be generated by a combination of these three features; for example, a stable protein complex can be due to a permanent interaction among the proteins while, a transient interaction can be involved in a signaling pathway[5].

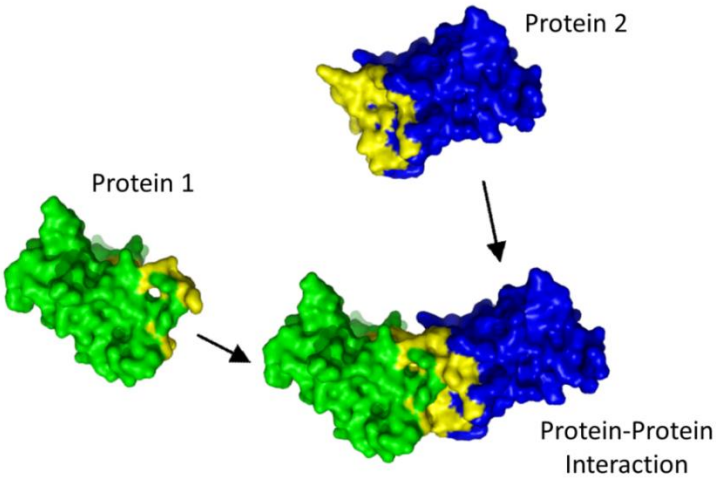

Figure 1. Schematic representation of the formation of a protein-protein interaction (PPI). Adapted from Fischer et al [6]

It is well known that over 80% of the proteins not perform their functions, in a living cell, alone but in complexes and many proteins involved in the same cellular processes are repeatedly found

to be interacting with each other[7]. For this reason, the function of an unknown protein could be predicted by its interactions with a protein, whose function is already known. Moreover, the study of PPIs could also help to understand the molecular mechanism of cellular processes[8].

PPIs have many properties, and the crucial ones are: i) ability to modify the kinetic properties of enzymes; ii) capacity to suppress or activate a protein; iii) regulatory role in upstream or downstream of a specific pathway; iv) capability to allow substrate channeling; v) ability to modify the specificity of a protein for its substrate by changing binding partners; and vi) to create a new binding site for small molecules[3].

It has been predicted that the human interactome includes between 130 000 and 600 000 PPIs[9].In recent years, thanks to different techniques such as mass spectrometry, phage display and protein microarray, PPIs data have been increased. All these techniques are largely useful to building detailed PPI networks[10]. And the knowledge of PPI networks is crucial since their deregulation is often associated with several pathology in principle each PPI sites could be a potential pharmacological target covering a very large range of illnesses[11].

Actually, there are various biological database that collect predicted and known PPIs and their analysis can open new directions for future experimental investigation and provide cross-species predictions for efficient interaction mapping[12]. In **Figure 2** is reported Nucleophosmin (NPM) 1 interaction network obtained from STRING (Search Tool for the Retrieval of Interacting Genes/Proteins) program.

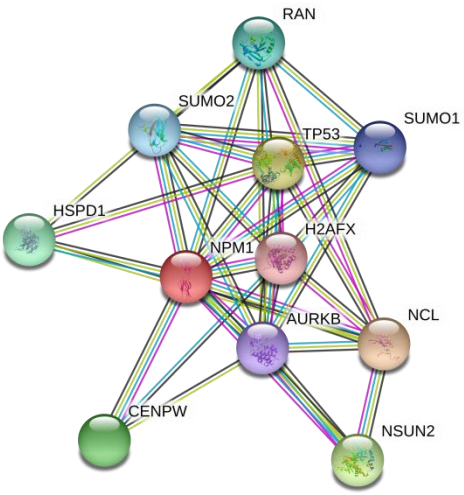

Figure 2. Schematic representation of PIN (protein interaction networks) of NPM1 protein (human).

The importance of PPIs in cell signaling represent the basis of intense research aiming to generate new pharmacological tools to regulate cellular responses[13]. In particular, the inhibition of molecular mechanisms underlying PPIs is a promising strategy for the control of their biological functions. This approach requires the availability of molecules capable of mimicking binding and/or functional sites of proteins and able to interfere with PPIs[14].

1.1. Interfering Peptides

In the past, many small molecules were developed to target intracellular PPIs; however, these interactions involved unique and specific protein surfaces that could not be mimicked by small compounds[15-16]. In this perspective, synthetic or natural peptides capable of interfering with PPIs, so-called interfering peptides (IPs), are receiving increasing attention (**Figure 3**)[17].

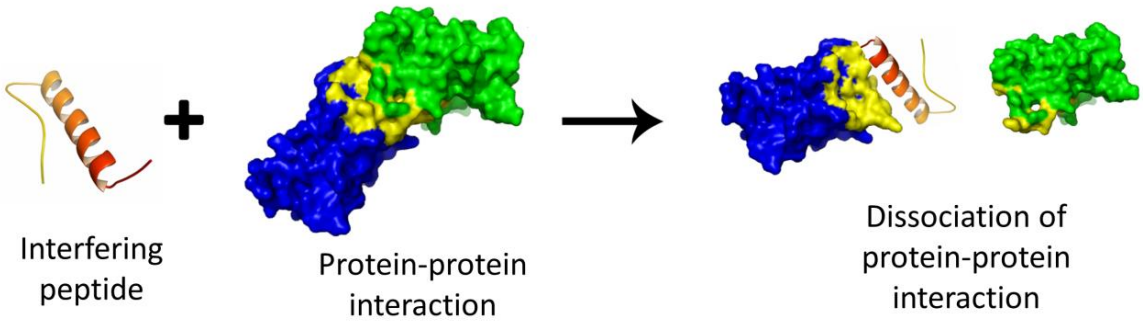

Figure 3. Schematic representation of the effect of an interfering peptide targeting a protein-protein interaction. Adapted from Fischer et al [6]

Recent advances in peptide and peptidomimetic synthesis are generating renewed enthusiasm in the use of peptides as therapeutics in vaccine's development, angiogenesis-related and auto-immune diseases, diabetes and neuroprotection[18-19]. The advantages of peptide-based therapeutics derive from peptide's underlying physics: the chemistry and modularity of amino acids combined with the physical and chemical nature of the amide bond make peptides unique since also the nature has solved numerous physiological and pharmacological problems using them [20]. Peptides offer greater efficacy, selectivity and specificity with respect to small organic molecules; further they are endowed with predictable and relatively low manufacturing costs,easy synthesis and storage, low toxicity and reduced antigenicity[21]. Compared with proteins and antibodies, peptides can further penetrate into tissues owing to their smaller size. Therapeutic peptides are generally less immunogenic than recombinant proteins and antibodies, and their degradation products are amino acids, thus minimizing the risks of systemic toxicity[22-24].

In cases of availability of the protein-protein complex structure, it is possible to identify few hot-spots involving residues situated at the PPI interfaces, responsible for the interaction between the partners[25]. When the structure of the proteins is available but not that of the complex, the PEPscan technology could be used. It is possible to scan entire sequence of one of the partners split as overlapping peptides, usually 15 amino acids long (peptide scan). Peptide sequences are then screened for their ability to compete with the formation of PPIs[26].Alternatively, to identify *de novo* bioactive peptides many combinatorial strategies have been developed. The latter approach is based on compound libraries, which are valuable tools for the investigation and characterization of unknown mechanisms of protein-ligand interactions related to newly discovered proteins with potential biomedical relevance[27].Another approach is the phage display: here filamentous bacteriophages able to express peptides and to expose them on their surface are investigated [28]. The produced peptides are tested for their affinity to bind a specific target and/or their ability to interfere with cellular mechanisms such as proliferation and development[29]. Also, computational methods are used to predict the binding mode of a peptide to the protein target: the ‘‘peptide docking’’ provides the most probable peptide bound conformation in complex with the target protein. This approach can be applied to guide the optimization of peptide sequences and simultaneously its conformation[30].

The use of peptides to target PPI interfaces has several advantages including high selectivity, but the conversion of a peptide lead to a commercial drug is a very challenging and time consuming process since they have their own limitations as low *in vivo* stability, poor pharmacokinetics and bioavailability and poor ability to cross physiological barriers because of their general hydrophilicity and high *in vivo* clearance[31]. To overcome such limitations, one way is to constrain the secondary structure of linear peptides by cyclization[32]. This method is principally a mean to fix peptide structure in the bioactive conformation, thereby increasing its binding efficiency and biological activity. Furthermore, cyclization can also improve resistance to proteases degradation and cell penetrability. Other approaches involved N-substitution, lactam cyclization or aza-amino scanning procedures[33].

At present, several IPs have been in *vitro* and in *vivo* validated and several are already in clinical stage.One of these is DPT C9 h, a peptide able to impair the interaction between the cysteine protease caspase 9 and the protein phosphatase 2A (PP2A), a serine/threonine phosphatase active in triple-negative breast cancer (TNBC) with antiproliferative effect[34].Another one is a

peptide derived from FOXO4 able tocompete with the formation of PPIs between transcription factor forkhead box O4 (FOXO4) and tumor protein p53, thus regulating cellular senescence [35].

In conclusion, PPIs represent a great promise as therapeutic targets and IPs as potential drugs. Progress on peptide administration, stability and delivery are encouraging the interest in peptide drug development Moreover, during the study of PPIs, for example by carrying out a protein dissection, could help us not only to identify new potential therapeutic targets but also to fully understand the molecular mechanisms necessary for proteins to perform their biological functions.

Secondary structure motifs and small protein domains can act as building blocks that are isolated and investigated to gain insights into protein global structure but can also modulate interactions with external partners. Most progresses in this field were due to the employment of synthetic peptides. Fragmentation of folded proteins helps to isolate shorter polypeptides with preserved secondary and tertiary structures or exhibit novel and unexpected conformational features. Such fragments can be used as probes for structural studies and to better delineate the structural features of PPI network [36]

This thesis is focused on these two aspects of investigations on synthetic peptides covering protein fragments: i) miniaturization of multidomain proteins to unveil structural determinants of diseases related mutations; and ii) design of mimetics of protein domains mainly involved in PPIs with improved drug-like features. Therefore, two basic case studies were investigated: Nucleophosmin 1 and SOCS proteins.

2. NUCLEOPHOSMIN 1 PROTEIN

Nucleophosmin 1 (NPM1, also known as B23.1, No38 and numatrin) is an abundant multifunctional protein belonging to the nucleoplasmin family of nuclear chaperone that constantly shuttles between the nucleus and cytoplasm [37-38]. The majority of NPM1 functions are played through different PPI with a variety of protein partners[39]. It is present in high quantities in the granular region of nuclei of proliferating cells, taking part in rRNA maturation and it is essential for embryonic development. NPM1 regulates centrosome duplication, ribosome biogenesis, apoptosis and the stability of many tumor-suppressors such as p53 and cyclin-dependent kinase inhibitor 2 A/p14ARF[40-41]. The human NPM1 gene is mapped on chromosome 5q35 and is composed of 12 exons encoding for three alternatively spliced nucleophosmin isoforms: B23.1, the best characterized isoform, results in a 294 amino acids protein; B23.2 and B23.3 are splicing variants that lack the C-terminal 35aa and a 29aa segment (residues 195-223) in the basic region, respectively [42]. Structurally, NPM1 is characterized by a modular organization in which three almost structural and functional domains can be distinct as shown in **Figure 4A** [43-44].

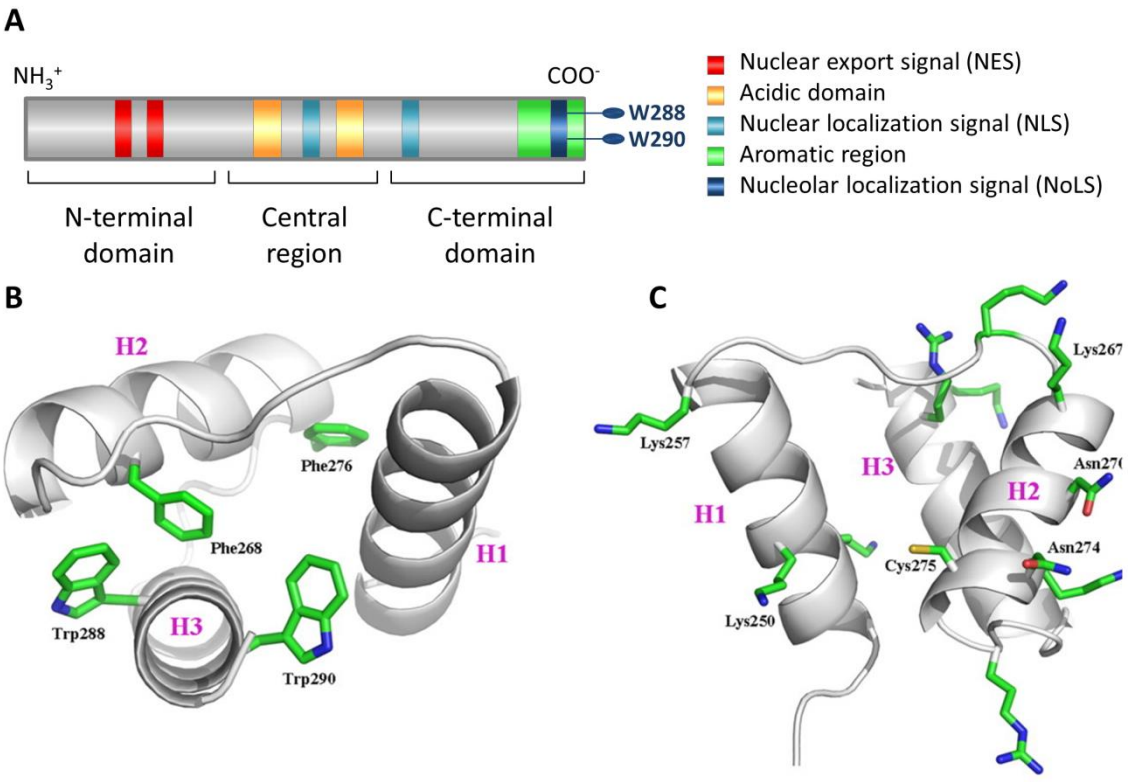

Figure 4. **A)** Modular structure and functional domains of NPM1 protein; **B-C)** NMR structure of NPM1 C-terminal domain. Adapted from Federici et al [45]

The N-terminal domain is the oligomerization domain mainly involved in its chaperone activity, which extends for approximately 100 residues and displays an eight-stranded β-barrel fold. It is a hydrophobic domain, containing two nuclear export signals (NES) [45]. These motifs bear closely spaced leucines along with other hydrophobic amino acids, and promote translocation from nucleus to cytoplasm through interaction with CRM1 export protein. The hydrophobic N-terminus also contains regions responsible for self-oligomerization in which five monomers form a pentamer, helping to drive NPM1 to the nucleolus [46].

The middle region is an IDR (Intrinsically Disordered Region), characterized by the presence of two acidic domains which play a role in histone binding [47]. This region also contains part of a bipartite Nuclear Localization Signal (NLS), contributing to NPM1 shuttling from cytoplasm to nucleus [48]. Deletion of either N-terminus or central region results in impaired chaperone activity, thus suggesting that both regions are essential for it [49]. Interestingly, it was demonstrated that NPM1 contribute to the liquid-like properties of nucleoli. Indeed, it was demonstrated that NPM1 thanks by its IDR, is able to independently undergo liquid-liquid phase separation (LLPS) with nucleolar proteins presenting arginine-rich linear motifs (R-motifs) and ribosomal RNA (rRNA)[50-52].

The C-terminal domain (CTD), in its wild-type (wt) form, is formed by a three-helix bundle in which helices H1 and H3 are almost coaxial, whereas the connecting helix H2 is tilted, by ~45° with respect to other helices and is stabilized by a small hydrophobic core formed by four aromatic residues: Phe268, Phe276, Trp288 and Trp290 as shown in **Figure 4B** [53]. Several lysine and asparagines residues (Lys250, Lys257, Lys267, Asn270, Asn274, Cys275) are found in the three-helix bundle, distributed throughout its length, and contribute to the marked basicity of this domain (**Figure 4C**). The CTD, along with its N-terminal basic regions are involved in nucleic acid binding and ribonuclease activity [48, 54]. Interestingly, in the third helix of the bundle, H3, of the C-terminal region, appears an aromatic short stretch including tryptophans 288 and 290 that formed a nucleolar localization signal (NoLS), critical for NPM1 localization into nucleolus[53]. This is a unique NoLS because, most of the identified NoLS are formed by sequence motives enriched in consecutive basic[55]while in this case it is formed by two aromatic aminoacids. This function was shown by observing that deletion of the NPM1 C-terminal 288-294 fragment which includes the two tryptophans as well as substitution of both tryptophans to alanine caused the delocalization of the protein in the nucleoplasm [56].

The presence of several nuclear and nucleolar import/export signals in NPM1 sequence indicates the prominent role of NPM1 in nuclear or nucleolar protein import; indeed, it is involved in several biologic processes, such as ribosome biogenesis, maintenance of the stability of the genome, in the duplication of centrosome, tumor suppression and nucleolar stress response [57]. NPM1 also has been implicated in the apoptotic response to stress and oncogenic stimuli, such as DNA damage and hypoxia and it can modulate the activity and stability of crucial tumor-suppressor proteins such as p53 [58-60].

2.1. NPM1 mutations in Acute Myeloid Leukemia

Much of the interest in NPM1 protein arises from its relevance in human malignancies [47, 54]. Indeed, it is frequently overexpressed in solid tumors and is the target of several chromosomal translocations in hematologic neoplasms. Notably, NPM1 was the most frequently mutated gene in acute myeloid leukemia (AML) patients; in particular, specific mutations in the exon 12 of the NPM1 gene occur, accounting for approximately 65% of AML cases [61-64]. AML is a neoplasm of the myeloid blood cell line, characterized by the rapid growth of abnormal white blood cells that accumulate in the bone marrow and interfere with the production of normal blood cells. NPM1 mutations are always heterozygous and mutually exclusive with AML carrying recurrent genetic abnormalities. Mutations cluster in the terminal exon 12 of the NPM1 gene and consist in the duplication or insertion of small nucleotide stretches [63].

The reading frame of NPM1 is altered and this leads to a mutated protein that has a different sequence in the last seven residues and longer of four residues with respect to wt protein. In the most frequent case, mutation A, which accounts for about 75-80% of cases, both Trp288 and Trp290 are lost (mutants A-D), whereas in other mutants only Trp290 is replaced (mutant E, F) (**Table1**). The mutations A and D differ only in one base of the inserted tetra nucleotide that didn't change the amino acid sequence[63].

Table 1: Mutations at the CTD evidenced residues constituting new NES (red) and stop signal (blue). In green the two tryptophans, Trp288 and Trp290.

Mutant	Sequence	Protein
Wild-type	GATCTCTG. . . .GCAGT. . . .GGAGGAAGTCTCTTTAAGAAAATAG	^{286}DLWQWRKSL^{294}
Mutant A	GATCTCTGTCTGGCAGT. . . .GGAGGAAGTCTCTTTAAGAAAATAG	^{286}DLCLAVEEVSLRK^{298}
Mutant B	GATCTCTGCATGGCAGT. . . .GGAGGAAGTCTCTTTAAGAAAATAG	^{286}DLCMAVEEVSLRK^{298}
Mutant C	GATCTCTGCGTGGCAGT. . . .GGAGGAAGTCTCTTTAAGAAAATAG	^{286}DLCVAVEEVSLRK^{298}
Mutant D	GATCTCTGCCTGGCAGT. . . .GGAGGAAGTCTCTTTAAGAAAATAG	^{286}DLCLAVEEVSLRK^{298}
Mutant E	GATCTCTG. . . .GCAGTCTCTTGCCCAAGTCTCTTTAAGAAAATAG	^{286}DLWQSLAQVSLRK^{298}
Mutant F	GATCTCTG. . . .GCAGTCCCTGGAGAAAGTCTCTTTAAGAAAATAG	^{286}DLWQSLEKVSLRK^{298}

It has been shown that loss of these residues, that are crucial elements of the hydrophobic core of the CTD, impairs the folding of the domain [53] and hampers its ability for nucleic acids recognition [45, 47, 53, 65]. However, in all instances the NoLS is compromised. Furthermore, the new sequence in the variant protein matches the consensus for a leucine-rich NES motif that may be recognized by the exportin1-Crm1 export system. This new NES is added to and reinforces the two NES normally present in the N-terminal domain of the native protein [53]. Notably, when only Trp290 is replaced (mutant E and mutant F), a stronger NES motif, L-xxx-L-xx-V-x-L, is inserted to ensure maximal export in the cytoplasm of the NPM1 mutant. Thus, the combined effect of the loss of either one or both tryptophan residues and the appearance of a new NES in the variant protein is mandatory to completely alter the shuttling properties of the protein; indeed mutated protein is stably and aberrantly localized in the cytoplasm of leukemic cells (therefore referred to as NPM1c+, where c+ stands for cytoplasmic positive) and only a limited portion is retained within nucleoli [47, 54]. Moreover, since the mutated protein is able to oligomerize with the NPM1 protein synthesized by the wild-type allele, through its unchanged N-terminal domain, most of wt NPM1 is also a translator in the cytosol and only a minimal part of it is still conserved in the nucleoli (**Figure 5**) [66]. Because of its distinctive characteristics, this type of leukemia was included in the 2008 as a new provisional entity from World Health Organization classification of myeloid neoplasm [63].

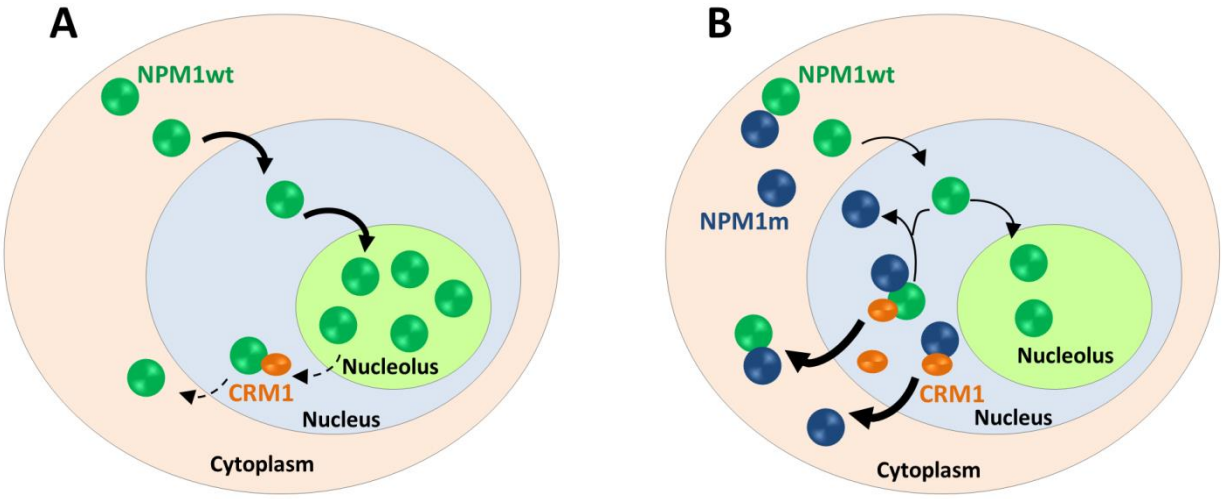

Figure 5. A) Mechanism of nucleo-cytoplasmic shuttling of wild-type NPM1. **B)** Mechanism of aberrant cytoplasmic expression of nucleophosmin (both mutated(blue) and wild-type proteins(green)) in AML with mutated NPM1 gene. NMP1m: NPM1 mutated; CRM1: Chromosomal Maintenance 1). Adapted from Falini et al.[47]

3. JAK/STAT SIGNALING PATHWAY

The JAK/STAT as well as the MAPK (Mitogen Activated Protein Kinase) pathway transmits information from extracellular cytokine/chemical signals, through the cell membrane into gene promoters on the DNA in the cell nucleus, causing the transcription and expression of target genes involved in immunity, proliferation, differentiation, apoptosis and oncogenesis [67]. The JAK/STAT system is a major signaling alternative to the second messenger system. In mammals, JAK/STAT pathway is the principal signaling mechanism for a wide array of cytokines and growth factors. The JAK/STAT system consists of three main components: i) a receptor, ii) Janus kinase (JAK) and iii) Signal Transducer and Activator of Transcription (STAT) [68]. The receptor is activated by a signal from interferon (IFN), interleukin (IL), growth factors, or other chemical messengers. This activates the kinase function of JAK, which phosphorylates itself and the receptor, in particular the cytoplasmic tail of gp130. In details, the ligand-receptor interaction triggers the activation of JAKs, and the consequent increased kinase activity phosphorylates tyrosine residues on the receptor and generates sites for interaction with proteins that contain phosphotyrosine-binding SH2 domains, like STATs proteins. Indeed, STATs are able of bind these phosphotyrosine residues and are themselves phosphorylated by JAKs, further they act as binding sites for SH2 domains of other STATs, mediating their dimerization. Following phosphorylation, STAT proteins form homo or heterodimers, and the activated complex translocates into the nucleus and binds to specific response elements of genes leading to their transcriptional activation (**Figure 6B**) [69]. STAT responsive genes affect many basic cell functions, like growth, differentiation and death [70]. It is evident that aberrations in these pathways could lead to chronic inflammatory diseases, or tumorigenesis.

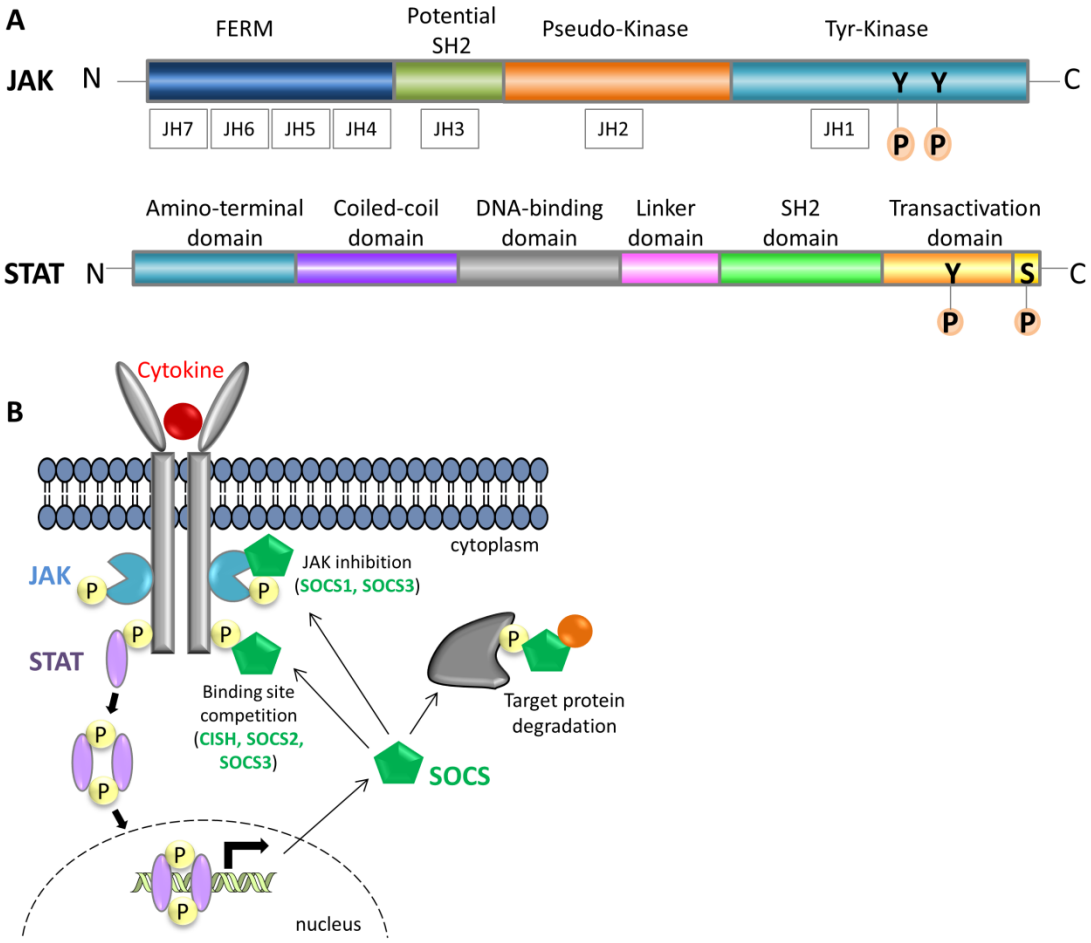

Figure 6. JAK/STAT signaling pathway. **A)** Modular representation of the structure of JAK and STAT protein family. **B)** Activation of the JAK/STAT pathway and its negative regulation by SOCS proteins. Adapted from Baker et al.[71]

The JAK family includes four members: JAK1, JAK2, JAK3 and TYK2. JAK1, JAK2 and TYK2 tyrosine kinases are ubiquitously expressed, while JAK3 expression is restricted to the hematopoietic lineage. JAKs are large proteins of approximately 1000 residues, with molecular masses of 120-140 kDa. Based on their primary sequences, JAK kinases were initially divided into seven members for several highly conserved regions (JH1-7, starting from the C-terminal end) but were subsequently organized into four functional domains (**Figure 6A**) [72-73]. The N-terminal region constitutes the receptor-binding module with a FERM domain (JH4-7) and an atypical SH2 domain (JH3) [73-74]. Instead, the C-terminal JH1 and JH2 domains are respectively a kinase and pseudo-kinase domain, and although this latter domain contains structural features of a tyrosine kinase, it does not have any catalytic activity. Reports suggest that it acts as a fine modulator of the catalytic activity of the kinase domain [75]. The JH2 domain was initially considered to be devoid of catalytic activity but was recently found to bind ATP and be able to phosphorylate two negative

regulatory sites in JAK2 [76]. Mutations in the JH2 domain have been shown to lead to hyperactive JAK2 [77-80], and constitutive activation of JAK2 is causing myeloproliferative diseases [81].

The STAT family is formed by seven members of 84-113 kDa (STAT1, STAT2, STAT3, STAT4, STAT5A, STAT5B, STAT6) characterized by regions of high homology which include an N-terminal domain that mediates cooperative binding to multiple DNA sites, a DNA-binding domain, a Src homology 2 (SH2) domain, and a carboxyl-terminal tyrosine phosphorylation site (**Figure 6A**). The C-terminal region contains two residues (Tyr 701 and Ser 727 in STAT1, Tyr 705 and Ser727 in STAT3) crucial for the activity of the STATs; particularly, the tyrosine phosphorylation by JAK promotes the dimerization of STAT while the serine phosphorylation increases its transcriptional activity [70].

The STAT protein is located in a latent form in the cytoplasm and its phosphorylation promotes the formation of homodimers (STAT1, STAT2, STAT4, STAT5A and STAT5b) or heterodimers (STAT1-STAT2 and STAT1-STAT3) through its SH2 domain. The active dimers are able to translocate into the nucleus where they bind binds to a consensus DNA-recognition motif called gamma-activated sites (GAS) in the promoter region of cytokine-inducible genes, activating the expression of chemokines such as C-C motif chemokine ligand (CCL) 2, CCL5, IL-8, and C-X-C motif chemokine (CXCL) 10; adhesion molecules like intercellular adhesion molecule (ICAM) 1 and vascular cell adhesion protein 1 and; extracellular matrix proteins such as collagen IV; and the early response genes c-fos and c-jun. STAT1-STAT2 heterodimers could also combine with interferon regulatory factor (IRF) 9 to form interferon stimulated gene factor 3, which is able to bind the interferon-stimulated response element promoter and activate gene expression [82].

Each STAT protein is activated by a specific signal. In details, the main function of STAT1 and STAT2 is to mediate IFNα/β/γ signaling; STAT3 is activated by IL-6, IL-10, epidermal growth factor (EGF), platelet-derived growth factor (PDGF) and also by active oncogenic proteins, such as Src and Ras; STAT4 is activated by IL-12 and IL-23; STAT5A and STAT5B are stimulated by prolactin, EGF, PDGF, IL-3, IL-5, and erythropoietin; while STAT6 is important for IL-4 and IL-13 signal [83].

3.1. Regulation of JAK/STAT pathway: SOCS proteins

Given the key role that JAK/STAT plays in the signaling of cytokines and other mediators involved in inflammatory diseases, many studies have highlighted the importance to regulate the duration and extent of this intracellular pathway to prevent tissue damage[84]. Transient JAK/STAT pathway activation is guaranteed by several mechanisms of negative regulation which operate at each step of signal transduction, such as ubiquitin-mediated receptor internalization, dephosphorylation of tyrosines in the JAK activation loop by constitutive phosphatases, and induction of suppressor of cytokine signaling (SOCS) proteins [85]. Members of SOCS family of proteins play key roles in the negative regulation of cytokine signal transduction. Indeed, these proteins function in a negative feedback loop, inhibiting the cytokine-activated JAK/STAT signaling pathway to modulate cellular responses (**Figure 6B**) [86].

The SOCS proteins comprise a family of eight intracellular proteins: cytokine-inducible SH2 protein (CIS), and from SOCS1 to SOCS7. CIS, SOCS1 and SOCS3 are most often associated with regulation of cytokine receptor signaling through the JAK/STAT pathway, while SOCS4-7 predominantly regulate growth factor receptor signaling [87-89]. SOCSs are thought to regulate over 30 cytokines, such as leukemia inhibitory factor, granulocyte colony stimulating factor (G-CSF), IFNγ, IL-6 and IL-10 [90]. The basal expression levels of SOCS proteins are low in physiological conditions, but they are selectively upregulated in response to cytokines stimulation in many immune, inflammatory and carcinogenic processes.

Each SOCS protein is endowed with a modular structure schematically reported in **Figure 7**. It is constituted by: i) a central Src homology 2 (SH2) domain that interacts in a specific manner with phosphotyrosine residues located on their target proteins, including cell surface receptors; ii) an N-terminal domain of variable length and sequence; and iii) a C-terminal 40-amino-acid conserved module known as the SOCS box that is comprised of two functional sub-domains: a BC box that recruits Elongin B and C, and a Cul box that mediates Cullin5 binding [89, 91-92].

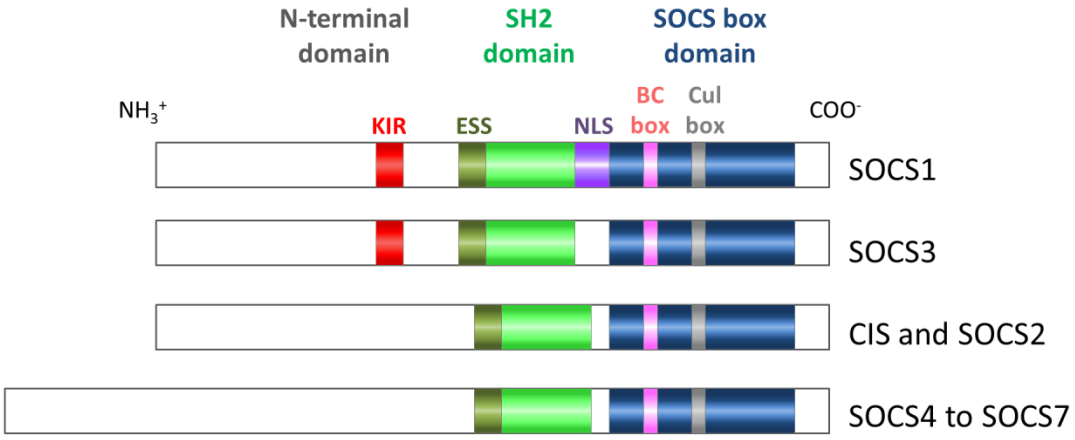

Figure 7. Modular representation of the structure of the SOCS protein family: SH2 domain in the middle portion and a SOCS box at the C-terminus are well conserved domains. Adapted from Yoshimura et al.[93]

Thus SOCS protein can be considered a substrate-recruitment module of E3 ubiquitin ligases that act to shut down cytokine signaling by inducing the proteolytic degradation of signaling molecules. Differently from other members (**Figure 7**), SOCS1 and SOCS3 possess a kinase inhibitory region (KIR) adjacent to the SH2 domain that is required for high-affinity binding to JAKs and the inhibition of JAK kinase activity [94].

Therefore, the SOCS family can inhibit cytokine signals either by binding to the JAK catalytic site (SOCS1 and SOCS3), either by competing with STAT for receptor binding sites (CIS, SOCS2 and SOCS3), or by activating their proteosomal degradation (all SOCS proteins)[94]. SOCS1 and SOCS3 share the highest degree of sequence homology to each other inside the SOCS family and, due to their ability to directly inhibit JAK, are the two most potent inhibitors of cytokine signaling[95]. Although their similarity, the JAK inhibition involved two different mechanisms [95].

In the past, Johnson and co-workers developed, thanks by mutagenesis studies, a peptidomimetics of KIR domain of SOCS1 able to bind to the autophosphorylation site of JAK2 acting as its pseudosubstrate [96-98]. Recently the X-ray crystal structure of a SOCS1/JAK1/ADP complex (**Figure 8A**) was reported [99]. Finally, this structure confirmed that the domain mainly involved in the interaction with JAK protein is KIR even if, the ESS as well as the SH2 domain make substantial contacts with the C-lobe of the JAK1 kinase domain. SOCS1 appeared able to directly bind and inactivate JAK1 protein: its KIR domain acts as pseudosubstrate and directly interacts with JAK tyrosine kinase inhibiting its catalytic activity and preventing the access of substrates[99].

For SOCS3, earlier the crystal structure of the ternary complex of SOCS3/JAK2/gp130 (**Figure 8B**) [100]was reported. From its inspection SOCS3 binds JAK2 and gp130 simultaneously and the SH2 domain of SOCS3 does not interact directly with phosphotyrosines in the activation loop of JAK [100]. SOCS3 is recruited to cytokine receptors that contain high-affinity SOCS3 binding sites (such as gp130, LeptinR, G-CSFR). Once attached to these receptors, SOCS3 can bind to JAK2 via an adjacent surface and directly inhibit the catalytic activity of those kinases. JAK binds receptor through its FERM domain and SOCS3 through its kinase domain. Receptor binds JAK via its Box1 motif and SOCS3 via pY 757. Finally, SOCS3 binds gp130 via its phosphotyrosine binding groove and JAK via a surface adjacent to this [100].

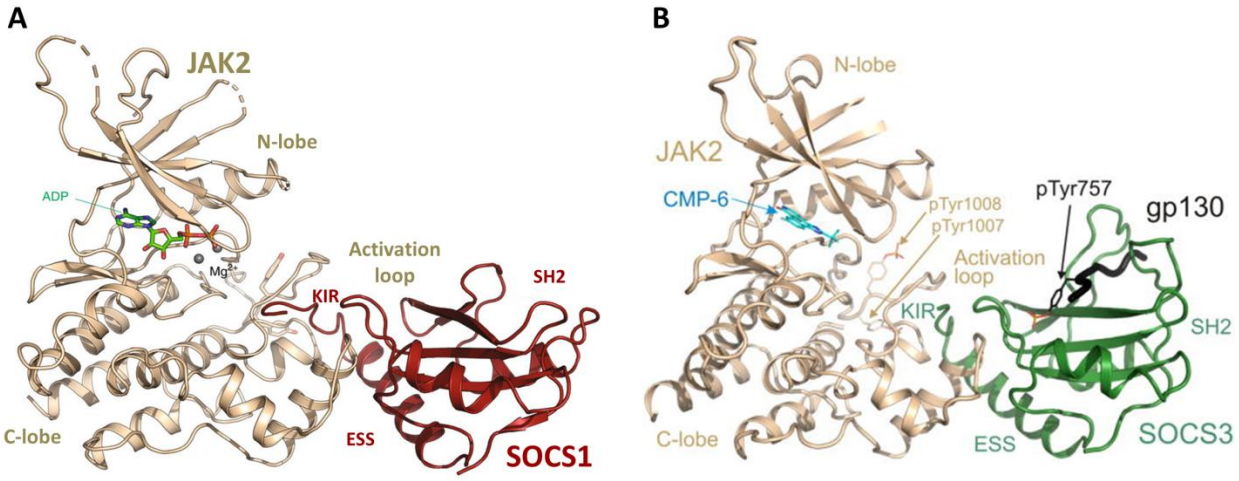

Figure 8. X-ray crystal structure of **A)** SOCS1/JAK1/ADP complex, and **B)** JAK2/SOCS3/GP130 complex. Adapted from Liau et al. and Kershaw et al [99-100]

3.2. JAK/STAT/SOCS signaling pathway in cancer and atherosclerosis

Several studies have described the key role of the JAK/STAT pathway in many inflammatory diseases such as rheumatoid arthritis, psoriasis, Crohn's disease and encephalomyelitis[101-103]. JAK/STAT is also involved in two important pathogenesis, atherosclerosis and cancer.

Atherosclerosis is a chronic multifactorial disease of the vascular wall and actually is the underlying cause of about 50% of all deaths in Western countries [104]. Interestingly, it was revealed that the JAK/STAT signaling pathway controls a large number of genes involved in leukocyte recruitment, migration and proliferation of vascular smooth muscle cells (VSMC), foam cell formation and apoptosis[105-106-107]. SOCSs have shown to play a key regulatory role in vascular cell responses; in experimental models, loss of neuronal/glial SOCS3 increases pathological

neovascularization [108], while SOCS3-specific antisense oligonucleotides aggravate inflammation and atherosclerosis[109].

Interestingly, JAK and STAT isoforms were found in inflammatory regions of human atherosclerotic plaques and in experimental models of atherosclerosis[109-114]. In mice, gene deficiency of STAT1 and STAT3 prevents the development of atherosclerotic plaques. Furthermore, therapy with inhibitors of JAK2 (ag490), STAT1 (fludarabine) and STAT3 (atiprimod) or with expression plasmids encoding SOCS, reduces the size of the lesion and neointimal hyperplasia[115-117]. Moreover, several studies revealed that acute and/or chronic inflammation alters the expression of SOCS proteins[118]. Particularly, SOCS1 and SOCS3 have been linked to a variety of pro-inflammatory and proaterogenic factors. Its expression has been also described in human atheroma plaques of patients[119-120].

On the other hand, several studies described the involvement of this pathway in cancer and the different role of SOCS1 and SOCS3.

Concerning SOCS1, controversial studies revealed that SOCS1 may function as either tumor suppressor or promoter, in a cell context-dependent manner [121-122]. Decreased expression of SOCS1 was observed in many cancers, including prostate cancer, hepatocellular carcinoma, pancreatic cancer and acute myeloid leukemia [123-126]. Although SOCS1 expression is frequently lost in many tumors, its overexpression has been reported in human breast, epidermal and neuronal tumors[127]. The reasons of this behaviour are still unknown.

On the other hand, the role of SOCS protein as tumor suppressor is largely investigated. SOCS3 resulted deleted or epigenetically downregulated in many types of solid tumors, and its functional deficiency is implicated in tumor development and metastases[128-129]. SOCS3 expression appeared downregulated in colorectal cancer tissues, and low level of SOCS3 associated with metastatic lymph nodes. On the contrary, patients with high expression of SOCS3 often showed a good prognosis [130]. Moreover, it was shown that the loss of SOCS3 expression also provides enhanced risks of recurrent disease in breast cancer patients [131]. Interestingly, SOCS3 revealed to be able to regulate the inflammatory cytokines in PTEN and p53 inactivated TNBC models[132]. Furthermore, SOCS3 deficiency at the mucosal surface, due to impaired alveolar macrophage secretion, contributes to epithelial cell transformation into mature tumor cells[133].

III. AIM OF THE THESIS

1. Conformational determinants of leukemogenic potentials of NPM1 mutations in AML

To fully understand the purposes of the work presented in this thesis, the mention to previous studies is of crucial importance.

An ongoing project from our research group is focused on the dissection of the CTD of NPM1 into peptides corresponding to the helices of the native three-helix bundle, to gain insights into their conformational behavior and their ability to interact with NPM1 biological partners. The CTD is essential for NPM1's biological functions and its functionality is due to the specific fold that it adopts: a three-helix bundle (**Figure 9**). The primary sequences of the three helices of the CTD of NPM1 share a high propensity to form α-helical structures as predicted through bioinformatics analysis[134].

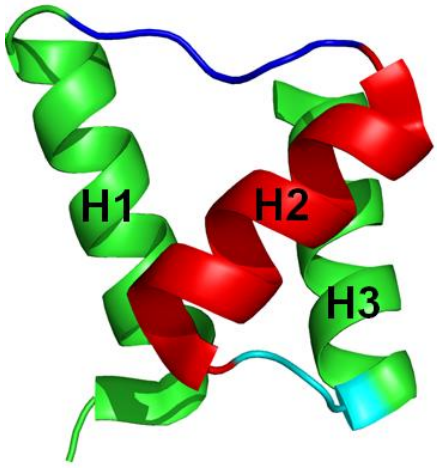

Figure 9. NMR structure of the CTD of wt NPM1[53].

Confirming this bioinformatics analysis, the first designed peptide, corresponding to the H1 region, assumed an α-helical structure with a helical content of ~39% and revealed to be stable upon increasing time and temperature; furthermore, it appeared to be able to bind to G-quadruplex structures in a cooperative recognition along with its N-terminal IDRs [135].

On the other hand, the peptide encompassing the H2 region showed an unexpected remarkable tendency to form amyloid-like assemblies endowed with fibrillar morphology and β-sheet structure. These aggregates appeared to be toxic in *in vitro* cell viability assay. Particularly, these studies, revealed that the "basic amyloidogenic unit" is the fragment corresponding to the sequence 268-272 FINYV (named H2 very short[268-272]). On the contrary, the extension of the H2

sequence beyond its N- and C-terminal ends to include the connecting regions with H1 and H3, delayed aggregation and its associated cytotoxicity [134]. Moreover, a systematic alanine scan of the H2 region 264-272 confirmed the crucial role of the fragment 268-272 FINYV for initial steps of self-recognition process. Substitutions within this stretch dramatically affect the β-conformations and the tendency to aggregate of the whole H2 region, as shown in **Figure 10**[136].

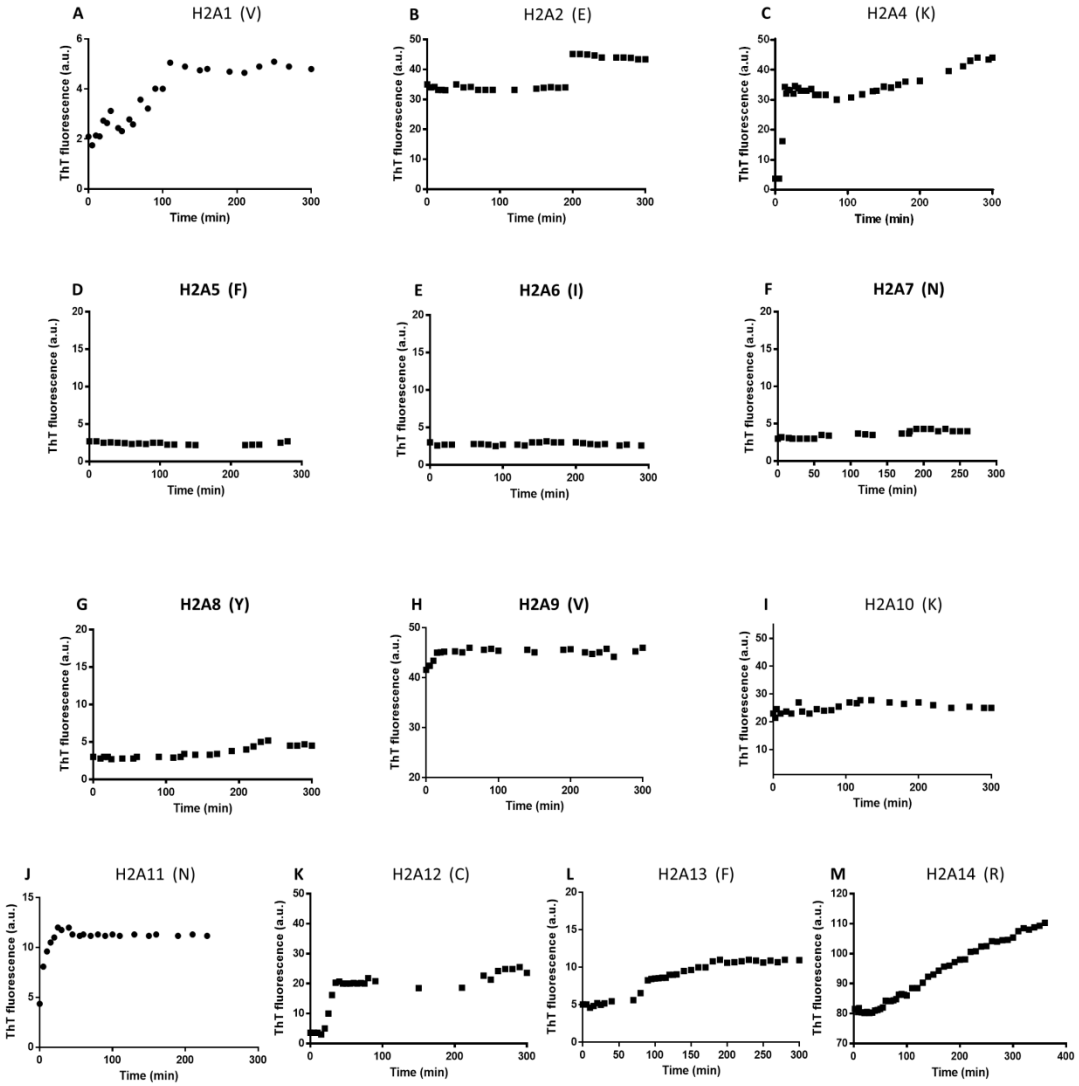

Figure 10. Time course of oligomers formation of H2A1 (A), H2A2 (B), H2A4 (C), H2A5 (D), H2A6 (E), H2A7 (F), H2A8 (G), H2A9 (H), H2A10 (I), H2A11 (J), H2A12 (K), H2A13 (L) and H2A14 (M) peptide, as determined by ThT fluorescence assay. Adapted from Russo et al. [136]

With respect with the H3 region, three main variants of this region were previously investigated. This region in the wt form includes Trp288 and Trp290 while, AML-NPM1 mutations, like the mutant E and A, lead to the loss of one or two Trp residues [53]. Conformational studies showed that both H3 mutants (H3 mut E and H3 mut A) displayed a typical unstructured profile with respect to the H3 wt.

Moreover, both mutated peptides showed a substantial tendency to aggregate and to be toxic in human SH-SY5Y neuroblastoma cells [137].

On the basis of these data, we reasoned that the destabilization of the CTD upon AML mutations could favor the exposure of the H2 region that could cause, in turn, the formation of toxic aggregates. These considerations pave the way to new therapeutic agents able to selectively kill leukemic blasts following a "cell starvation strategy".

Here, to deepen the molecular mechanisms associated with AML misfolding and to further evaluate the leukemogenic potential of these mutations, we investigated biophysical features of several protein regions, as follows:

1) The smallest amyloidogenic stretch of the entire NPM1 sequence: encompassing region264-272
2) H3 mut sequences related to all exon-12 amino acidic mutations reported in AML
3) The polypeptide deriving from the connection of H2 and H3 in the type A mutated variant, $NPM1_{264-298}$

2. Mimetic compounds of SOCS proteins as therapeutic agents

JAK/STAT pathway is a tightly regulated system and its alteration determines inflammatory and/or tumorigenic disease states. JAK/STAT regulation by SOCS proteins appeared critical for the normal regulation of the primary cytokine effects[129]. The KIR domain, present only in SOCS1 and SOCS3 proteins and crucial to inhibit the JAK2 catalytic activity, could be considered as a good starting point to develop potential drugs able to regulate JAK/STAT activity[138]. Particularly, for some years, the goal of our research group is to develop mimetics of SOCS1 and SOCS3 proteins.

2.1. KIR and neighboring regions of SOCS3

In multiple solid tumors dependent on the IL6/STAT3 pathway, SOCS3 overexpression suppresses the tumor growth and spread. In transformed MCF10A breast epithelial cells, simultaneous inactivation of tumor suppressors, p53, and PTEN, induces downregulation of SOCS3, led to the development and progression of TNBC. Interestingly, both the over-expression of SOCS3 or the blockade of the IL-6R inhibit the TNBC growth and the formation of metastasis in mouse xenograft models [132]. On the other hand, in human atherosclerotic lesions, VSMCs and macrophages express SOCS3, conferring it a key regulatory role in vascular cell responses[109]. On this basis, the development of SOCS3 mimetics appears a valid strategy to design active drugs for these diseases. The SOCS3 way of inhibition of JAKs' enzymatic activity is different with respect to SOCS1 [100].The X-ray structure of the protein complex among SOCS-3, JAK2 and gp-130 showed that KIR was required for the complex formation, but the SOCS-3-KIR peptide alone did not block JAK2 kinase activity[100].

In order to gain insights in molecular discriminants for the interaction of SOCS3 toward JAK2, in this thesis several linear peptides covering protein regions of SOCS3 were investigated starting from KIR region toward C-terminal extremity in a "protein dissection approach" [135]to identify the minimum active sequence (MAS) able to recognize JAK2. Subsequently, to better investigate cooperative mechanism of action in the recognition of JAK2 among different protein fragments, chimeric peptides connecting not contiguous SOCS3 regions were designed and characterized.

2.2. PS5 as lead compound of SOCS1 peptidomimetics

Concerning SOCS1, in 2012, our research group identified a new unnatural and potent peptidomimetic of SOCS1-KIR, named PS5[139]. This identification was carried out through the screening of a focused simplified combinatorial peptide library, in positional scanning format[140]. PS5

peptide was able to bind JAK2 catalytic site, with a K_D in the low micromolar range, acting as an antagonist of wt KIR. Its therapeutical application was tested in cellular-based treatment of type-1 immune-mediated skin diseases. Indeed, IFNγ-activated keratinocytes treated with PS5 exhibited impaired JAK2, IFNγRα, and STAT1 phosphorylation and also reduced the expression levels of IRF1 transcription factor, and the inflammatory genes ICAM1, HLA-DR, CXCL10 and CCL2. ICAM1 reduced expression resulted in an impaired adhesiveness of T lymphocytes to autologous keratinocytes and so the migration of T cells towards supernatants from PS5-treated keratinocytes was drastically reduced [141]. Moreover, the presence of an unnatural residue, Cys(Acm), renders this sequence more stable to protease degradation and suitable for cellular and *in vivo* experiments.

In this thesis, PS5 sequence was assumed as lead-compound to design new head-to-tail cyclic analogues containing different unnatural amino acids such as naphthyl group, with the aim to increase their rigidity and ameliorate their abilities to interact with JAK2 in a 1st generation of PS5 analogues. Later, to further rigidify the structure new analogues containing different intramolecular cycles were designed and tested.

IV. MATERIALS AND METHODS

1. Peptides covering NPM1

1.1. SOLID PHASE PEPTIDE SYNTHESIS

Reagents for peptide synthesis were from InBios (Naples, Italy). Solvents for peptide synthesis and HPLC analyses (dichloromethane (DCM), Dimethylformamide (DMF), methanol, trifluoroacetic acid (TFA), diethyl ether, water and acetonitrile) were from Romil (Dublin, Ireland); all other reagents such as triisopropylsilane, piperidine and DIEA were supplied by Sigma-Aldrich (Milan, Italy). Derivatized amino acids with 9-fluorenylmethoxycarbonyl (Fmoc) (purity> 99%), activating reagents HBTU, HOBt were provided by Iris Biotech. Solid-phase peptide syntheses were carried out by means of an automatic multichannel synthesizer (SYRO I) (MultiSynTech, GmbH, Witten, Germany). Preparative RP-HPLC was performed on an LC-8A equipped with an SPD-M10 AV detector (both from Shimadzu, Kyoto, Japan) and a C18 Jupiter column (50 × 22 mm inner diameter; 10 µm; Phenomenex, Castel Maggiore, Italy). Reversed-phase (RP) columns for peptide analysis and the liquid chromatography-mass spectrometry (LC-MS) system were from Thermo Fisher Scientific (Waltham, MA, USA). LC-MS analyses were performed on an LCQ DECA XP Ion Trap mass spectrometer equipped with an Opton Educational Services, Inc. source, operating at 4.2 kV needle voltage and 320°C, with a complete Surveyor HPLC system, comprising an MS pump, an autosampler, and a photo diode array (all from Thermo Fisher Scientific).

Peptide sequences were prepared by the solid phase method on a 50 µmol scale following the Fmoc strategy and using standard fluorenylmethoxycarbonyl (Fmoc)-derivatized amino acids RINK AMIDE resin (substitution 0.5 mmol/g) was used as solid support [142]. Activation of amino acids was achieved using 2-(1H-benzotriazol-1-yl)-1,1,3,3-tetramethyluronium hexafuorophosphate (HBTU)/1-hydroxy-benzotriazole (HOBt)/di-isopropylethylamine (DIEA) (1:1:2), whereas Fmoc deprotection was carried out using a 40% (v/v) piperidine solution in DMF. All couplings were performed for 20 minutes and deprotections for 10 minutes.To better mime the protein regions, the peptides were acetylated and amidated at the extremities.

Peptides were then removed from the resin by treatment with a TFA:tri-isopropylsilane (TIS):H2O (90:5:5 v/v/v) mixture for 90 min at room temperature, then they were precipitated in cold ether, dissolved in a water/acetonitrile (1:1 v/v) mixture, and lyophilized.The peptides were purified by preparative RP-HPLC, applying a linear gradient of 0.1% TFA CH3CN in 0.1% TFA water from 5-70%

over 13 min with a semipreparative 2.2 × 5 cm C18 column at a flow rate of 20 ml/min, using a UV detector set at a wavelength of 210 nm. The purity of the purified fractions and the molecular weight of the peptides were evaluated by LC-MS analysis. Then, NPM1 mimetic peptides were all pre-treated overnight with hexafluoroisopropanol (HFIP) in order to determine a monomeric state [143], lyophilized and stored at -20 °C until use.

1.2. CONFORMATIONAL AND FUNCTIONAL STUDIES

Far-UV circular dichroism spectroscopy

Samples were prepared by dilution of freshly prepared stock solutions (1 mM peptide on average in phosphate buffer 50 mM), with peptide concentrations determined by UV absorbance with an ε_{275} value of 1390 $cm^{-1}\,M^{-1}$. Circular dichroism (CD) spectra were recorded on a J-810 spectropolarimeter (JASCO Corp, Milan, Italy), registered at 25°C in the far-UV region from 190 to 260 nm. Other experimental settings were 20 nm/min scan speed, 2.0 nm band width, 0.2 nm resolution, 50 mdeg sensitivity, and 4 s response. Each spectrum was obtained with an average of 3 scans and the intensity is reported as average molar ellipticity per residue (deg cm^2 $dmol^{-1}$ res^{-1}). Machine data units of millidegrees ellipticity were normalised as a function of the concentration of solutions and the number of amide bonds by conversion to mean residue molar ellipticity (θ) using the following equation (where n is the number of peptide bonds and Ellipticity is the raw data from the instrument):

$$\theta(\mathrm{deg\ cm^2\ dmol^{-1}}) = \frac{\mathrm{Ellipticity(mdeg)} \times 10^6}{\mathrm{Pathlength(mm)[C](\mu M)}n}$$

The peptide concentration was 50 or 100 µM, and a quartz cuvette path length of 0.1 cm was used. To record the spectra was used a phosphate buffer solution at a concentration of 10mM pH 7,4.

Fluorescence assays

All fluorescence assays were performed using a Jasco FP 8300 spectrofluorometer and a cell of 10 mm path-length quartz cuvette, under magnetic stirring. For NPM1 $_{264\text{-}272}$, ThT assays were carried out at 200 µM of peptides and 50 µM of ThT at 25 °C in phosphate buffer 50mM. Measurements were collected every 1-5 minutes during 350-450 minutes, using excitation and emission wavelengths

of 440 and 450–600 nm, respectively. The amyloid seeding assay was performed by stirring NPM1 $_{264-272}$ fragment for 200 min and adding it to freshly dissolved treated peptide solutions. For EGCG experiment, the small molecule was added at a 2_1 ratio with respect to treated peptide. Tyr assays were carried out at 300µM of peptides at 25 °C in phosphate buffer 50mM using a Varian Cary Eclipse spectrofluorimeter (Varian, California, USA).Measurements were collected every 1-5 minutes during 300 minutes.

Concerning H3 mutant peptides, ThT assays were carried out at 800 µM of all peptides in phosphate buffer 50mM, except mutA short (580 µM), mutB extended (672.5 µM), mutE short (322 µM), and mutF short (416 µM) with ThT 50 µM at 25 °C. Measurements were collected every 5-15 minutes during 24-48 hours, using excitation and emission wavelengths of 440 and 450–600 nm, respectively. Fluorescence intensities were then reported subtracted of the corresponding value of ThT alone (at 50 µM) at each time of analysis.

For NPM1$_{264-298}$, both ThT and Tyr assays were carried out at 116 and 100 µM, respectively, at 25 °C in phosphate buffer 50 mM and the former at 50 µM of ThT. ThT (λ_{exc}: 440nm, λ_{emiss}: 481 nm) and Tyr (λ_{exc}: 275nm, λ_{emiss}:303nm) fluorescence. Measurements were collected every 20 minutes until 60-80 hours.

For all experiments, $t_{1/2}$ were calculated as $F_{max}/2$ where Fmax is the maximum emission intensity.

Time resolved fluorescence experiments

On the basis of kinetic data, aggregating peptide solutions were analyzed at the same concentrations of ThT assays at different times coincident with maxima fluorescence intensities.

Fluorescence decays were recorded with a time-correlated single photon counting (TCSPC) system, exciting with a pulsed laser diode (336 nm). Lifetime traces were recorded with the monochromator at ranges 380-440 nm, 8-nm slit width, and collection time of 10,000 counts in the peak channel. The instrument response was recorded using scattering solutions (Ludox 0.1%) at 336 nm.

Congo Red Absorbance assay

Interaction of CR with peptide aggregates was tested using a NanoDrop 2000, Thermofisher, UV-Vis Spectrophotometer (Waltham, MA) by recording the absorbance spectra from 400 nm to 800 nm using a 10 mm quartz cell. H3 mutated peptides at 800 µM concentration and buffer as control

were incubated in 5 mM phosphate, pH 7.4, at 25 °C and an aliquot of 37.5 µL of each sample was mixed with 462.5 µL of a 5 mM phosphate, 150 mM NaCl buffer at pH 7.4 containing 20 µM CR. Spectra were then recorded in time interval 0-100h.

Dynamic Light Scattering

$NPM1_{264-298}$ sample (1.0 mM monomer concentration), was kept under stirring in 50 mM phosphate, pH 7.2, at 25 °C. The measurements were performed using a Zetasizer Nano S DLS device from Malvern Instruments (Malvern, Worcestershire, UK) with 633 nm laser, dual scattering angle mode, thermostated with a Peltier system and using a low-volume (50 µL), ultramicro cell. Size distributions by intensity and total light scattering intensity were determined in automatic mode at regular time-intervals over a period of 10 min for each measurement. Thirteen acquisitions were recorded, each of 10 seconds in duration.

Isothermal titration calorimetry (ITC) experiments

ITC experiments were performed with an iTC200 calorimeter (Microcal/GE Healthcare), using ITC data of EGCG (1mM) in the syringe to NPM1 $_{264-272}$ (200 µM) in the cell both in phosphate buffer 50 mM pH 7.2. The heat generated per injection as EGCG bound to the NPM1 $_{264-272}$ fragment was recorded and displayed as differential power (µcal s^{-1}) vs. time (min). The area under each injection peak was integrated and presented as kcal mol^{-1} of injectant vs. the molar ratio of [protein]/[EGCG]. Subtracting the integrated peak areas for ligand/buffer titration from the ligand/protein titration allows a direct determination of thermodynamic parameters. Data were fitted to a “sequential binding (n=2) of sites” model with Origin software (GE Healthcare). Thermodynamic parameters were estimated after subtracting the control experiment (EGCG in buffer HBS).

ESI experiments

NPM1 $_{264-272}$ peptide was diluted to 250 µM peptide in ammonium bicarbonate (20 mM) pH=8.3. ESI mass spectra were acquired in positive ion mode on a LCQ DECA XP Ion Trap mass spectrometer (ThermoElectron, Milan, Italy). The employed OPTON ESI source was operated at 1.8 kV and the ESI sample solutions were infused at 10 µL/min using the pump system. The desolvation and source temperature were 150 °C and 80 °C, respectively, and the cone voltage was set to 20 V. Mass spectra were recorded continuously over the mass range 400–2000 Da in

positive mode. The BioMass program was employed to deconvolute all registered multi-charge spectra.

Confocal microscopy

Confocal analysis was performed by Leica SP5 microscope. Bright field and fluorescence images using a HCX IRAPO L 40×/0.95 water objective were acquired. The intrinsic fluorescence of fibers was investigated by Multiphoton (MP) modality using the Second Harmonic Generation technique (SHG), with a λ_{exc} at 840 nm. Autofluorescence was collected from 420–600nm. Then a solution of 100µM of peptide was incubated with a solution of ThT (50µM) in phosphate buffer (pH 7.4) at room temperature for 15 hours. After the incubation, the fluorescence of formed fibers was analyzed using the excitation wavelength of ThT at 440 nm, and the detection occurred between 460-600 nm. Images were acquired with a resolution of 1024 × 1024 pixels, zoom 1, 2.33A.U. and at maximum of pinhole.

1.3. MORPHOLOGICAL ANALYSIS OF FIBERS

Scanning electron microscopy

For H3 mutants, mutC short and extended were dissolved at three different concentrations (500, 800, 1500 µM), while mutF at 1500 µM in phosphate buffer 50mM and incubated for six hours under stirring. mutC short was also analyzed at 0 and 2h of aggregation.

NPM1 $_{264\text{-}272}$ peptide, was dissolved at 500 and 1500 µM in phosphate buffer 50mM while, NPM1$_{264\text{-}298}$ peptide at 100 µM and both were incubated under stirring. Then, 20µL of aggregating solutions were deposited on an aluminum stub and the solvent was allowed to evaporate.

Finally, samples were sputtered with Au/Pd conductive layer using a Denton Vacuum Desk V TSC coating system. SEM micrographs were recorded with a Field Emission Gun Scanning Electron Microscope (FEG-SEM) FEI/Thermofisher Nova NanoSem 450, at 3.00 kV in high vacuum mode, using an Everhart Thornley Detector (ETD) and the Through the Lens Detector (TLD).

Wide-Angle X-ray Scattering

Fibril diffraction WAXS patterns were recorded from stalks prepared by the stretch frame method [144]. Briefly, a droplet (10 µL) of peptide dissolved in phosphate buffer 50mM (5mg/mL), after 5/7

days of incubation under stirring at 25°C, was suspended between the ends of a wax-coated capillary (spaced 2 mm apart). The droplet was allowed to dry gently at room temperature overnight to obtain oriented fibrils. Optical images of fibers were recorded with a Dino-Lite Digital Microscope Premier at 57x magnification and 1280x1024 resolution using the DinoCapture 2.0 software. The WAXS experiments were performed with the laboratory set-up of the XMI-Lab[1-2] equipped with Fr-E+ SuperBright rotating anode copper anode microsource (Cu K_α, λ=0.15405 nm, 2475W), multilayer focusing optics (Confocal Max-Flux; CMF 15-105) and three-pinhole camera (Rigaku SMAX-3000). An image plate (IP) detector with 100 µm pixel size was placed at 10 cm from the sample and calibrated by means of the Si NIST standard reference material (SRM 640b) [145-146].

1.4. CELLULAR ASSAYS

Cell culture

Human SH-SY5Y neuroblastoma cells (American Type Culture Collection (ATCC), Manassas, VA) were cultured in DMEM, F-12 Ham with 25 mM HEPES and $NaHCO_3$ (1:1) and supplemented with 10% Fetal Bovine Serum (FBS), 1.0 mM glutamine and antibiotics. Cell cultures were maintained in a 5.0% CO_2 humidified atmosphere at 37°C and grown until they reached 80% confluence for a maximum of 20 passages.

MTT reduction assay

Short and extended versions of the wt, mutC and mutF H3-derived peptides (1 mM monomer concentration) and H2 mutA peptide (267µM monomer concentration) were incubated in 50 mM sodium phosphate buffer, pH 7.2, 25°C under stirring, for 0, 6, 24 and 72 h. Their cytotoxicity was then assessed in SH-SY5Y cells seeded in 96-well plates 24 h at 37°C after their addition to the cell culture medium at a 100 µM peptide concentration, by the 3-(4,5-dimethylthiazol-2-yl)-2,5-diphenyltetrazolium bromide (MTT) reduction assay [147].

Measurement of intracellular Ca^{2+}

Aggregated wt, mutC and mutF H3-derived peptides were diluted in cell culture media at a 100 µM peptide concentration, and then added to the SH-SY5Y cells seeded on glass coverslips for 60 min at 37°C as previously reported[148]. The cells were then loaded for 15 min at 37°C with 10 µM Fluo-4 AM (Thermo Fisher Scientific, Waltham, MA, USA). The resulting cell fluorescence was

analyzed by confocal Leica TCS SP5 scanning microscope (Mannheim, Germany) equipped with an argon laser source for fluorescence measurements at 488 nm and a Leica Plan Apo 63× oil immersion objective. To quantify the signal intensity of the fluorescent probe between 10 and 22 cells were analyzed using ImageJ software (NIH, Bethesda, MD). Intracellular Ca^{2+}-derived fluorescences were expressed as the percentage of the value for untreated cells (taken as 100%).

2. SOCS peptidomimetics

2.1. SOLID PHASE PEPTIDE SYNTHESIS

The solid phase peptide synthesis was performed as already reported for NPM1 peptides.

The synthesis of internal cyclic PS5 and internal cyclic PS5 Nal1 were obtained by employing peculiar methodologies. Since the formation of lactam bridge was performed on solid support, the use of super-acid labile protecting group was required. In particular were used Fmoc-Lys(Mtt)-OH and Fmoc-Asp(beta-isopropil)-OH. The cyclization reaction, at the end of the peptide assembly, has been performed with 1% TFA in DCM, the addition of 5% triisopropysilane (TIS), at room temperature, washing five times for two minutes. The solution was prepared as 94:1:5 DCM/TFA/TIS. After the deprotection of both lysine and aspartic acid, the coupling reaction was performed adding HATU and DIEA overnight.

Peptides were then removed from the resin and purified by preparative RP-HPLC. The purity of fractions and the molecular weight of the peptides were evaluated by LC-MS analysis. Peptide products were lyophilized and stored at -20 °C until use.To perform cellular assays CPPs (Cell penetrating Peptides) conjugated peptides were synthesized and purified. Conjugated peptides were also labelled at their N-termini with Fluoresceine-βAla or 5-(and-6)-carboxytetramethylrhodamine (TAMRA).

2.2. CONFORMATIONAL, FUNCTIONAL AND COMPUTATIONAL STUDIES

Far-UV circular dichroism spectroscopy

Circular dichroism (CD) assays were performed as previously described for NPM1 peptidomimetics.

NMR

A Varian Unity Inova 600 MHz spectrometer equipped with a cold probe was implemented to acquire NMR experiments that were all registered at 298 K. To prepare the NMR samples, the peptides (1.2 mg each) were dissolved in 600 µL of a mixture H_2O/D_2O (99.9% D, Sigma Aldrich, Milan, Italy) 90/10 v/v. TSP (Trimethylsilyl-3-propionic acid sodium salt-d4, 99% d, Armar Scientific, Switzerland) was added to the sample as internal standard for chemical shift referencing. For KIRCONG chim peptide, NMR samples were prepared by dissolving the peptide (0.9 mg) either in

H_2O with 10% v/v D_2O (98% D, Sigma-Aldrich, Milan, Italy), or in aqueous mixtures containing 15% and 40% v/v 2,2,2-trifluoroethanol-D3 (99.5% isotopic purity, Sigma-Aldrich, Milan, Italy); with final sample volumes equal to 500 μL.

1D [^{1}H] proton experiments were recorded with a relaxation delay d1=1.5 s and 64 scans. For conformational analyses the following NMR spectra were recorded: 2D [^{1}H, ^{1}H] TOCSY (Total Correlation Spectroscopy)[149], NOESY (Nuclear Overhauser Enhancement Spectroscopy) [150], ROESY (Rotating frame Overhauser Enhancement Spectroscopy)[151]and DQFCOSY (Double Quantum-Filtered Correlated Spectroscopy)[152]. Typical acquisition parameters were as follows: 16-64 scans, 128-256 FIDs in t1, 1024 or 2048 data points in t2. TOCSY experiments were recorded with 70 ms mixing time, NOESY experiments with 300 ms mixing time, and ROESY experiments with 250 ms time. Water suppression was accomplished through *Excitation Sculpting* [153]. Proton resonance assignments were obtained with a canonical strategy [154]. The VNMRJ 1.1D (Varian, Italy) software was used to process NMR spectra that were next inspected with the software NEASY included in CARA (http://www.nmr.ch/).

For Internal cyclic PS5 and Internal cyclic PS5 Nal1, NMR structures were calculated using CYANA 2.1 [155]. Distance constraints were generated from 2D [^{1}H, ^{1}H] ROESY 250 spectra, and angular constraints with the GRIDSEARCH module of CYANA. The non-standard amino acids S-acetaminomethyl-L-cysteine (C(Acm)) and 3-(1-naphthyl)-alanine (Nal1) were added to the CYANA standard residue library. Values of the atomic coordinates were obtained from Chimera where the residues were built and energy minimized. Asp1 and Lys9 side chains in both peptides were also modified in the CYANA library to allow the linkage between the CG of Asp and the NZ of Lys. The distance between Asp1 CG and Lys9 NZ atoms was imposed equal to 1.33 Å during structure calculations. Internal cyclic PS5 structures were generated from 92 ROE upper distance limits (67 intraresidues, 22 short-, 0 medium- and 3 long-range), including the distance constraint that was inserted for Asp1-Lys9 linkage, and 39 angular constraints. Internal cyclic PS5 Nal1 was generated from 146 NOE upper distance limits (117 intraresidues, 26 short-, 0 medium- and 3 long-range), including the distance constraint that was inserted for Asp1-Lys9 linkage, and 32 angular constraints. Calculations started from 100 random conformers, then 20 structures, provided with the lowest CYANA target functions were subjected to further unrestrained energy minimizations that were carried out with the software UCSF Chimera (version 1.10.1) [156]. Peptides minimizations were achieved through 1000 steps of steepest descent and 1000 steps of conjugate gradients. Structures were finally inspected with the programs MOLMOL [157] and PROCHECK NMR [158]. In

Chimera the structures were clusterized by matching in all residues of the 20 NMR conformers, excluding N-terminal acetylation and C-terminal amidation.

Also the NMR solution structures of KIRCONG chim peptide in H_2O and H_2O/TFE mixtures were calculated with the software CYANA. The non-standard amino acid β-Alanine (BAL) was built and added to the CYANA[155] standard residue library. Distance constraints (:upper distance limits) were generated from manual integration of peaks in 2D [^{1}H, ^{1}H] NOESY spectra (300 ms mixing time) or 2D [^{1}H, ^{1}H] ROESY spectrum for the sample in H_2O; the GRIDSEARCH module of CYANA software was implemented to obtain angular constraints. 100 random conformers were initially generated and in the end the 20 structures provided with the lowest CYANA target functions and better obeying to experimental constraints, were selected as representative NMR conformers and additionally analyzed with the software MOLMOL and UCSF Chimera, that were also used to generate structure images.

Microscale Thermophoresis

MST experiments were carried out with a Monolith NT 115 system (Nano Temper Technologies) equipped with 100% LED and 40% IR-laser power. Labeling of His-tagged Catalytic Domain of JAK2 (residues 826-1132) (Carna Bioscences) was achieved with the His-Tag labeling Kit RED-tris-NTA. SOCS3 derived peptides were used in the following concentrations: ESSCONG 404μM, KIRCONG chim 409μM, restKIRESSCONG 408μM in labeling buffer (Nano Temper Technologies); the dye concentration was adjusted to 100 nM while the protein concentration was 200nM. Subsequently, 100μL of protein and 100μL of dye were incubated in the dark for 30 min. To monitor binding of SOCS3 derived peptides, a serial dilution (1:1) was carried out by preparing 14-16 samples on average. Premium capillaries were employed for analysis, at 25°C in 50mM Tris-HCl buffer (150mM NaCl, 0.05% Brij35, 1mM DTT, 10% glycerol, 15% TFE) at pH 7.5. Data points were fitted with a non-linear regression, one site-total binding equation (Prism 5 GraphPad Software Inc).

Surface Plasmon Resonance

The BIAcore 3000 SPR binding assays for real-time and related reagents were purchased from GE Healthcare (Milan, Italy). The biotinylated catalytic domain of JAK2 (826-1132 aa) from (Carna

Bioscences)has been immobilized at a concentration of 50 µg/mL in HBS (10 mM Hepes, 150 mM NaCl, 3 mM EDTA, pH 7.4) 0.1mM TCEP (tris (2-carbossietyl) phoshin) buffer (flow 5 µL/min, injection time 7 min) on a streptavidin coated chip, reaching immobilization level of 750 RU. All peptides were dissolved in running buffer and binding experiments were set up at 25 °C with a flow rate of 20µL/min. All samples and buffers were degassed prior to use. The association phase (k_{on})was followed for 180s, whereas the dissociation phase (k_{off}) was followed for 300 s. The complete dissociation of active complex formed was achieved by addition of 1 M NaCl, for 60 s before each new cycle start. The reference chip sensorgrams were opportunely subtracted to sample sensorgrams. When experimental data met quality criteria, kinetic parameters were estimated assuming a 1:1 binding model and using version 4.1 Evaluation Software (GE Healthcare).

Computational Methods

Protein Preparation. JAK2 (PDB: 3FUP[159], chain A) missing atoms and residues were reconstructed with Swiss Model[160], as well as SOCS1 (PDB: 6C7Y[161], chain B). The complex JAK2/SOCS1 was constructed by aligning both the reconstructed JAK2 and SOCS1 to the JAK1/SOCS1 complex (PDB: 6C7Y[161]) with Swiss PDB Viewer[162]. JAK2/KIR was extracted from this complex. The JAK2/KIR complex was then minimized by performing a steepest descent minimization to be stopped either when the maximum force was lower than 1000.0 kJ/mol/nm or when 50000 minimization steps were performed with 0.005 kJ/mol energy step size, with Verlet cutoff scheme, short-range electrostatic cut-off and Van der Waals cut-off of 1.0nm. We used GROMOS 54a7 force field[163] and run the minimization as implemented in the Gromacs package v. 2016.1 [164].

Peptides preparation and docking. Ligands structures obtained by NMR were first minimized with AM1 method as implemented in MOPAC [165]. The minimized peptides were docked to the KIR binding site on JAK2 with AutoDock Vina [160]. The docking cubic box was (22.5x19.5x22.5)Å side and centered on KIR in the minimized JAK2/KIR complex (as identified by AutoDock tools). The docking was performed with exhaustiveness 500 and energy range 50. Larger exhaustiveness ad energy ranges led to the same result. The calculations run on 32 cpu and were performed on the MoNaLiSA cluster hosted at the University of Udine, Italy.

*Molecular Dynamics Simulations.*The complex was minimized by first minimizing the protein side chains alone, then whole protein and finally the whole system by constraining selected portions of the system. We placed the complex in a cubic box with a water layer of 0.7 nm and performed a

second minimization.We used GROMOS 54a7 force field [163] and Simple Point Charge water. Ligand topologies were built with ATB [166]. We performed NVP and NPT equilibrations for 100 ps, followed by 150 ns NPT production run at 300 K. The iteration time step was set to 2 fs with the Verlet integrator and LINCS[167] constraint. We used periodic boundary conditions. All the simulations and their analysis were run as implemented in the Gromacs package v. 2016.1 [164]. RMSDs and RMSF have been calculated from configurations sampled every 10ps and as running averages over 100 sampled points. VINA scorings were calculated over configurations sampled every 100 ps and as running averages over 10 points. The binding free energy was estimated with the MM/PBSA method, with the apolar solvation energy calculated as solvent accessible surface area (SASA) and default parameters, as implemented in the g_mmpbsa tool [168]. Simulations were run on Marconi (CINECA, Italy).

Serum stability

Diluted FBS at 25% (w/v) was used to analyse peptides stabilities. In details, peptides were incubated at 37°C in FBS. 80 µL aliquots of the incubating mixtures were at selected times taken and mixed with 80 µL of 15% trichloroacetic acid (TCA) and incubated at 2 °C for at least 15 min to precipitate serum proteins. Reverse phase high performance liquid chromatography (RP-HPLC) was performed on a HPLC 1200 series (Agilent Technologies) with UV detector using a C18 column from ThermoFisher (Milan, Italy). Gradient elution was performed at 25°C (monitoring at 215nm) in a gradient starting with buffer A (0.1 % TFA in water) and applying buffer B (0.1 % TFA in acetonitrile) from 5 to 70 % in 15 min. These assays were performed in triplicate.

2.3. CELLULAR EXPERIMENTS

Cell cultures

VSMCs from mouse aorta were isolated by enzymatic digestion cultured in DMEM supplemented with 10% FBS, 100 U/mL penicillin, 100 µg/mL streptomycin, and 2 mM L-glutamine (Sigma-Aldrich) and used between the 4^{nd} and 7^{th} passages. Murine macrophage cells (RAW 264.7 cell line, ATCC) were cultured in DMEM with 10% FBS, 100 U/mL penicillin, 100 µg/mL streptomycin, and 2 mM L-glutamine (Sigma-Aldrich).

Quiescent cells (24h in medium with 0% FBS) were pre-treated for 90 min with peptides conjugated to TAT derived cell penetrating sequence, 12.5 µM before stimulation with recombinant cytokines (IFNγ 10^3 U/mL plus IL-6 10^2 U/mL; PeproTech) for different time periods.

For KIRESS peptide, 4T1 murine breast tumor and MDA-MB-231 cell lines were purchased from ATCC. All cell lines were analyzed for mycoplasma contamination using MycoAlert Mycoplasma Detection Kit (Lonza, Walkersville, MD). 4T1 cell line was maintained in RPMI supplemented with 10% FBS and antibiotic/antimycotic 10,000 units/mL. MDA-MB-231 cell line was maintained in DMEM/F-12 supplemented with 2.5 mM L-glutamine, 15 mM HEPES, 0.5 mM Sodium Pyruvate and 5% FBS.

Viability and proliferation assays

The cell viability and proliferation were analyzed by MTT assay.

For viability assay, VSMCs were plated in 96-well plates ($1x10^4$ cells/well) and allowed to attachtovernight at 37°C, then incubated overnight in serum-free media at 37°C. Peptides were then added to the plate (12.5 µM) and incubated for additional 6 h in medium containing 0.5% FBS. MTT solution was then added for 2h. The absorbance of the metabolized MTT was measured at λ = 600 nm in a plate reader.

For the cell viability assay, VSMCs ($5x10^3$ cells/well) were processed similarly except that peptides were incubated for 24h in medium containing 10% FBS.

Wound healing assay

Migratory capacity of VSMCs was assessed by wound healing experiments. VSMCs were plated in 12-well plates ($3x10^5$ cells/well) and depleted for 24h in medium with 0.5% FBS, then scratches were applied using a sterile 200-µl pipette tip pipette tip, and cells were incubated with cytokines in the presence or absence of peptides. To determine the closing speed of the wound, two images of each well were captured at different stimulation times (0, 3, 19, 26, 45h), the cell-free area was quantified (Image Pro-Plus; Media Cybernetics) and normalized with respect to the initial time.

mRNA expression analysis

Tryzol (Life Technologies) was used to extract total RNA from cultured cells. Target gene expressions were analyzed by quantitative real-time polymerase chain reaction (PCR; Applied Biosystem), and mRNA values were normalized to housekeeping gene 18S.

Protein expression analysis

Cells were lysed in ice-cold buffer (150 mM NaCl containing 1% Triton X-100, 10 mM Tris pH 7.4, 0.5% NP-40, 1 mM EDTA, 1 mM EGTA, 0.2 mM Na_3VO_4, 0.2 mM PMSF, 10 mM NaF, and protease inhibitor cocktail). Total proteins (25µg) were electrophoresed, transferred onto polyvinylidene fluoride membranes and immunoblotted for phosphorylated STAT1 (P-STAT1; Invitrogen), P-STAT3 (Cell Signaling), STAT1 (Santa Cruz Biotechnology), STAT3 (Cell Signaling), and α-tubulin (loading control; Sigma-Aldrich) using appropriate peroxidase-conjugated secondary antibodies and chemiluminescent substrate.

Immunofluorescence studies

The VSMCs were plated on slides with 4 cameras treated for cell growth. Cells were treated for 90min with TAMRA-conjugated peptides before stimulation (1h), then fixed (4% paraformaldehyde), permeabilized (0.5% Triton X-100) and incubated overnight with primary antibodies (P-STAT3 and PSTAT1), followed by FITC-secondary antibody (Sigma-Aldrich) and nuclear counterstaining with diamidino-2-phenylindole (DAPI).

Finally, the samples were mounted using FluorSave and a confocal fluorescent microscope (Leica) was used to capture images.

DHE assay

For the detection of superoxide anion, VSMCs plated on coverslips were incubated with the fluorescent dye dihydroethidium (DHE) at 2.5µM in KRB-HEPES buffer, for 30 minutes at 37°C. After several washes to remove excess of fluorescent probe, the VSMCs were stimulated and fixed with 1.5% paraformaldehyde, contrasted with DAPI and mounted. The samples were analyzed by fluorescence microscopy (λexc = 488 nm and λem = 585nm). ROS levels were expressed as number of DHE positive cells vs total cells (nuclear staining with DAPI).

Statistical analysis

Results are presented as individual values, mean±standard deviation (SD) or mean±standard error of the mean (SEM) of determinations from separate animals and at least 3 independent experiments. Statistical analysis was performed using Prism 5 (GraphPad Software Inc) and P-

value<0.05 was considered significant (two-tailed Student's t test or one-way ANOVA with Bonferroni's post-hoc test).

2.4. *IN VIVO* EXPERIMENTS

High-fat diet mouse model of atherosclerosis

Male Apolipoprotein E knockout (ApoE KO) mice aged 8-10 weeks were fed a high-fat diet (Western type TD88137, 20-23% fat, 0.2% cholesterol; Harlan Teklad) and administered linear PS5 by intraperitoneal injection 3 days/week for 8 weeks. Groups of study: untreated control (n = 6), treated with low-dose PS5 (~38µg/mouse; n = 6), and treated with high-dose PS5 (~79µg/mouse; n = 7). At the study endpoint, 16 h-fasted mice were anesthetized (100 mg/kg ketamine and 15 mg/kg xylazine), saline-perfused and killed. Blood was collected by retro-orbital puncture. For biodistribution experiments, mice received a single intraperitoneal injection of TAMRA-labelled peptides (200µL, 0.6mg/mL) and killed after 6-24 hours. *Ex vivo* images of dissected tissues (liver, spleen, kidney, heart and aorta) were immediately recorded with an IVIS-Lumina system (Caliper Life Sciences Inc., Hopkinton, MA). Aortic tissues were also processed for confocal microscopy.

Atherosclerotic lesion analysis

To analyze the area and composition of atheroma plaques, aortic root was embedded in optimal cutting temperature medium (Sakura Finetek, Flemingweg, Netherlands) and cryosectioned. Sequential 8µm cross-sections (covering ~1000 µm from valve leaflets) were stained with Oil-red-O/hematoxylin. Atherosclerotic lesion area (μm^2) and neutral lipid content were quantified using Image-Pro Plus, and individual averages were calculated from 3-5 sections.

V. RESULTS AND DISCUSSIONS

1. NPM1 PROTEIN: AN AGGREGOMIC PERSPECTIVE IN ACUTE MYELOID LEUKEMIA

1.1. Results

1.1.1. NPM1 $_{264\text{-}272}$ fragment : design, structural and functional characterization

In this study, we investigated the role of a peptide covering the "basic amyloidogenic unit" of NPM1, the fragment 264-272 located in the N-term extremity of H2 region.

Thanks by Waltz server, we firstly predicted the tendency of the entire NPM1 wt to amyloid aggregation. This prediction revealed that the shortest amyloid core corresponds to the stretch 267-272 (KFINYV). Here, we have selected the frame 264-272 including also VEA residues (264-266) because they appeared partly involved in the aggregation process [169] and able to enhance aqueous solubility of the peptide to allow spectroscopic investigations.

The nonapeptide: Ac-^{264}VEAKFINYV^{272}-NH_2, named NPM1$_{264\text{-}272}$, was synthesized, identified through LC-MS and purified by RP-HPLC. The aggregation assays were performed using the peptide NPM1 $_{264\text{-}272}$ both pre-treated with hexafluoroisopropanol (HFIP) that usually determines a monomeric state [143], and in an partially aggregated in an "untreated state" [169].

The conformational properties of NPM1 $_{264\text{-}272}$, over time, were investigated in phosphate buffer and in **Figure 11A** are reported the overlays of CD spectra. As shown, the spectrum registered at t=0 presented a mixed α-helix+random coil state with a dominant unique absolute minimum at ~ 198 nm. The peptide aggregateswithin ~ 4 hours as suggested by the shift of the absolute minimum toward 218 nm, and by a subsequent CD signal decrease.

The tendency of this peptide to assume helical conformations is clearly indicated by HFIP and trifluoroethanol (TFE) titrations, reported in **Figure 11B** and **C**, respectively. The effects of TFE and HFIP as co-solvents in the conformational preferences are consistent with the formation of helical intermediates. As shown, the variation of θ_{222nm} values using fluorinated co-solvents (insets of **Figure 11 B-C)**indicates a greater helical content for HFIP with respect to TFE.

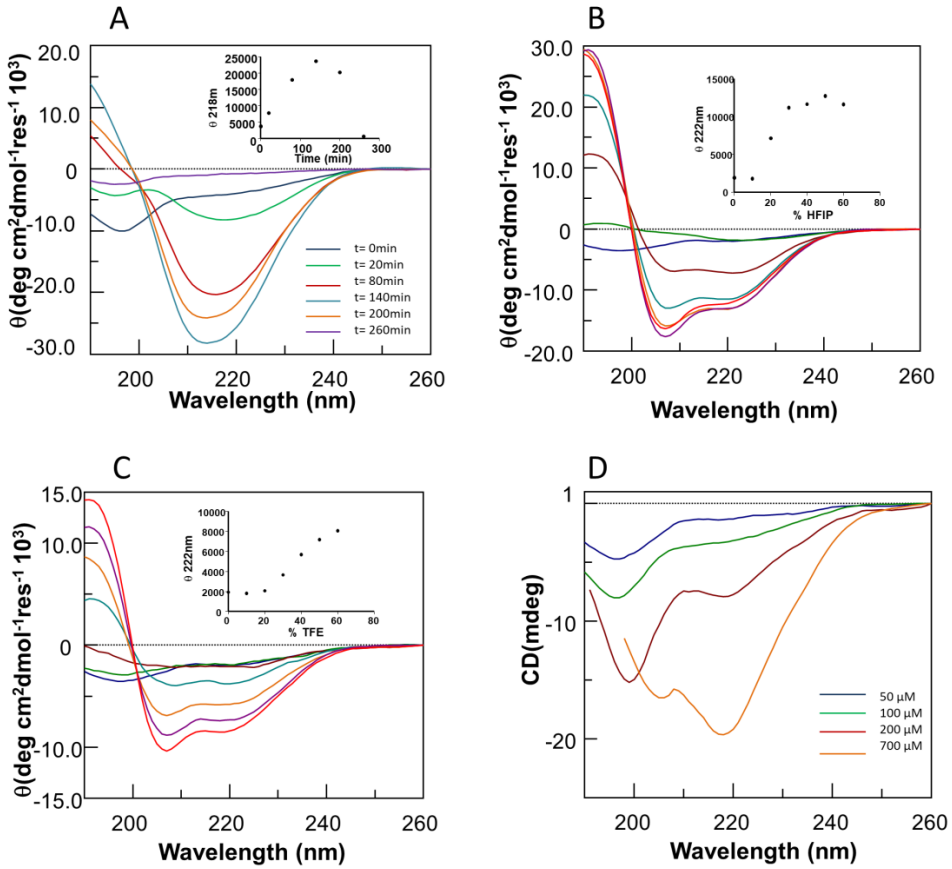

Figure 11. Conformational properties of NPM1 $_{264\text{-}272}$: Overlay of CD spectra **(A)** over time, **(B)** HFIP titration, **(C)** TFE titration, **(D)** over concentration.

As expected, the CD spectra of the untreated peptide exhibits at t=0 a more pronounced negative band centred at 218 nm (in addition to that at ~ 200 nm), indicating a higher structured content (helix+β) and, the aggregation processappears faster than that of treated peptide (**Figure 12A**).

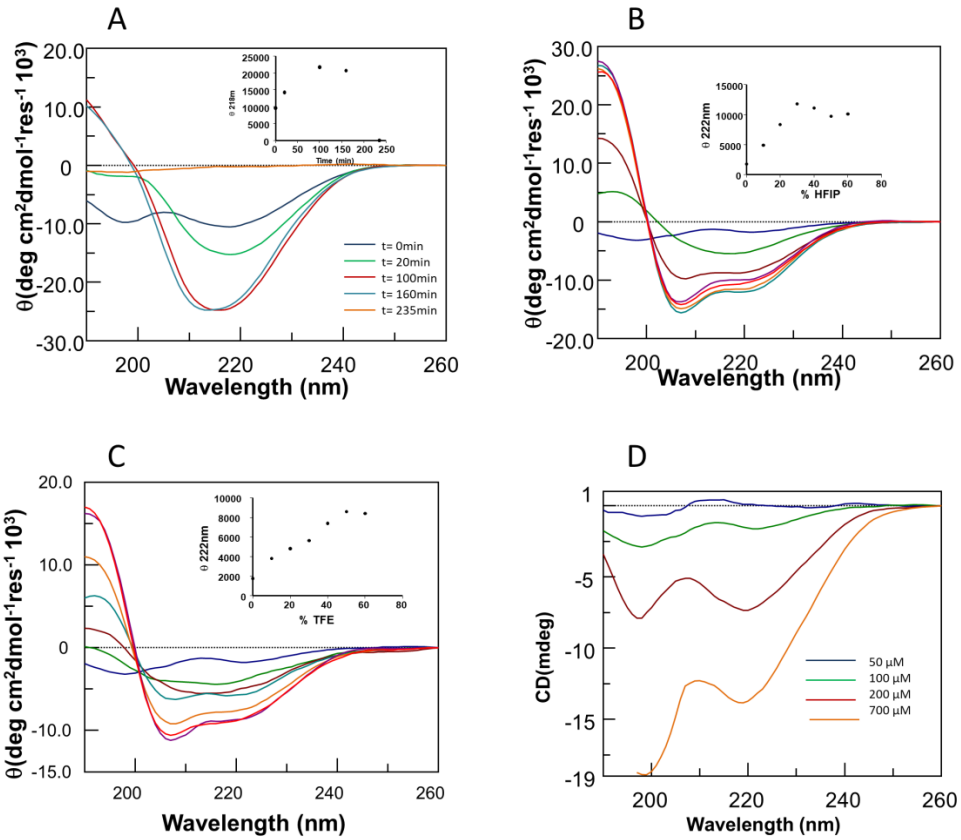

Figure 12. Conformational properties of untreated NPM1 $_{264\text{-}272}$: Overlay of CD spectra **(A)** over time, **(B)** HFIP titration, **(C)** TFE titration, **(D)** over concentration.

The kinetic of amyloid fibril formation of NPM1 $_{264\text{-}272}$was analyzed by both thioflavin T (ThT) fluorescence emission at 482 nm [170](**Figure 13A**, **C**) and tyrosine (Tyr) emission at 303 nm [171](**Figure 13B**, **D**). For ThT assays, the fluorescence intensity increased with time: in detail, the aggregation of NPM1 $_{264\text{-}272}$ took place with a $t_{1/2}$ at 210 min after incubation while, as expected, the typical concave shape of the profile for untreated sample (**Figure 13C**) clearly indicated the presence of pre-aggregated states [172-173]. This behaviour was corroborated by the analysis of Tyr emission for which the enhancement of intensity suggests a progressive higher exposure of Tyr residues in the aggregation process as already reported for γ-B-crystalline and HEWL aggregation processes [174]. In addition, the initial Tyr fluorescence intensities were significantly different between treated and untreated samples (126 and 365 a.u., respectively)suggesting different conformational and hydrogen bonding network in the systems in the monomeric and partially aggregated states (**Figure 13B** and **D**).

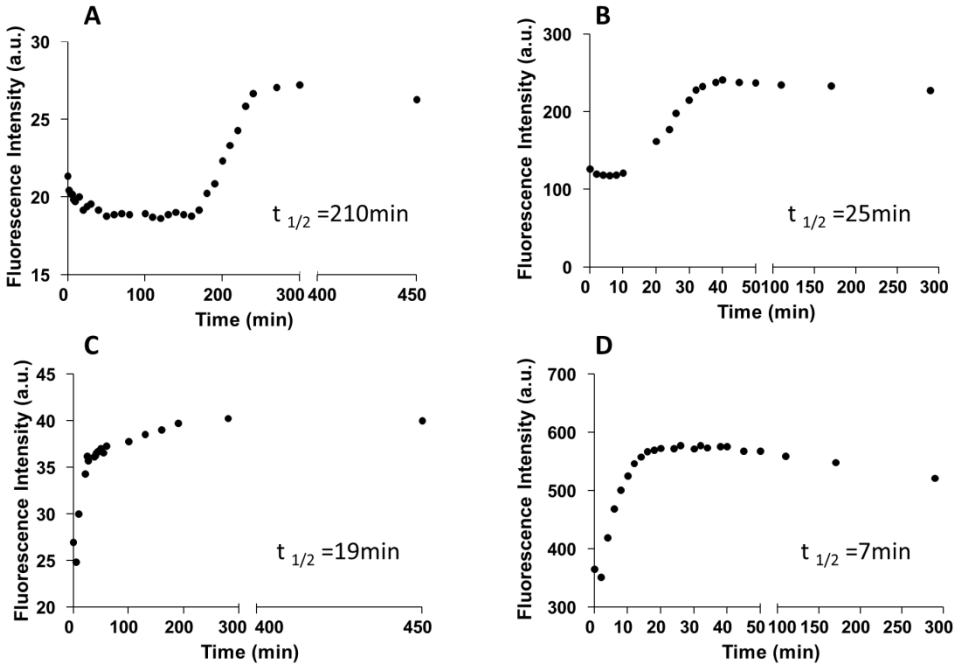

Figure 13. Kinetic of amyloid aggregation of HFIP treated **A-B**, HFIP untreated **C-D**. Time course of ThT fluorescence emission intensity (ThT) (A-C) and Tyr (B-D). Data are representative of three independent experiments.

These considerations were further corroborated bybinding assays with ANS (8-anilinonaphthalene-1-sulfonate ammonium salt) reported in **Figure 14**, that provide clues on the exposure of hydrophobic amino acids on the surface of aggregating sequences [175-177]. The differences in the variations of fluorescence intensity of ANS, between untreated and treated peptide indicated a higher degree of solvent exposure of hydrophobic clusters for the untreated sample, as confirmed by the shifts of the wavelength of maximum emission (λ_{max}) (**Figure14**). In both cases, the variations of ANS fluorescence signal appeared very small due to the small size of the aggregating sequence (maximum intensity 10 a.u.)

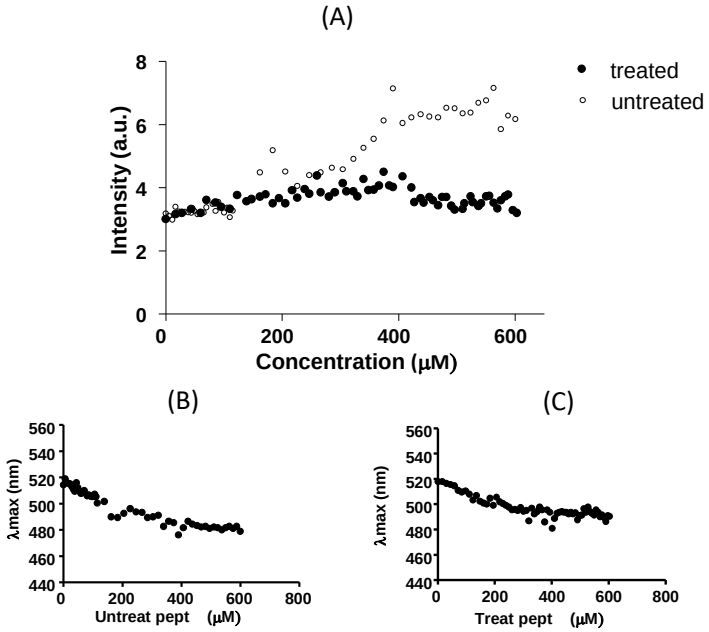

Figure 14. (A) Fluorescence intensity emission of the ANS fluorophore at 475 nm versus the concentration of peptide NPM1 $_{264-272}$, **(B-C)** Plot of λmax variations at different peptides concentrations.

With the aim to deepen the aggregation properties of NPM1 $_{264-272}$ fragment, we carried out an amyloid seeding assay (ASA) monitored by ThT fluorescence emission [178]. As expected the addition of preformed- seeds of NPM1 $_{264-272}$ to the reaction of aggregation of peptide accelerates amyloid formation, compared with control (**Figure15A**). The $t_{1/2}$ for NPM1 $_{264-272}$-seeded reaction was 185 min, resulting in a ~12% reduction, compared with unseeded reaction ($t_{1/2}$=210 min) (Fig. 3A). By comparing ThT fluorescence intensity at 400 min of seeded reaction versus control reaction we found substantially greater signals from NPM1 $_{264-272}$-seeded reaction, suggesting greater levels of oligomerization.

On the other hand, a disaggregation assay was carried out, in which, we monitored ThT emission signal upon the addition of Epigallocatechin-3-gallate (EGCG), a known inhibitor of the amyloid oligomers, [179] to the untreated peptide as reported in **Figure15B**: after the addition, the fluorescence signal significantly decreased with time. This assay confirmed the presence of soluble aggregates in the untreated sample, since a decrease of ThT fluorescence within the first 15 minutes was observed.

Furthermore, we evaluated the thermodynamic parameters of the interaction between NPM1 $_{264-272}$ peptide and EGCG through isothermal titration calorimetry (ITC) [180]. In particular, by titrating aliquots of EGCG into peptide solution, the downward ITC titration peaks demonstrate that the

association between EGCG and the peptide is an exothermic reaction, as shown in **Figure15C**. Data reached saturation and allowed an estimation of the thermodynamic parameters. Best fit of experimental data with the sequential binding model (n=2) provided data reported in **Table 2**, in agreement with similar experiments [181].

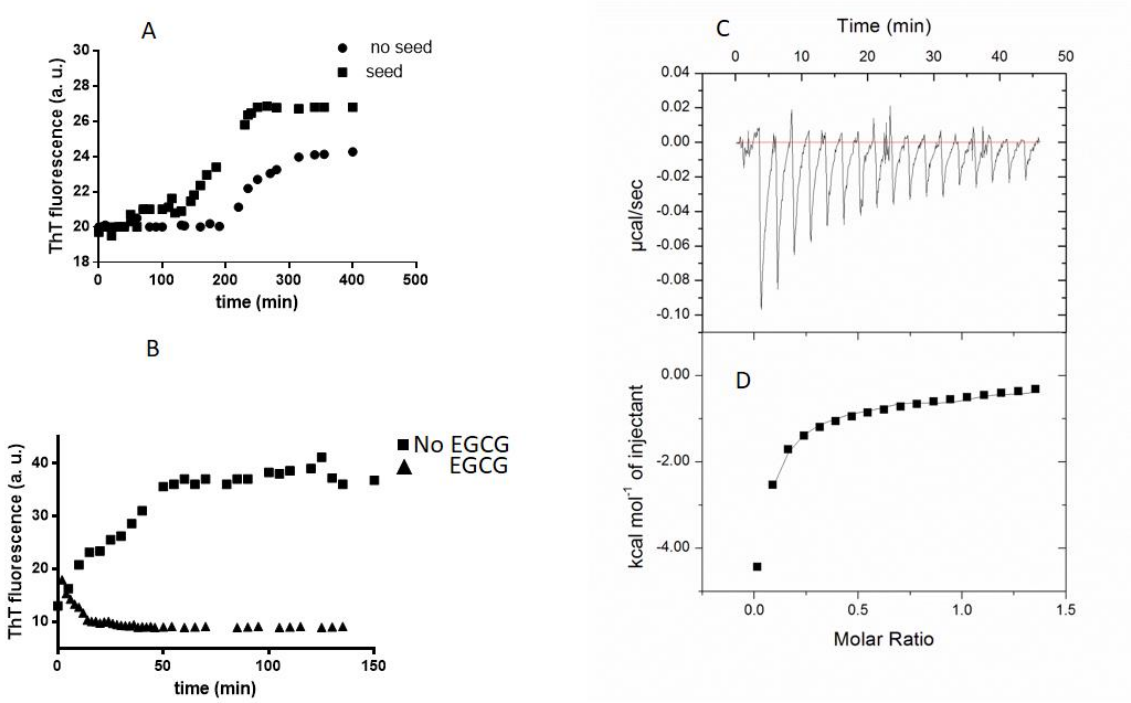

Figure 15. Amyloidogenic properties of soluble aggregates of NPM1 $_{264\text{-}272}$ **(A)** Kinetic profiles of amyloid formation in the presence of pre-formed seeds of NPM1 $_{264\text{-}272}$ monitored by ThT fluorescence over time, **(B)** EGCG disaggregation assay towards NPM1 267-271 oligomers (2:1 EGCG: peptide), **(C)** ITC data of EGCG (1mM, at pH 7.2, 25 °C) titration to NPM1 264-271 (200 µM). Thermodynamic parameters were estimated after subtracting the control experiment (EGCG in buffer HBS).

Table 2: Calorimetric analysis of the interaction of the NPM1 $_{264\text{-}272}$with ECGC

Ka_1 ($M^{-1} \times 10^{-3}$)	ΔH_1 (kcal/mol)	ΔS_1 (cal/mol/deg)	Ka_2 ($M^{-1} \times 10^{-3}$)	ΔH_2 (kcal/mol)	ΔS_2 (cal/mol/deg)
2.4±0.3	-29.8±0.5	-83,1	865±1	28±5	123

To investigate the oligomerization level of aggregation of monomeric NPM1 $_{264\text{-}272}$, a time course of mass experiments [182] was carried out. The deconvolution of ESI mass spectra registered at t=0 and t=70 minutes is reported in **Figure 16**.

NPM1 $_{264-272}$, freshly dissolved, presented peaks due to the formation of few self-assemblies at low aggregation state (up to n = 10) as also reported for similar systems [183] even if a prevalent monomeric state can be outlined. During time the progressive presences of new peaks at higher MWs clearly indicated an aggregation process: in **Figure 16B** the deconvolution of ESI mass spectra, after 70 minutes from the dissolution, presented many new peaks due to much moreoligomeric states consisting of higher aggregation levels (up to n = 58).

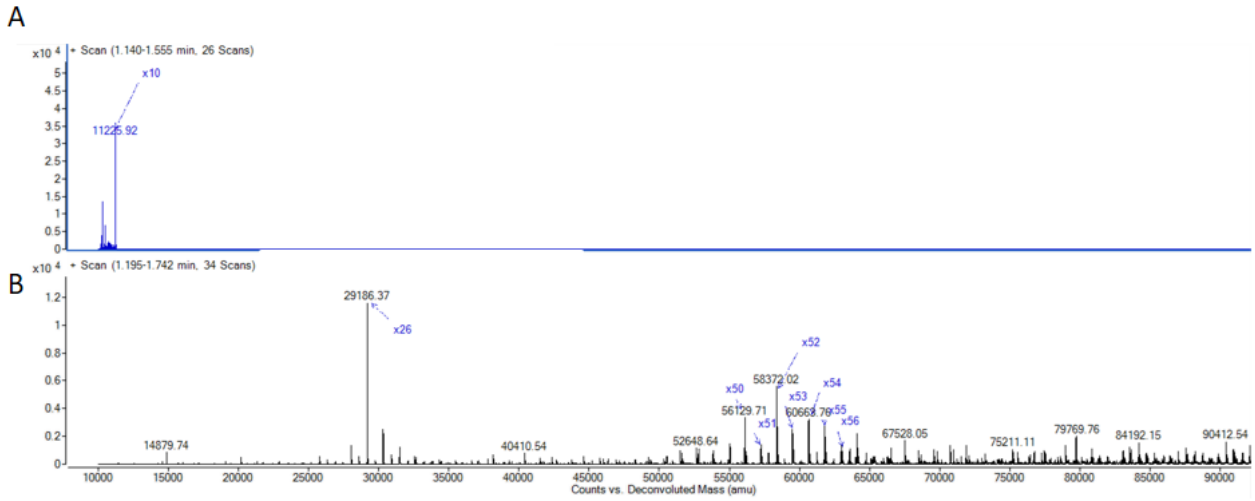

Figure 16. Deconvolution of ESI mass spectra showing peptide aggregation stability for NPM1 $_{264-272}$ at 250 µM dissolved in ammonium bicarbonate buffer at **(A)** t=0 and **(B)** t=70 min.

To gain deeper insights into the aggregated state the NPM1 $_{264-272}$ fragment and in its molecular organization, Scanning Electron Microscopy (SEM) and Wide-Angle X-ray Scattering (WAXS) experiments were carried out. SEM micrographs, reported in **Figure17**, were obtained at two different concentrations (500 and 1500 µM) and confirmed the capability of the peptide to assemble and to form fibers with a certain morphological variability in dependence of concentration.

Flat nanostructures were observable with widths of size ~16-21 µm and ~10-13 µm respectively for the lower and the higher concentration along their full lengths (~1 and 0.6 mm, respectively) (**Figure17A, B, D, E**). In both cases fibers appeared formed by the aggregation of smaller tapes (**Figure 17 C, F**) with regular size at 500 µM (~30 nm width) and with very variable dimensions for the 1500 µM (17-90 nm width).

Noticeable lower concentration nanostructures presented a flat ribbon shape (**Figure17A**), while those at higher concentration a twisted ribbon (**Figure17D**), as already reported for amyloid peptides having helical intermediates [184].

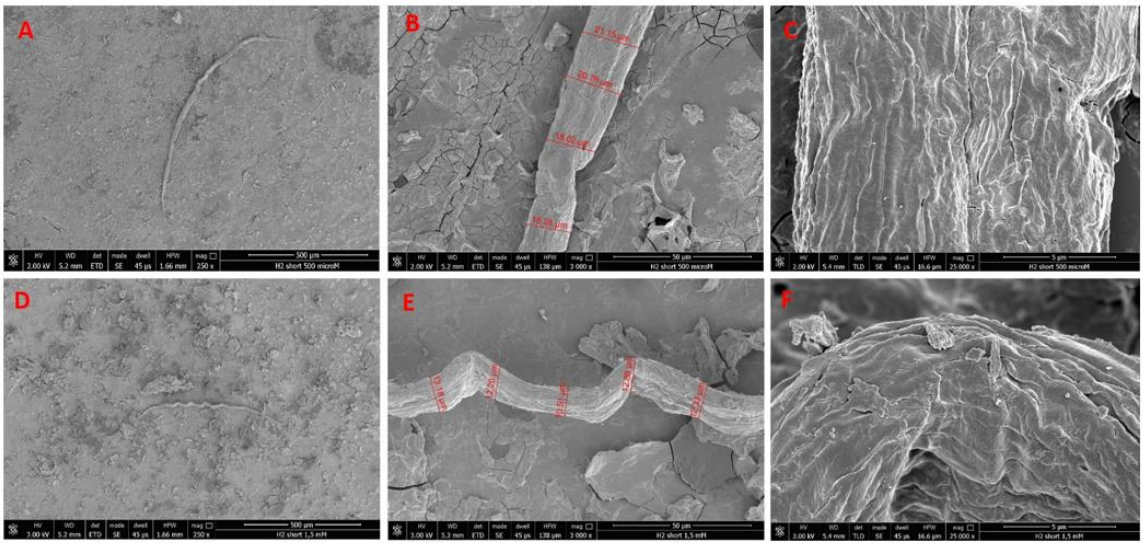

Figure 17.SEM micrographs for nanostructures of NPM1 $_{264\text{-}272}$ at 500 µM (A-C) and 1500 µM (D-F): overviews of the surface of fibers at 250x, 500 µm (A- D); details with measures at 3000x, 50 µm (B- E); more details at 25000x, 5 µm (C- F).

The fibrils were also analyzed through WAXS investigations [184] and in **Figure18** the results of the experiments are summarized: Fig. 6A shows the investigated fiber as appears under an optical microscope (red bar=0.1 mm); **Figure18B** the 2D WAXS diffraction pattern collected on a fiber deriving from a solution at 2.6 mM; **Figure18C** the 1D WAXS diffraction pattern obtained after centering, calibration and folding of the 2D WAXS data in **Figure18B**[185]. The 2D WAXS pattern shows the typical cross-β diffraction features, with the relevant diffraction peaks occurring along two orthogonal directions: the meridional direction which coincides with the fiber axis and the equatorial direction perpendicular to it (highlighted by dotted white arrows). The position of the equatorial peaks, labelled as e1, e2 and e3 in **Figure18C**, as well as the position of the m1 meridional peak are reported in **Table 3**. Two main important peaks, the meridional m1 (d=4.8Å) and the equatorial e1 (d=12.6Å), correspond to the typical β-strand and β-sheet distances of an amyloid structure, respectively [186].

Table 3: Meridional and equatorial fiber diffraction peaks

Label	q [Å^{-1}]	d [Å]
e1	0.5	12.6
e2	0.7	9.0
e3	0.95	6.6
m1	1.3	4.8

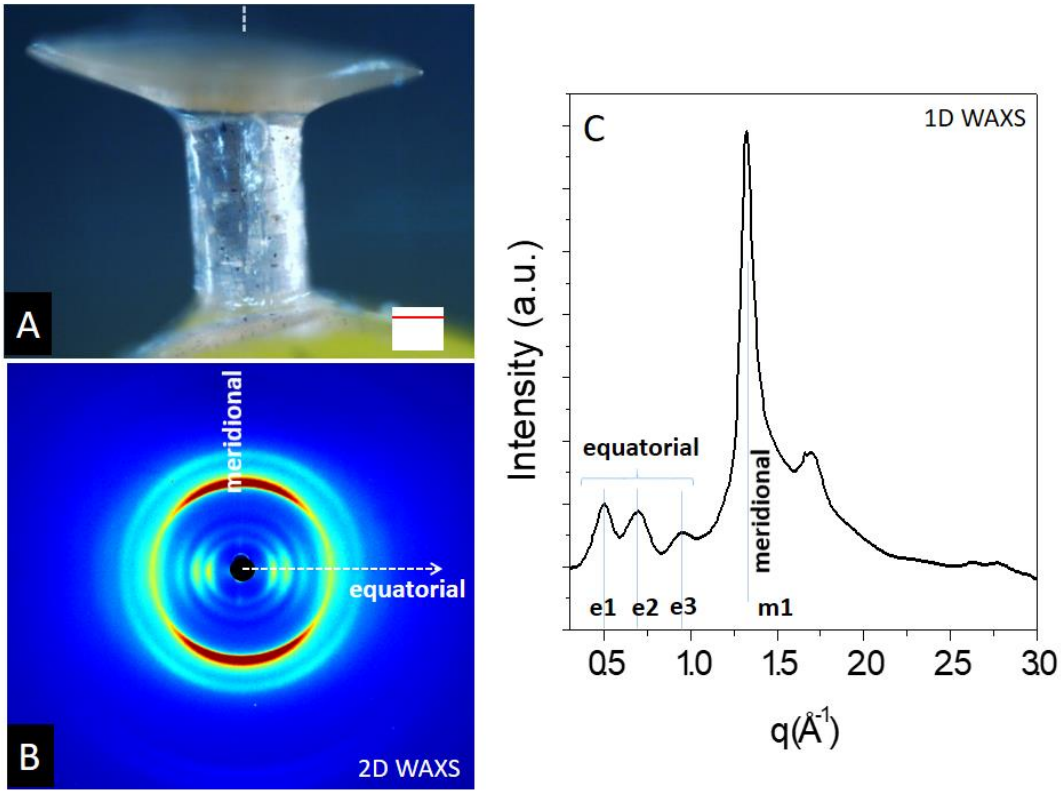

Figure18. WAXS analysis of NPM1 $_{264\text{-}272}$ derived fiber (A) the analyzed fiber as seen under the optical microscope (red bar=0.1 mm); (B) 2D WAXS fiber diffraction pattern with white dotted arrows along the fiber axis (meridional) and perpendicular to it (equatorial); (C) 1D WAXS fiber diffraction pattern.

1.1.2. AML H3 mutated peptides covering NPM $_{279\text{-}286}$: design, structural and functional characterization

In this work, the properties of sequences corresponding to AML mutations we investigate. In detail, we synthesized peptides, reported in **Table 4**, in two different forms: "elongated" form including 279-286 fragment that is common to all sequences and a "shorter" version covering only the mutated fragments. To deepen a potential link between leukomogenesis and amyloid aggregation the properties of sequences corresponding to AML mutationswere investigate. Peptides covering h3 sequence in wt and AML mutated version were synthesized (**Table 4**), in two different forms: "elongated" form including 279-286 fragment that is common to all sequences and a "shorter" version covering only the mutated fragments.

Table 4: H3 peptide primary sequences analyzed in this study. In bold residues constituting short peptides, underlined tryptophans belong to the NoLS.

Mutant	**Sequence**	**MW (amu) Extended/short**
Wild-type	^{279}TDQEAIQ**DLWQWRKSL**^{294}	2058.2/1272.45
Mutant A	^{279}TDQEAIQ**DLCLAVEEVSLRK**^{298}	2301.6/1515.8
Mutant B	^{279}TDQEAIQ**DLCMAVEEVSLRK**^{298}	2319.6/1533.8
Mutant C	^{279}TDQEAIQ**DLCVAVEEVSLRK**^{298}	2287.5/1501.7
Mutant E	^{279}TDQEAIQ**DLWQSLAQVSLRK**^{298}	2370.1/1584.8
Mutant F	^{279}TDQEAIQ**DLWQSLEKVSLRK**^{298}	2428.7/1642.9

Through ThT assay, we analyzed the tendency of mutated sequences to aggregate in amyloid-like way at high micromolar concentrations. As shown in **Figure 19**, both H3 wt short and extended peptides exhibit low values of ThT fluorescence at t=0, which did not increase with time. On the contrary, each mutated sequence shows an increase of ThT fluorescence intensity. The N-term extension retards the aggregation. Interestingly, the mutB short peptide appeared already aggregated, since it shows a high value of ThT fluorescence intensity at t=0, as also showed by mutA and mutC short sequences. Contrary to mutB, mutA and mutC exhibit a further

enhancement of fluorescence signal, presumably due to the formation of soluble aggregates of higher-order of oligomerization with respect to those observed at t=0, with very different kinetics (**Table 5**).

Table 5: Aggregation kinetics (t½) of the H3 peptides following ThT emission.

Peptide	**$t_{1/2}$ (h)**		**Fluorescence Intensity**	
	extended	**short**	**extended**	**short**
H3 wt	Not valuable		Not valuable	
mutA	46[187]	19	94.7	362
mutB	41	Already aggregated	383	150
mutC	71; 113	7	619, 1102	470
mutE	5,2	0,138	3302	3746
mutF	67	1,4	80	837

Noticeably for mutC extended sequence, the fluorescence intensity displays two distinct transitions, suggesting a seeding effect of first soluble aggregates to secondly achieve higher levels of oligomerization [188].

In order to evaluate potential conformational transitions during aggregation, CD experiments over time were carried out(**Figure 20**). At the beginning, all short mutated peptides (**Figure 20**, right panel) are in a mixed α-helix+random coil states, characterized by a predominant unique absolute minimum at $\lambda \leq 200$ nm, and a slight shoulder at ~222 nm. Differently, H3 wt short appeared partially structured, presenting the negative band at higher wavelength (204 nm), a positive value at 190 nm and a more pronounced minimum at 222 nm which indicate more regular structures. The extended sequences (**Figure 20**, left panel) showed more unordered profiles, with, in some cases (mut A-C extended) the minimum at wavelength lower than 200 nm.

In the time, all H3-mutated short peptides tended to precipitate and/or aggregate as suggested by a progressive decrease of the Cotton effect (**Figure 20**, right panel). As expected, H3 wt short showed no conformation variations, with a slight signal reduction only after 5.5 days. The aggregation of mutated sequences showed several differences; mutF short, for examples, presented a decrease of CD signal after only 4 days while most of them much earlier: after 4 hours for mutA, mutB and mutC short and after 6 hours for mutE short.

Moreover, the CD spectra of mutC and mutE short present large minima centered at ~ 220 nm at different times, 4 and 22 h for mutC and E short, respectively suggesting a conformational transition toward β-structures associated with aggregation. Differently from H3 wt extended, whose CD signal decreased consistently only after 137 hours [187], extended sequences showed to aggregate/precipitate as the loss of Cotton effect is observed after 30-90 hours.

These data clearly indicate a preferential tendency of the mutC and mutF sequences to aggregate with respect to A-D group (including sequences lacking both Trp of the NoLS) and E-F group whose peptides bear one of the two Ws of the NoLS), respectively, with different kinetics. For these reasons, we further analyzed sequences corresponding to mutF and mutC in comparison with wt forms, employing different techniques.

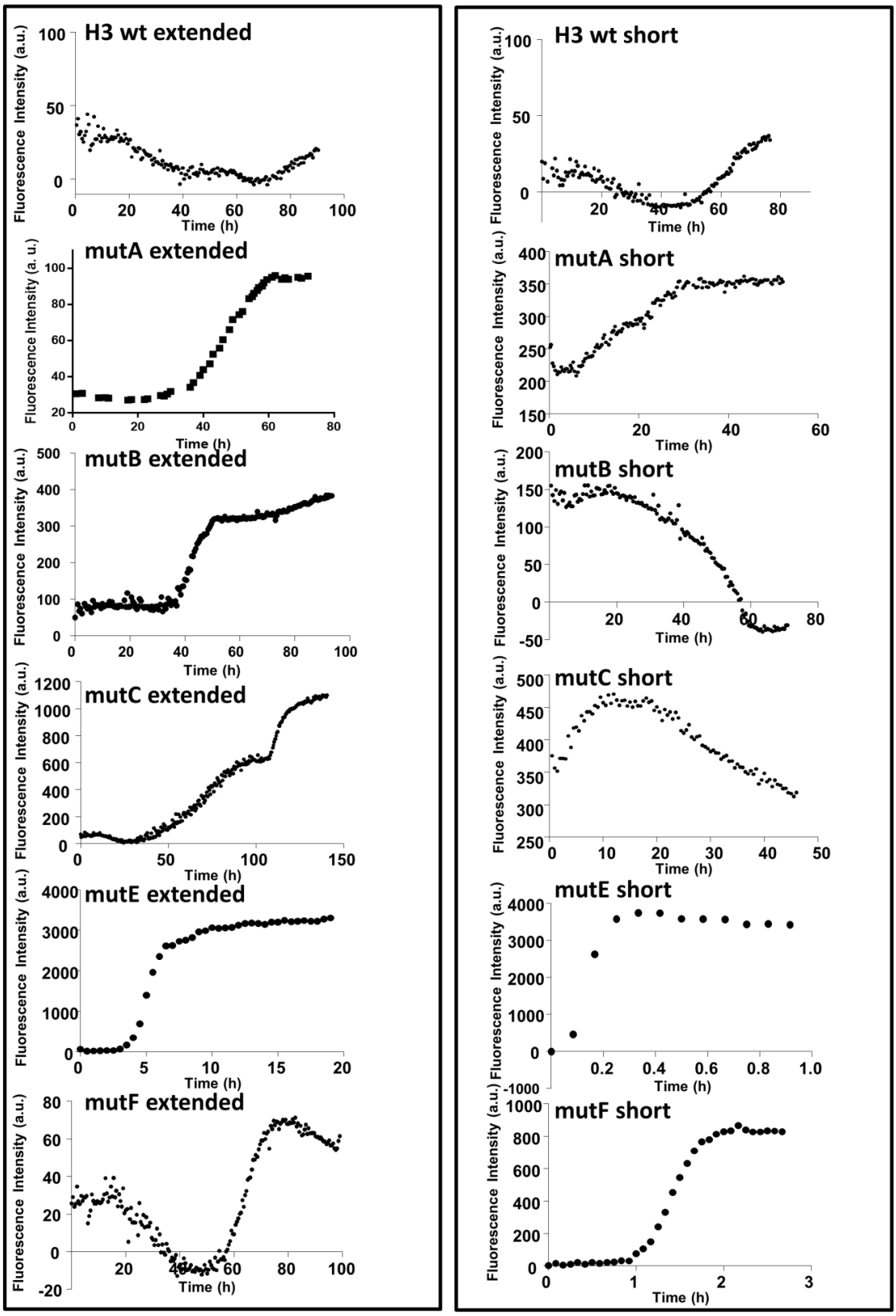

Figure 19. Time course of ThT fluorescence emission intensity of extended, left panel, short, right panel, H3 sequences.

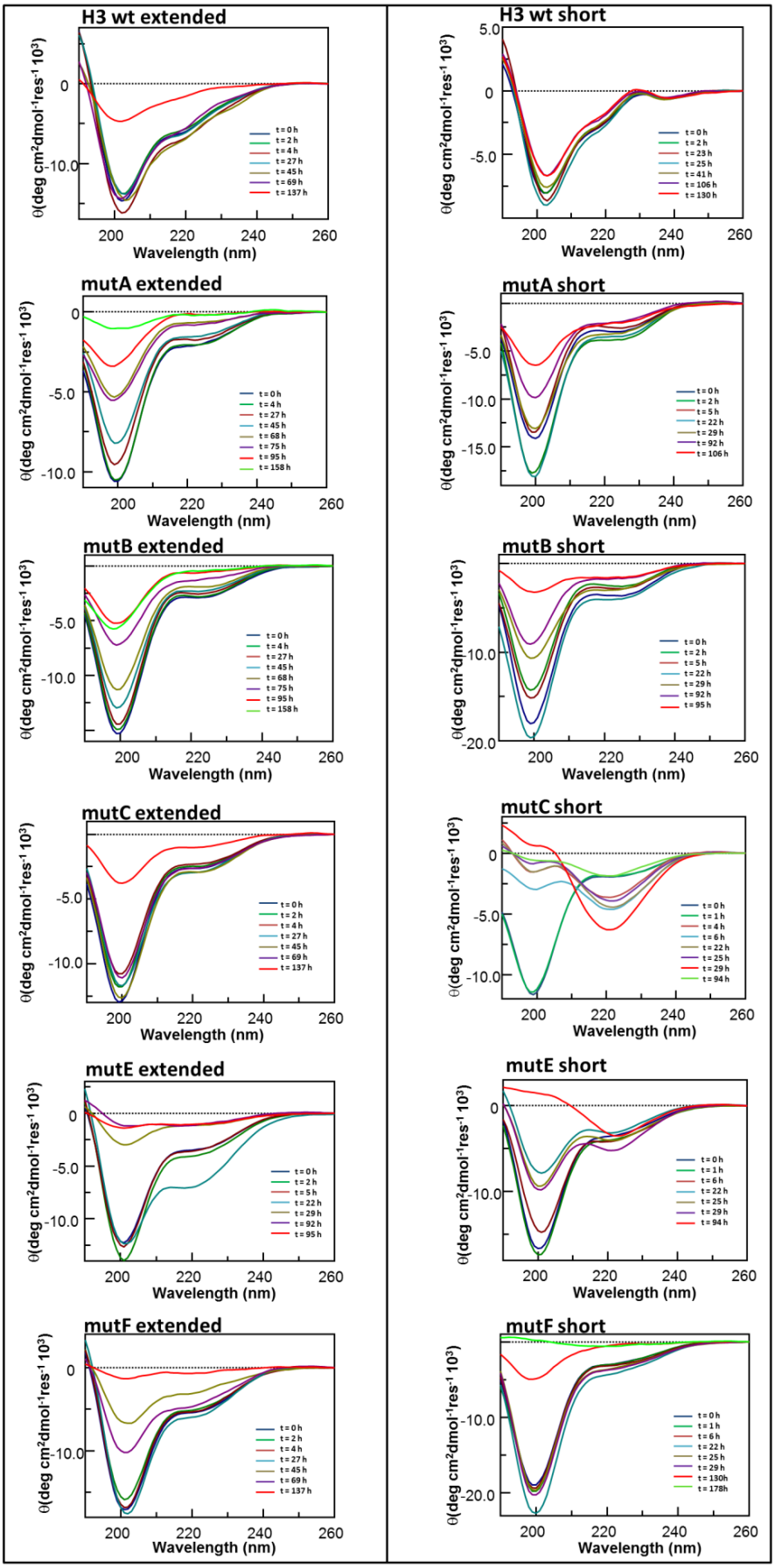

Figure 20. Overlay of CD spectra over time of extended left panel and short, right panel, H3 sequences.

To further analyze typical amyloid properties of mutC and mutF sequences, Congo Red (CR) assay was employed (**Figure 21**). As observed, both extended peptides (**Figure 21**, left panel), reached maxima of absorbance and shift of $\lambda_{max,}$ from 488 nm to a maximum of 563 nm (for mutF short), later with respect to shorter ones, even if mutF extended at 100 h exhibits a lower absorbance value with respect to 40 h, while the mutC signal is linear over time. This trend could be attributed to a lower solubility of mutF extended aggregates with respect to mutC, confirming CD analysis.

Comparably, mutC short gave a constant signal in the time interval 16-100 h , while the reduction and the blue-shift of λ_{max} for mutF short in the interval 24-40 h suggests the beginning of insoluble fibrils.

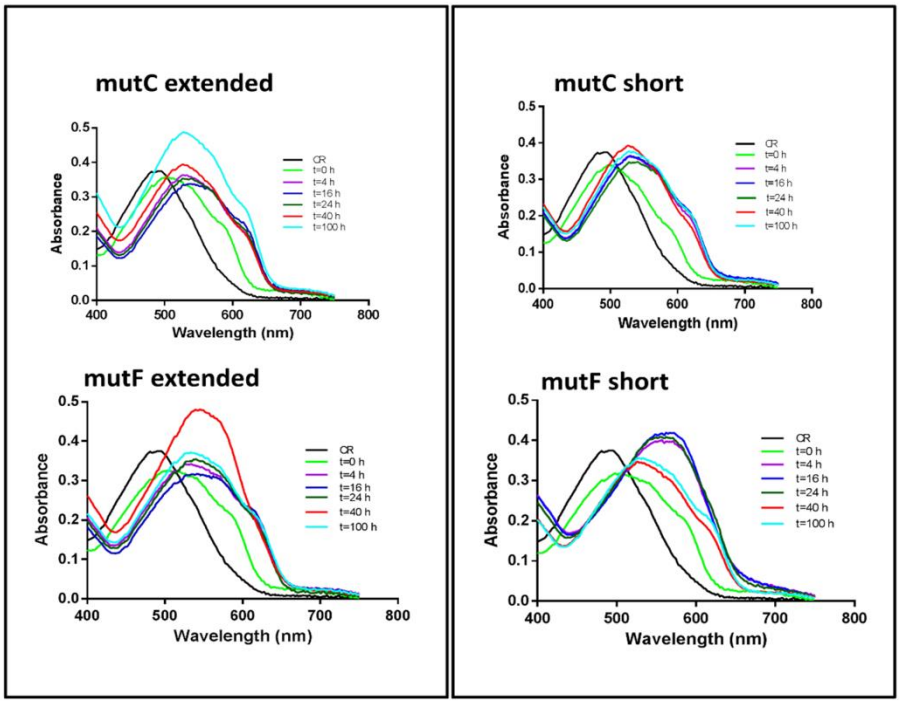

Figure 21.Time course of Congo Red absorbance spectra of: mutC extended; mutC short; mutF extended; mutF short.

Furthermore,we observed that all these four sequences presented an intrinsic fluorescence, often associated to amyloid-like fibrillar structure of proteins and peptides [189].Interestingly, the emission spectra resulted dependent on the excitation wavelength, as reported in **Figure 22**.

Particularly, the emission peak of mutC red-shifted from 420 to ~450 nm when excited at 336 - 440 nm, while the emission peak of mutF moved from 380 nm to ~420 nm. This phenomenon is not related to any particular residue or peptide sequence (i. e. the presence of aromatic residues)

rather it arises from charge delocalization along the backbone of the fibers in the amyloid structures.

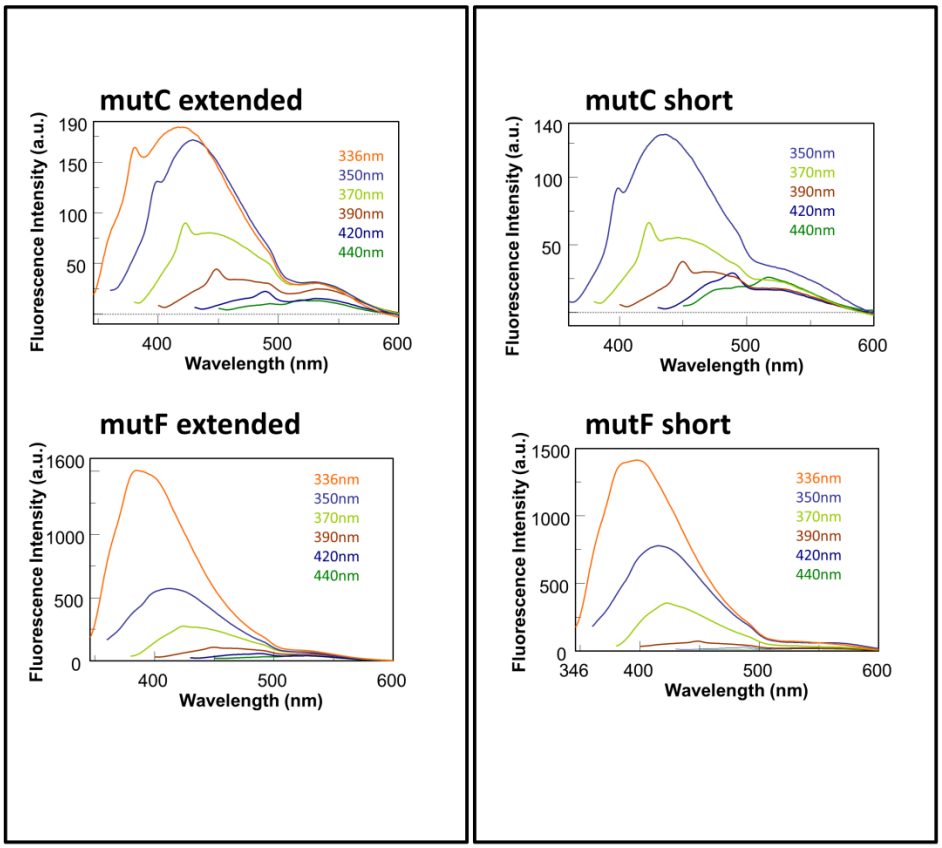

Figure 22. Changes in the intrinsic fluorescence spectra of several H3 peptides at different excitation wavelengths of mutC extended, mutC short, mutF extended and mutF short.

Fluorescence lifetime measurements also confirmed our previous date. Indeed, the fluorescence decay profiles of H3 mutated oligomers exhibited multi-exponential decay kinetics (**Figure 23**, upper) with bi/tri-exponential fitting, as reported in **Figure 23**, lower. Data fitting provided an average lifetime value of 0.28 ns for mutC short sequence with two lifetime components of 0.27 (99%), 1.35 (1%) and average lifetimes of 1.499, 1.12, 1.15 ns for respectively extended mutC, short and extended mutF, with three components each.

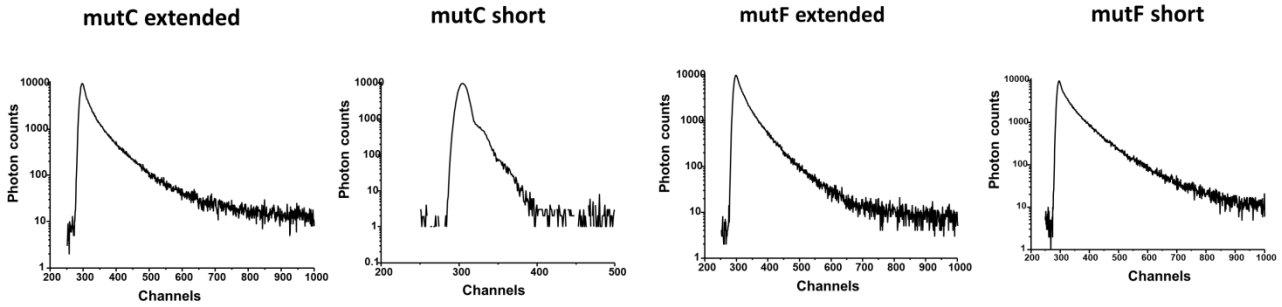

Peptide	t_1 (ns)	a_1	t_2 (ns)	a_2	t_3 (ns)	a_3	t average (ns)	c^2
mutC short	0.27	0.99	1.35	0.01	/	/	0.28	1.25
mutC extended	0.74	0.82	3.98	0.15	10.57	0.03	1.49	1.21
mutF short	0.30	0.84	3.55	0.12	10.58	0.04	1.12	1.37
mutF extended	0.32	0.69	1.94	0.24	6.55	0.07	1.15	1.19

Figure 23. Upper: Fluorescence decays of mutF extended; mutC extended; mutF short; mutC short. Lower: Fluorescence lifetime components of several mutated peptides (λex= 336 nm, λem = 450 nm), where αi is amplitude of the lifetime component and τi is the respective lifetime value.

To gain deeper insights into the aggregated states of H3 mutC and mutF sequences and in their molecular organization, Scanning Electron Microscopy (SEM) and Wide-Angle X-ray Scattering (WAXS) studies were carried out. Sequences showed distinct self-assembled morphologies depending on size, concentration and time. SEM micrographs registered on samples of short and extended mutC and mutF sequences are reported in **Figure 24**and**25**, respectively.

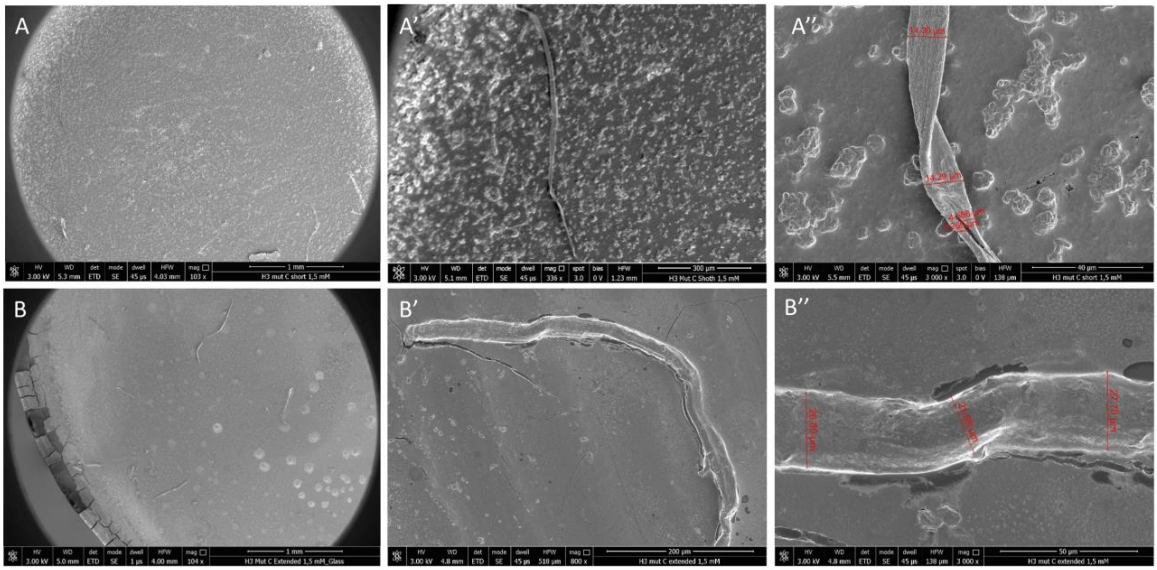

Figure 24. Micrographs of mutC short (A) and extended (B): overviews at 103x (A) and 104x (B), 1mm scale bar; details at 336x (A', 300 µm scale bar) and 800x (B', 200µm scale bar); morphologies of surfaces at 3000x (A'', 40µm scale bar; B'', 50µm scale bar).

MutC extended (**Figure 24B**) demonstrated rich of fibers with similar length (~900 µm) and thickness in the range 22-29 µm, while mutC short (**Figure 24A**) showed thin and ribbon-like fibers, sometimes wrapped around themselves, with length of ~800 µm and width of 2-14 µm.

MutF short and extended provided different morphologies as shown in **Figure 25**. A widespread distribution of circular structures (**Figure 25 A, A'**) with sizes of 22-26 µm are visible: these unusual vesicle-like entities partly hide very long fibers (~ 2.4 mm). Several fibers appeared wrapped around themselves (A', A''), with a thickness in the range 6.3-11.2 µm. On the other hand, mutF extended presented long fibers (1.6 mm), only partially wrapped and with larger thickness with respect to short sequence (8-18 µm, **Figure 25 B, B''**), in which vesicle-like structures were absent.

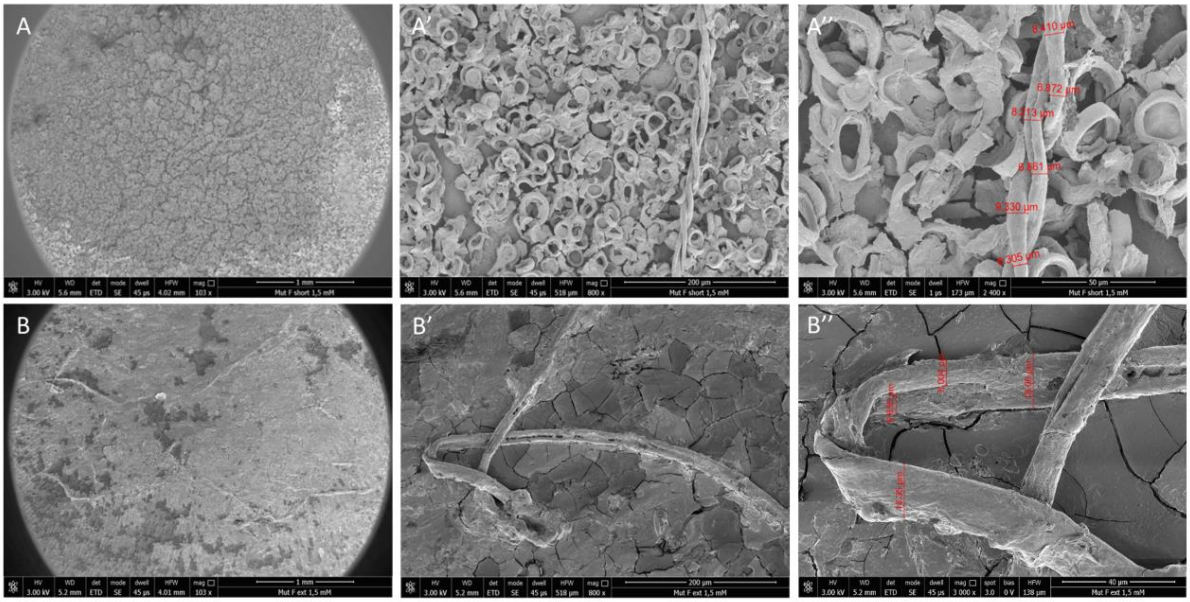

Figure 25. Micrographs of mutF short (A) and extended (B): overviews at 103x, 1mm scale bar (A, B); details at 800x, 200µm scale bar (A', B'); morphologies of surfaces at 2400x (A'', 50 µm scale bar) and 3000x (B'', 40µm scale bar).

Under the same conditions, micrographs deriving from H3 wt sequences displayed nanostructures poorly defined and highly dispersed in the matrix (**Figure 26**).

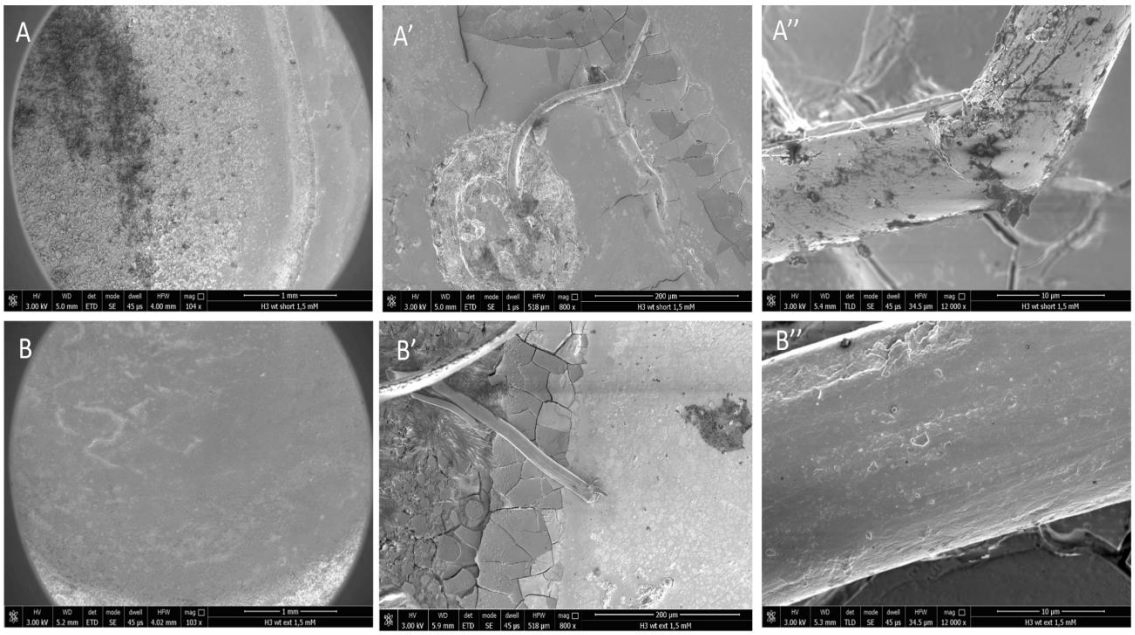

Figure 26. Micrographs of H3 wt short (A) and extended (B): overviews at 103-104x, 1mm (A,B), structures details at 800x, 200µm (A',B') and morphologies of surfaces at 12000x, 10µm (A'',B''). Micrographs deriving from H3 wt short (A) and extended (B): both contain weak nanostructures of about 300 µm in length, with a width greater in the H3 wt extended respect to the short one (16 and 19 µm respectively, A' and B'). Surface morphologies are poorly defined (A'' and B'') because fibers are dispersed in the matrix.

The observed sequence-dependent morphological arrangements of H3 mutated peptides mainly arise because of different extent of non-covalent interactions in the self-assembling nanostructures. Peptides of mutF type contain an aromatic residue with 3 leucine and one valine but vesicle-like molecular arrangements resulted visible only in the short version of this sequence. Maybe the short size of the sequence partially hampers π–π stacking along with H-bonding interactions that could lead to a compact fibrillar network as occur in the extended version of mutF peptide.

Only for the short mutF peptide a sufficiently large fiber for X-ray analysis was successfully obtained, following the "stretch frame method" with a length of about 500 µm and a thickness of about 700 µm, (**Figure 27A**).

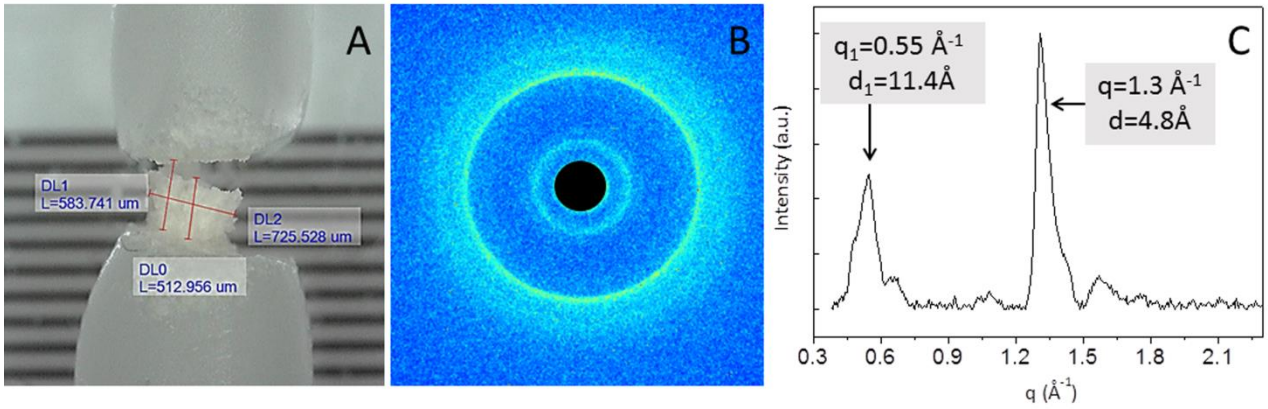

Figure 27.(A) Optical microscope image of H3 mutF short dried fiber between capillaries; **(B)** 2D-WAXS pattern collected on H3 mutF short dried fiber; **(C)** 1D-WAXS corresponding profile.

The two dimensional (2D) WAXS [145-146] pattern collected on the H3 peptide mutF short dried sample showed not highly oriented fiber, as evidenced by the presence of fully rings instead of arcs[39](**Figure 27B**). The 2D pattern, once centered, calibrated and radially folded into 1D profile, is displayed in **Figure 27C**. This profile presents two main reflections at q = 0.55 ±0.03 $Å^{-1}$ (d = 11.4 ± 0.5 $Å^{-1}$) and q = 1.3 ± 0.03 $Å^{-1}$ (d = 4.8 ±0.5 $Å^{-1}$), that correspond to the typical distances between two-distinct β-sheet and between adjacent peptide backbones organized in β-strands, respectively [145-146].

In order to evaluate the H3-derived peptides cytotoxicity, *in vitro* experiments, in human SH-SY5Y neuroblastoma cells were performed. As shown in **Figure 28 A-B**, the aggregated forms of H3 derived peptides could affect intracellular Ca^{2+} levels, that is an early event in the toxic amyloid pathway [190]. As expected, non-aggregated peptides at t0 did not cause any alteration in intracellular Ca^{2+} levels while, after 6 h of incubation, the mutC short peptide generated a significant Ca^{2+} influx, which progressively increased over aggregation time. The extended mutC and both forms of mutF started to affect Ca^{2+} homeostasis if aggregated at least for 24 h. The wild-type peptides caused a small increase in Ca^{2+} influx only after 72 h of aggregation.

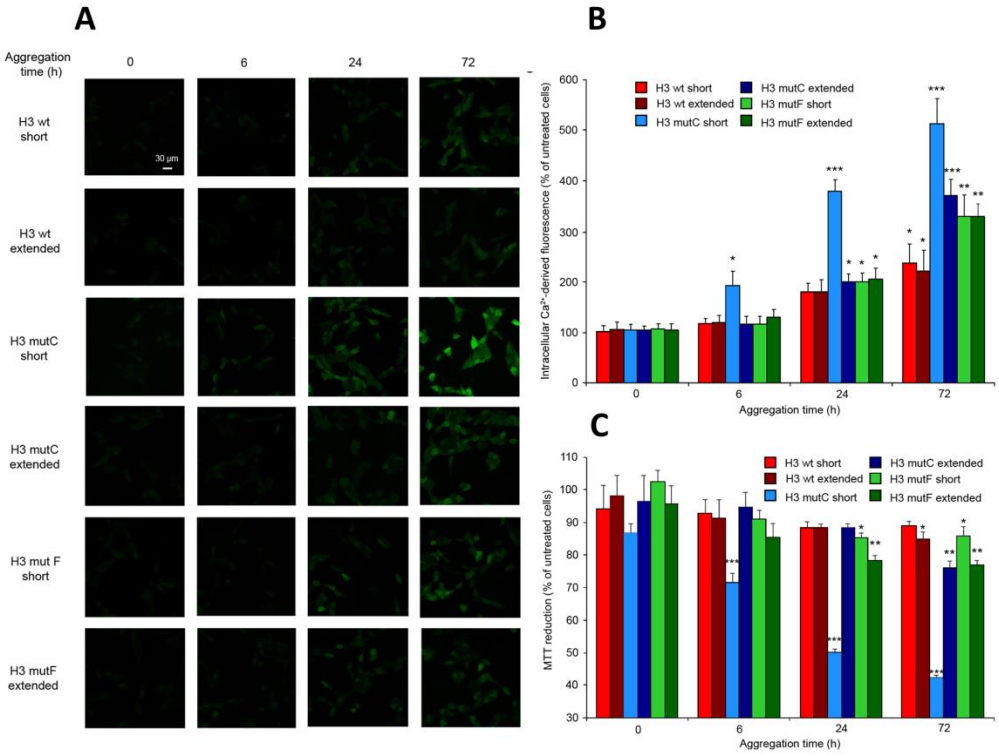

Figure 28. Cytotoxicity of several H3 peptides. **(A)** Representative confocal microscope images showing the Ca^{2+}-derived fluorescence in cells treated for 1h with indicated H3 peptides. Cells were loaded with Fluo-4 AM probe. **(B)** Intracellular Ca^{2+}-derived levels are expressed as the percentage of the value for untreated cells (taken as 100%). **(C)** MTT reduction in SH-SY5Y cells treated for 24 h with indicated peptides. The errors reported correspond to S.E.M. The *, ** and *** symbols refer to p values <0.05, <0.01 and <0.001 relative to untreated cells, respectively.

Moreover, in MTT experiments, the aggregated form of the mutC short peptide resulted cytotoxic in a time dependent manner (**Figure 28C**). The cytotoxic effect of the extended mutC sequence appeared only at longer aggregation time (72 h) (**Figure 28C**). Accordingly, cell viability was significantly decreased following treatment with the short and extended sequences of mutFaggregated for 24 and 72 h. On the contrary, the short and extended versions of the wtsequence showed a slight toxic effect only after 72 h of aggregation (**Figure 28C**).

1.1.3. $NPM1_{264-298}$: design, structural and functional characterization

In this study, with the intention to study how the connection of H2region and H3 mutA could interfere with the aggregation, we decided to synthetize the polypeptide spanning 264-298 residues of NPM1 in type A mutation ($NPM1_{264-298}$), reported **Figure29A**.

We firstly analyzed the tendency of $NPM1_{264-298}$ polypeptide to aggregate using Thioflavin T (ThT) fluorescence emission at 482 nm [170] and tyrosine (Tyr) emission at 303 nm [171]. Interestingly, as shown in **Figure 29B**, ThTfluorescence intensity displayed two distinct transitions suggesting a seeding effect of initial aggregates to reach larger oligomers [188]. The analysis of Tyr emission(**Figure 29C**) confirmed the ThT results: the progressive decrease of intensity indicated that Tyr residue was embedded in hydrophobic pockets upon the progression of fibrillization [191].

In order to study the influence of H2 region (264-277) on aggregation process of $NPM1_{264-298}$, we monitored ThT fluorescence emission through an amyloid seeding assay (ASA). In details, we performed the assay using two different equivalents (0.002 and 0.1) of $H2^{264-277}$ with r1espect to $NPM1_{264-298}$. As reported in **Figure 29B**, the addition of preformed-seeds of $H2^{264-277}$ to the reaction of aggregation of treated $NPM1_{264-298}$ polypeptide accelerates amyloid formation in a dose-dependent manner, compared with control.

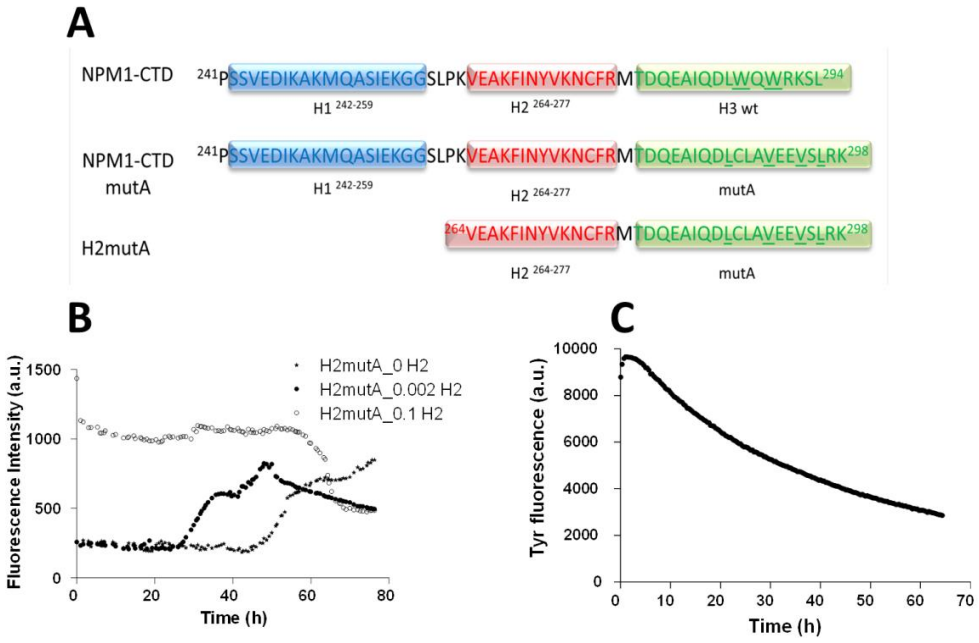

Figure 29. A) Schematic representation of native and mutated sequences of CTD of NMP1 and $NPM1_{264-298}$ peptide (underlined residues in the wt represent the NoLS, in the mutA form the acquired NES); Aggregation tendency of $NPM1_{264-298}$ polypeptide: B) ThT fluorescence assay in absence and presence of H2264-277 at different equivalents: 0, 0.002 and 0.1; C) Tyr fluorescence emission of $NPM1_{264-298}$.

The conformational properties were then evaluated performing a CD assay (**Figure30A)**. At t=0, as expected the CD profile indicates a mixed α-helix+random coil conformation due to the presence of two minima at 201 and 222 nm. The progressive decrease of Cotton effect, in four days, clearly indicated aggegation and the sligth shift of the minimum wavelengths from 201 nm to 205 nm suggested a certain conformational flexibility of the polypeptide during self-recogntion mechanism. DLS analysis, reported in **Figure 30B,** enriched the aggregation investigations. The experiment was performed over time at a peptide concentration of 1 mM. After 2 days, the $NPM1_{264-298}$ peptide showed a correct DLS profile with an apparent hydrodynamic radius centered at 220 nm.

In many amyloid systems the red edge excitation shift (REES) [192] represents a weak emission peak at 430 nm with λ_{exc} at 360-400 nm potentiated by additional fluorescence arising from charge delocalization along the backbone of the fibers in the amyloid structures [189]. Similarly, $NPM1_{264-298}$, as soluble aggregate, exhibited intrinsic fluorescence: the overlay of emission spectra at different excitation wavelengths is reported in **Figure30C**. The emission peak of $NPM1_{264-298}$ was shifted from ~420 to ~530 nm when excited in the 336 - 440 nm range and the maximum value

corresponded to 336 nm of excitation. The dependence of emission upon diverse excitation wavelengths is due to a heterogeneous size distribution of amyloid states [174, 193].

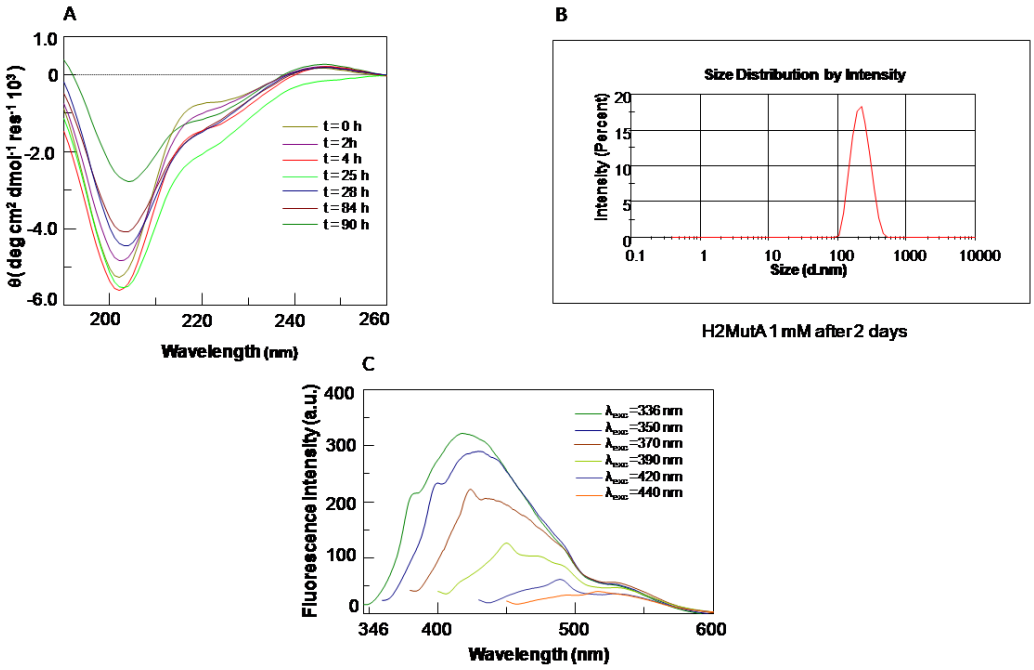

Figure 30. Conformational behaviour of NPM1mutA polypeptide: A) Overlay of CD spectra of $NPM1_{264-298}$ at different times; B) DLS profile after 2 days of aggregation of $NPM1_{264-298}$; C) Changes in the intrinsic fluorescence spectra of $NPM1_{264-298}$ at different λexc.

Label-free detection methods are also based on multiphoton excitation fluorescence (MPEF) and second harmonic generation (SHG) imaging: in these phenomena the non isotropic organisation and inherent non centro symmetry of the fibers enhance their SHG susceptibility [194]. The same sample described in **Figure 30C** was allowed to fibril for 48 h and then analyzed through MPEF: in **Figure 31A** fluorescence intensities of a representative fiber was reported as function of excitation wavelengths. The most intense signal derived from excitation at 810 nm (reported in **Figure31B**) that, since it is a two-photon excitation fluorescence, can be translated to 405 nm in single photon mode. This maximum value appeared shifted to longer wavelengths with respect to soluble aggregates and this is probably due to a further electron delocalization of amyloid nanostructures. In these conditions, the average diameter of fibers is 16.0±1.3μm.

To corroborate these data, we stained fibers with ThT and the image of related fiber is reported in **Figure31C**. The average of diameter values reported 18.7±0.9μm is in perfect agreement with that estimated on the same fiber with MPEF of **Figure31B**.

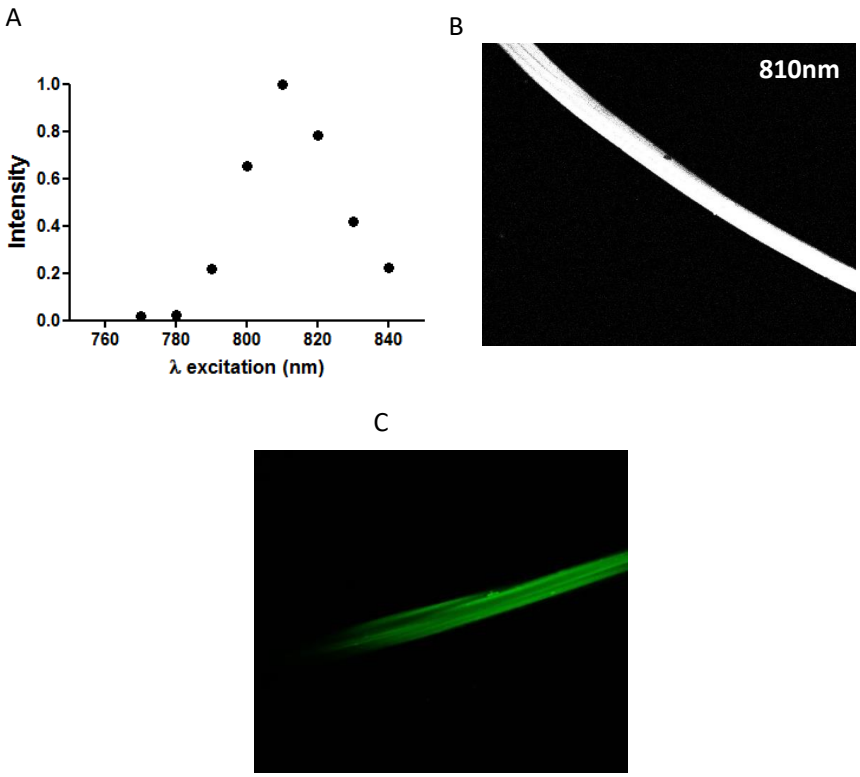

Figure 31. Structural characterization of amyloid fibers of NPM1mutA 264-298 polypeptide: A) Second harmonic generation (SHG) analysis of $NPM1_{264-298}$fibers: the fluorescence intensities of fiber are reported as function of excitation wavelengths; B) SHG image of a representative fiber at 810 nm as excitation wavelength; C) Confocal image of 50 mM ThT stained fibers after 15 hours of incubation, λexc: 440nm, λemiss: 460-600nm.

To gain deeper insights into the aggregated state of the $NPM1_{264-298}$ and in its molecular organization, Scanning Electron Microscopy (SEM) experiments were carried out. SEM micrographs are reported in **Figure 32**. Very long fibers were detected (~870μm) (**Figure 32A**): they appeared similar in length and thickness, and several of them appeared wrapped around themselves **Figure 32B**. Flat nanostructures were observable with averaged width of 13.6±1.2μm, as indicated in **Figure 32C**: in details, fibers appeared formed by the aggregation of smaller tapes, as fibers of fibers, as observed from zoom view reported in **Figure 32D**.

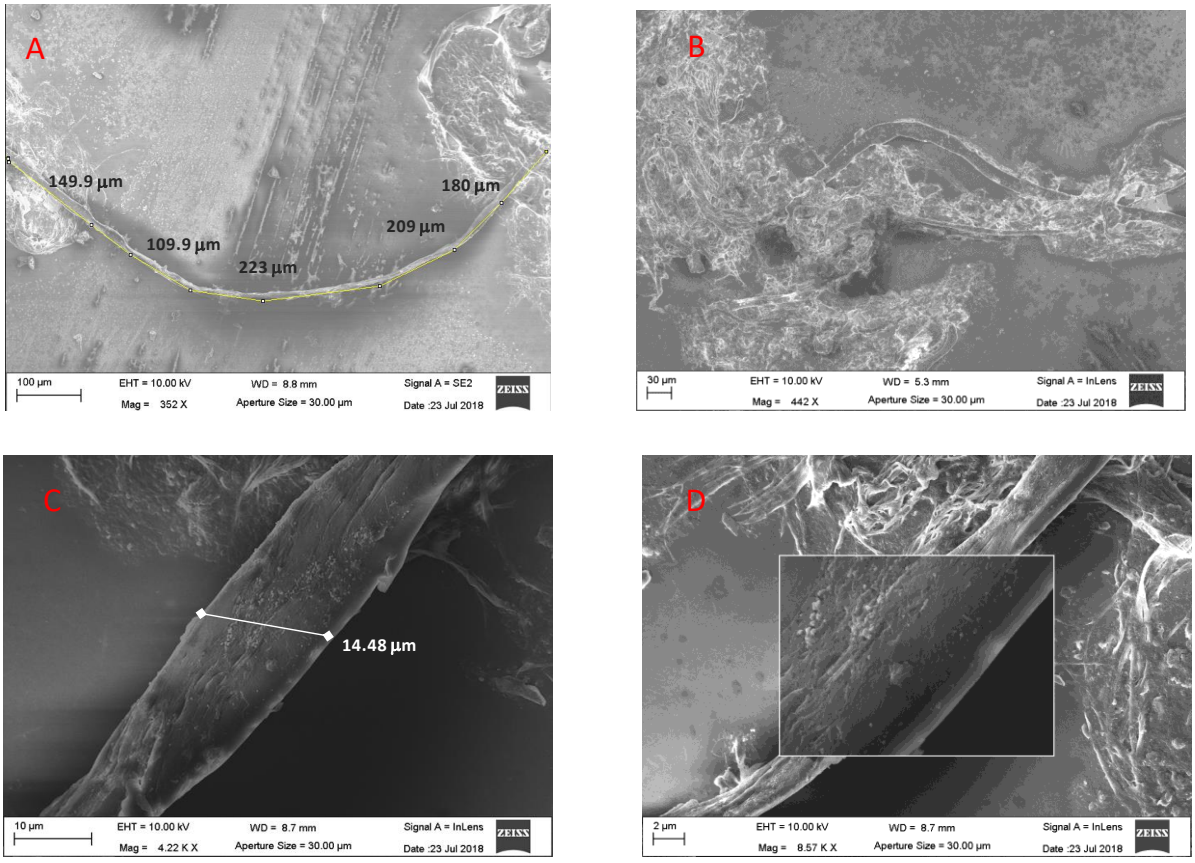

Figure 32. Scanning Electron Microscopy (SEM) images. A) Overview of the entire fiber at 352x, 100 µm; B) Fibers wrapped around themselves with measures at 442x, 30 µm; C) Details at 4.22 K x, 10 µm with highlighted diameters; D) More details at 8.57 K x, 2 µm, show fibers of fibers as observed from zoom view.

The $NPM1_{264-298}$ peptide was also investigated for its ability to impair cell viability. In detail we analyzed the effects of the aggregates formed from $NPM1_{264-298}$ on the mitochondrial status by measuring the MTT reduction assay in human SH-SY5Y neuroblastoma cells, as reported in **Figure 33**.

A sample of $NPM1_{264-298}$ at concentration of 267 µM was incubated under stirring and at 4 different times (0, 24, 32 and 70 h) added to the cells. Aggregated peptide showed the highest toxicity at 32 h, becoming less effective after 70h of incubation probably due to the conversion of the early aggregates into larger aggregates or mature fibrils, which are known to be less toxic than the first oligomeric species, in perfect agreement with kinetic profiles of aggregation.

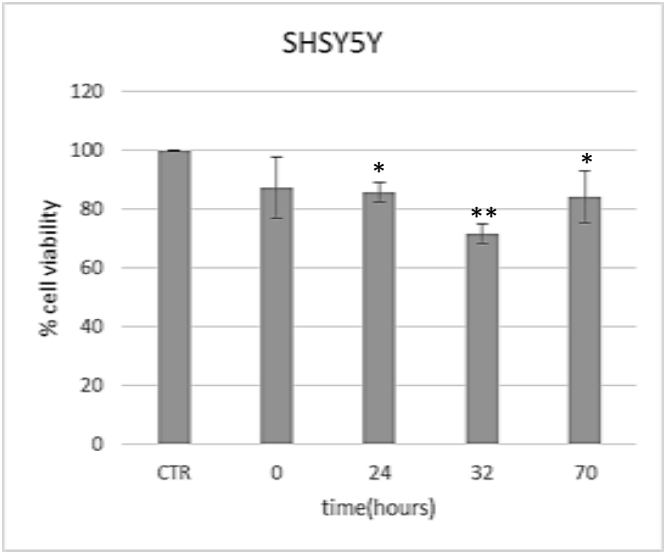

Figure 33. Cytotoxic effects of $NPM1_{264-298}$in SH-SY5Y cells: MTT assay of aggregates formed from A sample of$NPM1_{264-298}$ at concentration of 267 µM incubated under stirring and at 4 different times, 0, 24, 32 and 70 h. The * and ** symbols refer to p values <0.05 and<0.01, respectively.

1.2. Discussion

AML encompasses a heterogeneous group of diseases that has traditionally relied on morphology, cytochemistry and cytogenetic analysis for classification into various subtypes and in turn into different prognostic categories. The AML genome contains more than 20 driver recurrent mutations. The classification of AML into prognostic subgroups depending on the specific gene mutations, the so-called ''AML with gene mutations'', includes mutations in FMS-like tyrosine kinase 3 (FLT3) and nucleophosmin 1 [195]. All mutant NPM1 translation products change their nuclear localization signal and a shift in the balance of nuclear export occurs, leading to the accumulation of NPM1 in the cytoplasm [63, 196-198]. AML cells carrying NPM1 mutations always retain a certain amount of wt NPM1 in the nucleolus [54]. This is probably necessary for the survival of leukemic cells [199], since NPM1 mutations in AML are always heterozygous and knock-out mice with complete deletion of the NPM1 gene die during early embryogenesis [60]. Because NPM1 acts in the nucleolus as a hub building protein [200], the nucleolus of NPM1-mutated AML cells may be more vulnerable with respect to cells expressing only wild-type NPM1. AML cells are partially depleted of NPM1 as a consequence of both NPM1 haploinsufficiency and cytoplasmic delocalization of wt NPM1 protein as complexes with the mutants. Thus, mutation-induced changes of the levels or the oligomerization status of NPM1 may influence its capability to properly build up the nucleolus in *NPM1*- mutated AML cells. The mechanism through which cytoplasmic nucleophosmin contributes to leukemogenesis remains still unknown. Furthermore, NPM1 mutations are stable since they are detected during the whole course of the disease including relapses and thus represent a suitable target for immunotherapy.

NPM1 mutated sequences were also investigated for their immunogenic properties associated with cytoplasmatic localization and for the development of immunotherapy for the treatment of AML patients [201-203]. In my research group, previous studies evidenced the ability to aggregate in an amyloid-like manner of several regions of the C-term of NPM1.

In the present thesis, to deepen the molecular mechanisms linked to AML misfolding and to further evaluate the leukemogenic potential of AML mutations we investigated biophysical features of several protein regions. We firstly analyzed the smallest amyloidogenic stretch of the entire NPM1 sequence: encompassing region264-272. The investigated NPM1 fragment (264-272) presents Phe^{268} and Tyr^{271} that belong to the structural aromatic core that held together the helices of the bundle in the native protein structure [204] and play key roles in the aggregation of larger fragments [169], indeed

π-π interactions often demonstrated crucial for both protein and small peptides aggregation processes [205]. Spectroscopic investigations of NPM1 $_{264-272}$ peptide clearly indicate a strong tendency of this sequence to self-aggregate following a mechanism of propagation in which the native α-helical state exerts a predominant role to drive toward nanostructures and then stable β-turn fibrils [206-207].Aggregation states by ESI results, are consistent with the SEM analysis, in which the aggregation of smaller tapes with a width of ~30 nm has been observed. Considering that the distance between two β-strands is 0.48 nm, as derived by WAXS measurements, the number of assembled monomers should be approximately of 62.5. Finally, the main structural feature of amyloid fibrils in the cross-β architecture were confirmed by WAXS analyses of fibers deriving from NPM1 $_{264-272}$.

Studies on H3 mut sequences confirmed their ability to form amyloid aggregates with different kinetics and levels of oligomerization. In particular, the presence of a common stretch of seven residues at the N-terminal part delays self-assembly suggesting a protective role of the protein architecture toward the aggregation. In particular, two sequences, mutC and mutF, exhibited conformational transitions even if with very different times of aggregation. Furthermore, they demonstrated diverse cytotoxic abilities in human neuroblastoma cells.

To gain insights in cooperativity effects of hot spots of aggregation in mutA Cterminal domain we investigated the polypeptide deriving from the connection of H2 and H3 in the type A mutated variant, NPM1$_{264-298}$. Spectroscopic investigations of 264-298 NPMc+ polypeptide clearly indicate self-aggregation following a multiple mechanism of propagation and a seeding effect of intermediate aggregates Amyloid seeding assay experiments carried out employing H2 as seed, clearly indicated the abrogation of the lag phase of aggregation [178] confirming a cooperative effects between distinct protein regions in aggregating process. The self-assembly mechanism of this Cterm mutA region was confirmed by DLS analysis and by the intrinsic fluorescence emission properties of soluble aggregates. Subsequently these features were exploited in multiphoton excitation fluorescence (MPEF)- second harmonic generation (SHG) structural analyses of amyloid fibers. Noticeably derived aggregates resulted toxic in MTT assay suggesting the ability to self-degrade by mutA protein with respect to wt NPM1. In conclusion, studies herein presented represent an important piece of the puzzle to elucidate the interactions among NPM1 domains within homo- and hetero-pentameric structures both in its native and AML mutated state.

2. SOCS1 and SOCS3 mimetics: potential therapeutic agents in atherosclerosis and cancer

2.1. Results

2.1.1. Mimetics of SOCS3

2.1.1.1. 1st generation sequences: KIRESS peptide SOCS3 22-45

As previously reported, Babon and co-workers, in 2013, reported the X-ray structure of the ternary complex between mouse SOCS3, JAK2 kinase domain and gp130 phosphotyrosine-peptide, highlighting the inhibition mechanism of SOCS3 for JAK2 (**Figure34A**)[100, 208]. Gp130 domain was used in the crystallization experiment to improve SOCS3 aqueous solubility, but it does not interfere with JAK inhibition. As shown, SOCS3 can interact with JAK2 and gp130 simultaneously via two adjacent binding interfaces[209]. The X-ray structure of the ternary complex, solved at 3.9 Å resolution, provides details on the contact surface between SOCS3 and JAK2 and on the interactions that take place in the formation of the complex (**Figure34B**).

The SOCS3/JAK2 contact surface is approximately of 980 Å2. At the interface between the two proteins, hydrophobic-hydrophobic interactions dominate. JAK2 residues that are mainly involved in the recognition of SOCS3 are Gly1071, Gln1072, Met1073, which compose the so-called GQM motif responsible for recognition of JAK1, JAK2 and TYK2[209] and residues of helix G (Met1073- Ser1084)[210]. In particular, residues belonging to the GQM motif interact mainly with residues Leu22, Lys23, Thr24, which belong to KIR, and with residues Ser73, Ser74, Asp75, Gln76, Arg77, His78, Phe79 and Phe80 (BC loop) of SH2 domain of SOCS3, whereas residues Phe1076, Ile1079 and Glu1080 of the helix G of JAK2 pack against a hydrophobic surface of SOCS3 encompassing residues belonging to KIR (Thr24, Phe25, Tyr31), and to ESS (Val34, Val35 and Val38). The same hot spots were previously indicated by mutagenesis investigations on Leu22, Phe25, Glu30, Val34, Leu41[211]; while structural studies in solution (NMR) indicated ESS as the most perturbed region in the presence of gp130 peptide[212]. Other contacts involve some residues in a “hinge” region between ESS and helix A (HA) of the SH2 domain of SOCS3. In particular, residues Tyr47, Ser49 and Ala50 lie close to Asp1068, Lys1069 and Gln1070 (< 3.7 Å from Ala50), Met1073 (3.8 Å from Ty47) and His1077 (4.1 Å from Ser49) of JAK2. JAK2 Gln1070 is also close to Thr52 which is the first residue of HA of SOCS3 (distance <3.4 Å).

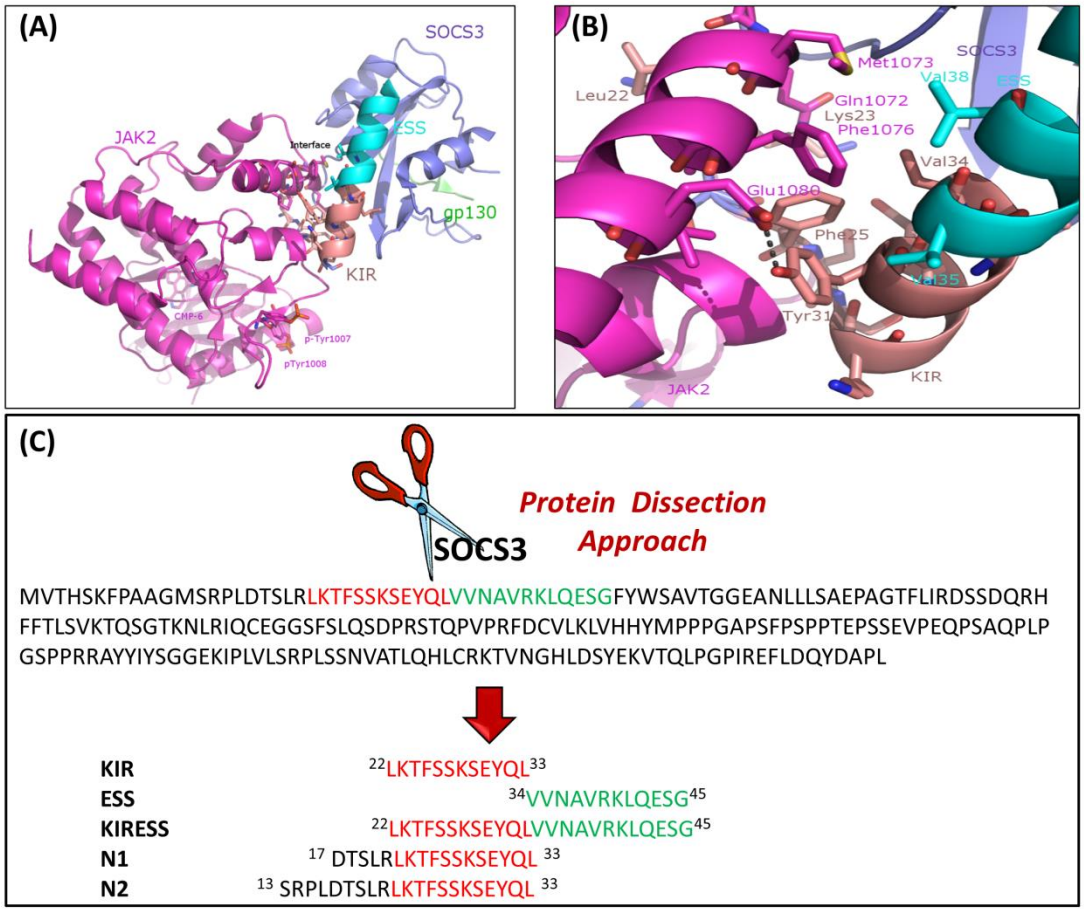

Figure 34. Design of SOCS3 peptides: **A)** Structural model of the ternary complex between SOC3, JAK2 and gp130. In this figure, JAK2 is colored in purple, SOCS3 in violet, gp130 in green. KIR and ESS regions of SOCS3 are in light brown and cyan, respectively. Positions of pTyr1007 and 1008 and of a JAK2 inhibitor, CMP-6, are also highlighted. **B)** Details of the hydrophobic JAK2-SOCS3 interface. A selection of important residues is shown and residues are labelled. The hydrogen bonds between the side chain atoms of Glu1080 and Tyr31 and between the N atom of the side chain of Gln1072 and the main chain oxygen of Lys23 are shown as dotted lines. **C)** Schematic derivatization of SOC3 peptides analyzed in the work.

On the basis of this structural analysis,[209] and considering the regions endowed with regular secondary structures, a protein dissection approach was used to identify the minimum active sequence of SOCS3 needed to JAK2 recognition (**Figure34C**). In particular, we designed peptides LKTFSSKSEYQL (KIR) and EYQLVVNAVRKLQESG (ESS) and a polypeptide containing both KIR and ESS (KIRESS) (**Table 6**). Furthermore, we synthetized other two additional peptides, named N1 and N2, in which the sequences DTSLR and SRPLDTSLR were added to the N-terminus of KIR. These residues are not observed in the crystal structure of the ternary complex, but were indicated to influence STAT3 phosphorylation in mutational studies[211].

Table 6: ka, kd and KD (in mM) values of the affinity of SOCS3 peptides toward JAK2.

Name	Sequence	ka(1/Ms)	kd *10 $^{-3}$ (1/s)	K_D(μM)
KIR	^{22}LKTFSSKSEYQL^{33}	6.7	1.36*10^{-5}	2.03
ESS	^{34}VVNAVRKLQESG^{45}			>>1000
KIRESS	^{22}LKTFSSKSEYQLVVNAVRKLQESG^{45}	226	3.89*10^{-5}	0,172
E30A KIRESS	^{22}LKTFSSKS**A**YQLVVNAVRKLQESG^{45}		No binding	
N1	^{17}DTSLRLKTFSSKSEYQL^{33}	241	73.1	303
N2	^{13}SRPLDTSLRLKTFSSKSEYQL^{33}	2.8	4.48*10^{-3}	1660
NC	AAARAAARAAARAAARAAARAAAA		No binding	

CD spectra of SOCS3 peptides were recorded in the far UV region in 10 mM phosphate buffer and in the presence of a structuring agent like TFE [212-213] (**Figure 35**). CD analysis suggests that the peptides, in aqueous solution, have a secondary structure content that partially reflects that they adopt in the native protein. In detail, the KIR and ESS (**Figure 35A** and**35B**respectively) sequences have similar CD spectra with minima at wavelength ≤ 200 nm, typical of unstructured peptides, confirming previous studies [212, 214].

The conjunction of these two regions in the KIRESS peptide causes an enhancement of the helical content, evidenced by the presence of the minimum at 222 nm (**Figure 35C**)[212, 214]. These features were further confirmed by a TFE titration, where KIRESS reached its maximum helical content at about 30% TFE. In previous NMR investigations the 15-residue peptide encompassing ESS and C-terminal half of KIR (residues Glu30-Ser44) was identified as a single helix [212]. On the other hand, in the unique available computationally-derived model of SOCS1, KIR and ESS region form two orthogonal helices [215]: this is probably due to difference in sequence in the ESS region between SOCS3 and SOCS1. These features along with SPR investigations (see below) suggest an important role exerted by secondary structure in different mechanisms of recognition of JAK2 by SOCS1 and SOCS3. The characterization of the conformational features of the sequence SRPLDTSLR in the N-terminally extended peptides of KIR, i.e. N1 and N2, confirms the tendency of this region to be

disordered [216], even in a structuring environment. Indeed, both sequences need high TFE concentrations, up to 70%, to reach partially ordered conformations, as shown in **Figures 35D** and **E.**

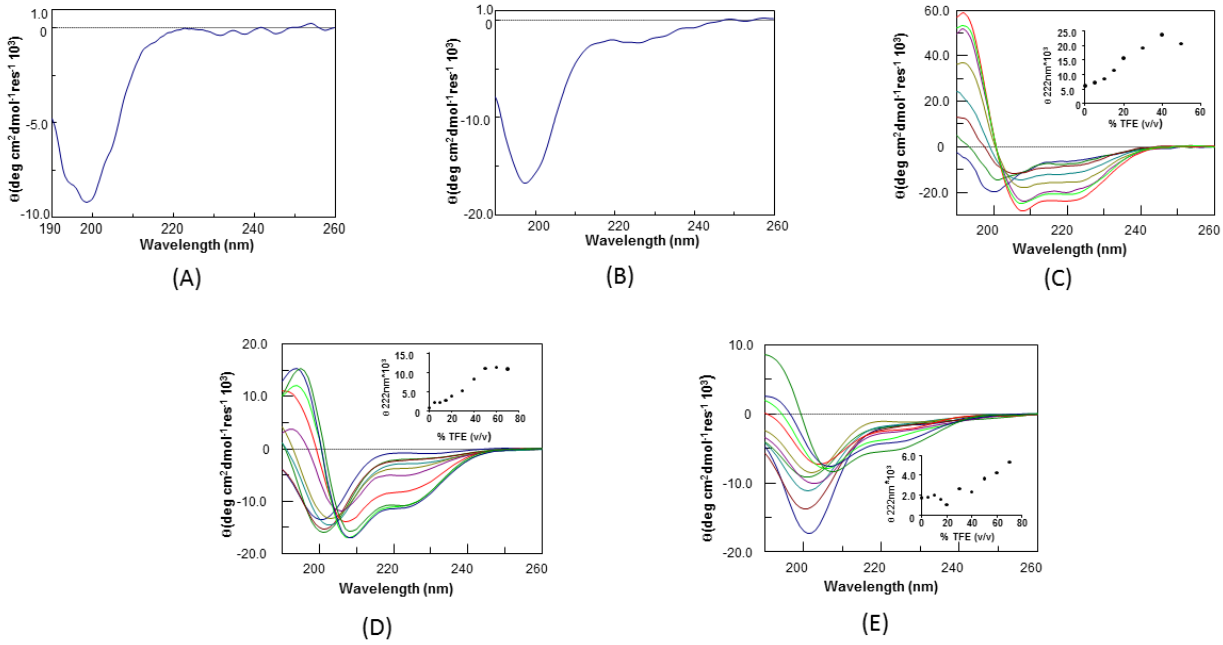

Figure 35.Conformational analysis of SOCS3 derived peptides through CD spectroscopy: CD spectra of (A) KIR, (B) ESS; at increasing concentrations of TFE (B) KIRESS (0–50%), (D) N1, and (E) N2 (0–70%).Overlay of spectra recorded at different concentrations of TFE are shown in the inset.

Subsequently, to evaluate the ability of SOCS3-derived peptides to bind to JAK2, a sandwich immobilization of the biotinylated catalytic domain of the kinase was carried out on a SA-coated chip.

The overlays of sensorgrams reporting the binding of SOCS3 peptides to JAK2 are shown in **Figure 36**. Inspection of the sensorgrams reveals that the RU signal intensity increases as a function of peptide concentrations in a dose-response way. In most cases, kinetic parameters can be estimated; dissociation constants (K_D) evaluated with the 1:1 Langmuir with drift of baseline fitting are reported in **Table 6**. K_D values are quite different, suggesting the existence of several hot spots at the interface between SOCS3 and JAK2, at least for the investigated SOCS3 regions. Notably, some sensorgrams are rather noisy (**Figure 36**), probably due to the insolubility of the peptides at high concentration or at JAK2 interface.

In detail, N1, N2 and KIR show a micromolar dissociation constant, differently from what has been observed for the KIR peptide of SOCS1 [139, 217] , and in line with what observed for functional chimera

proteins. ESS also reveals poor affinity toward JAK2, since under the investigated experimental conditions a row estimation of the K_D indicates a value >>1mM. A synergic effect was observed in the affinity shown by KIRESS, which has a higher affinity toward JAK2 when compared to the separated peptides, with a K_D in the very low micromolar range. This higher affinity appears mainly due to a faster association kinetic (**Table 6**). The N-terminal extension of KIR sequence in N1 and N2 does not improve the affinity of the SOCS3 peptide for JAK2. Rather, it negatively interferes with KIR recognition abilities, especially in the association phase (**Table 6**). As expected an unrelated peptide, with the same length of KIRESS, named NC (**Table 6**), was unable to recognize JAK2 (data not shown).

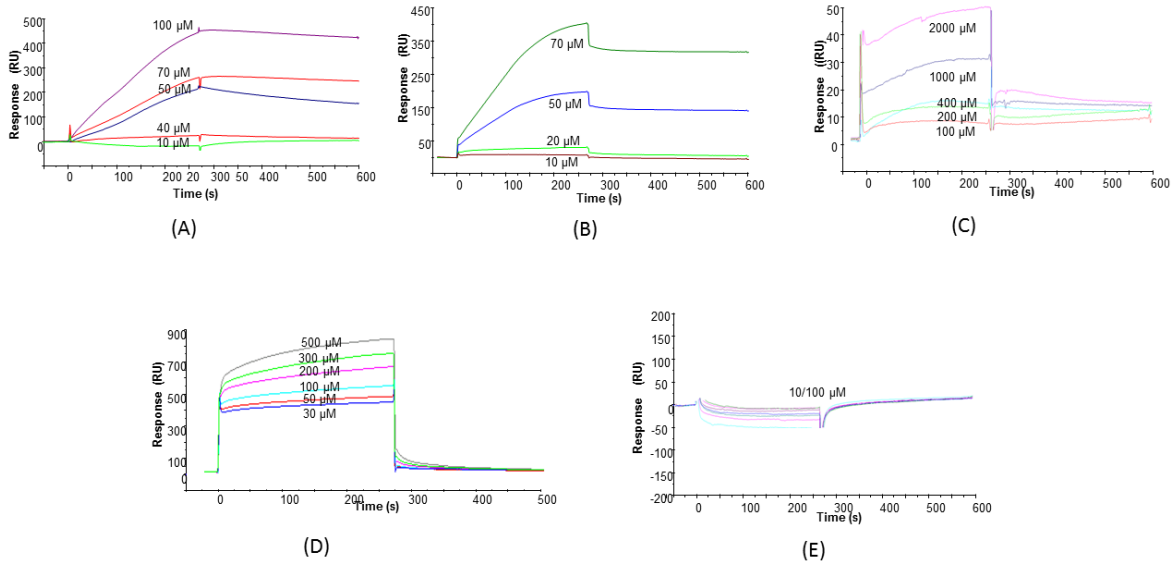

Figure 36.SPR assays for SOCS3 derived peptides toward JAK2: overlay of sensorgrams related to the binding of (A) KIRESS (B) KIR (C) ESS, (D) N2 and (E) E30A KIRESS peptides on biot-JAK2 immobilized on a SA-chip. Peptide concentrations are also indicated. Kinetic parameters obtained through a 1:1 Langmuir binding model with drift of baseline allowed to estimate dissociations constants reported in **Table 6**.

Considering SPR results, we have chosen KIRESS peptide for further *in vivo* investigations. In particular, in order to determine its cellular delivery, cells at medium density were treated with FITC-KIRESS peptide for 48-72 hours. Efficient delivery of the peptides *in vitro* was determined by fluorescent microscopy, which showed majority of the cells with FITC emission (**Figure 37A**). We also quantitated the percent rate of KIRESS peptide uptake by flow cytometry using the FITC and showed that more than 905 of cells showed FITC positivity (**Figure 37B**). To demonstrate the efficiency of delivery in mice, control or the 4T1 tumor-bearing BALB/c mice were treated with one dose of FITC-KIRESS peptide and animals were sacrificed after 16-18 hours and the peptide uptake was analyzed in

bone marrow, spleen and tumors by flow cytometry. Tumor-bearing animals (red line) has demonstrated much more efficient uptake of the KIRESS peptide in primary tumor as well as bone marrow and spleen compared to non-tumor bearing mice (**Figure 37C**). Although the data was surprising, it was reproducible and thus we concluded that more efficient peptide uptake in organs provides an easy access for peptides to disseminated tumor cells in these organs. Furthermore, our data are supported by previous reports suggesting that metastatic cancer patients may have higher vascularity index and increased blood flow [218-219]. Therefore, mice bearing aggressive/metastatic 4T1 tumors may have a higher vascularity index and increased blood flow which may have resulted in much efficient peptide uptake compared to non-tumor bearing mice.

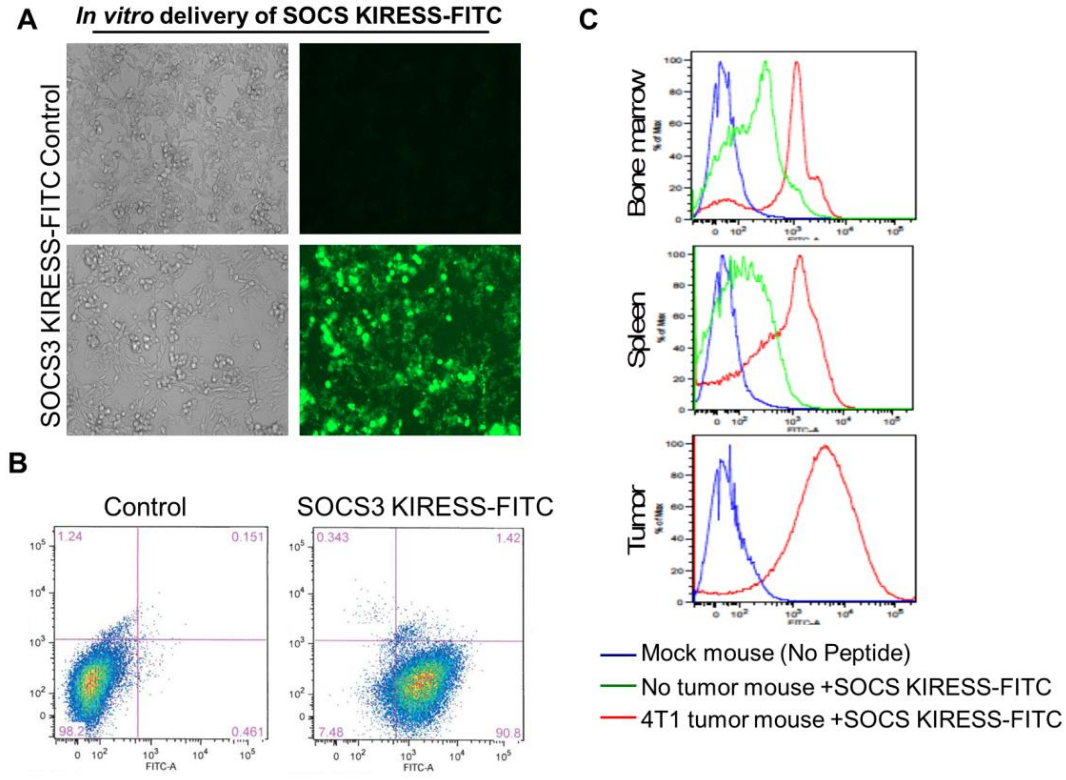

Figure 37. *In vitro* and *in vivo* delivery of SOCS3 KIRESS peptide. (A,B) FITC conjugated SOC3 KIRESS peptide (at 10 mM dose) was efficiently delivered into the cells *in vitro* as demonstrated by fluorescent microscopy and flow cytometry. (C) Control or the 4T1 tumor bearing BALB/c mice were treated with one dose of SOCS KIRESS-FITC peptide (10 mg/kg) and animals were sacrificed after 16 hr and KIRESS-FITC peptide uptake were analyzed in bone marrow, spleen and tumors by flow cytometry. Tumor bearing animal (red line) has demonstrated very efficient uptake of the KIRESS peptide in bone marrow, spleen and tumor compared to mouse without tumor (green line) and control animal (blue line) without peptide injection. Results are presented as mean±SD (n=3).

We next investigated the effects of KIRESS peptide on tumor growth *in vivo* in human breast tumor xenografts. MDA-MB231-Luci tumor bearing NOD-SCID animals after 2 weeks post-implantation were treated with either control and KIRESS peptide for the duration of 3 weeks. During the course of treatment, MDA-MB-231-luci tumors were monitored by optical imaging. KIRESS peptide treated mice showed reduced tumor growth as shown by the reduced luci intensity after 3 weeks (**Figure 38A, B**) and eliminated pulmonary metastasis as demonstrated by optical imaging in live mice and ex-vivo images and histological examination of lungs (**Figure 38A, C, D**). In order to determine target specificity of KIRESS peptide's action, we assessed SOCS3/pStat3/NF-kB pathway by western blotting experiments. KIRESS peptide significantly reduced the pStat3 and NF-kB (p65) phosphorylation (**Figure 38E**) as well as number of inflammatory cytokines including IL6, leptin, RANTES (**Figure 38F**) acting as an effective mimetic of the whole SOCS3 protein. Furthermore, KIRESS peptide efficiently induced the accumulation of SOCS3 protein upon inhibition of pStat3/NF-kB pathway (**Figure 38E**). This is also consistent with our previous report that SOCS3 degradation is dependent on the IL6/pStat3/NF-kB pathway [220].

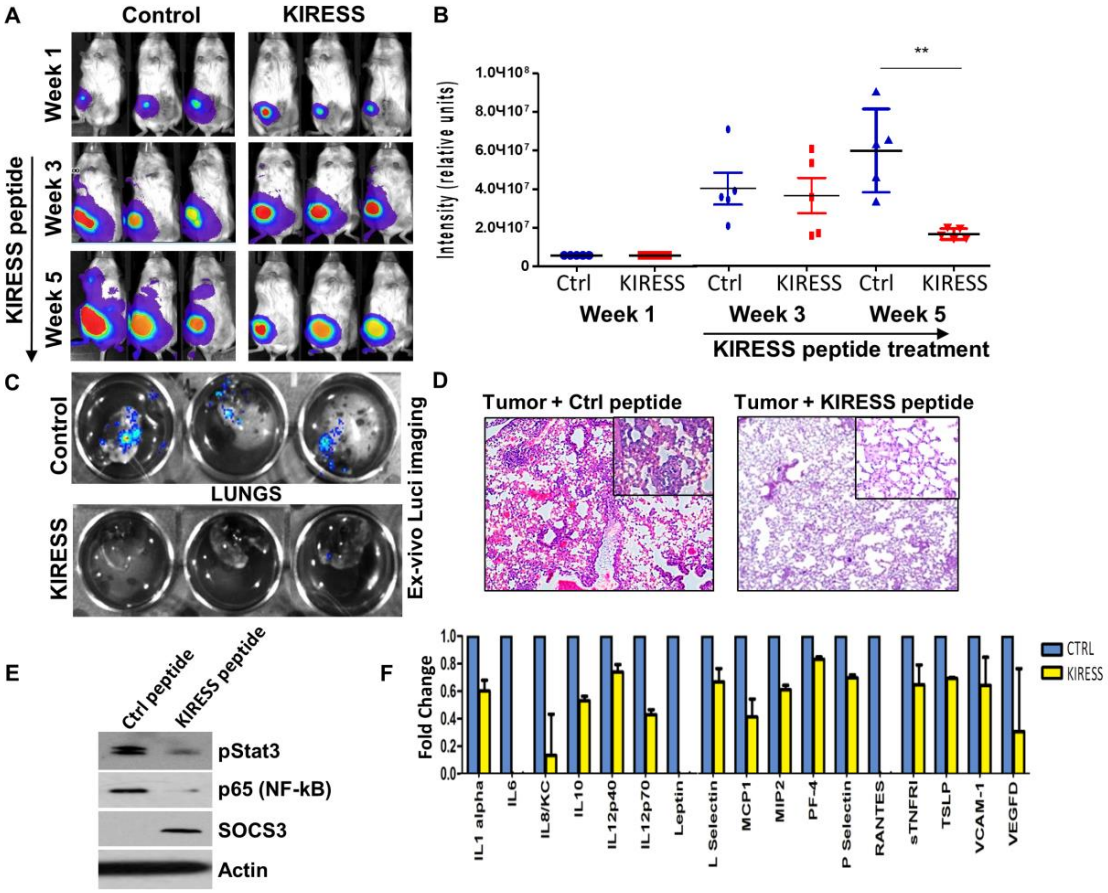

Figure 38. Activity of KIRESS peptide on human breast tumor xenografts. (A, B) MDA-MB231-Luci tumor bearing NOD-SCID animals were treated (starting at Week 3 postimplantation) with either control peptide or KIRESS peptide (10 mg/kg, every other day) via IP injection. KIRESS peptide treated mice showed a significant suppression of primary tumors. (C, D) Elimination of lung metastasis in KIRESS peptide treated mice is shown by ex-vivo luciferase imaging of lungs and histology sections. Insets are 403 magnification of selected areas of lungs. (E) Tumors from KIRESS peptide treated animals showed suppression of pStat3/NF-kB pathway. In addition, this was resulted in upregulation of SOCS3. (F) Luminex analyses of serum cytokines from control and KIRESS peptide treated mice revealed a significant suppression of circulating levels of cytokines that are tested. Results are presented as mean±SD. (n=5). **p>0.005, unpaired t test.

Due to the crucial role that SOCS3 plays in immune responses to infection or other pathological conditions such as cancer, we examined the toxicity associated to the presence of KIRESS peptide. Histopathological examination of intestine, liver and kidney of treated animals clearly indicates no observable toxicities (**Figure 39A**) and similarities of gross animal weight among mice treated with the KIRESS, control peptide or mock (**Figure 39B**) confirmed the lack of toxicity of the active SOCS3 derived peptide.

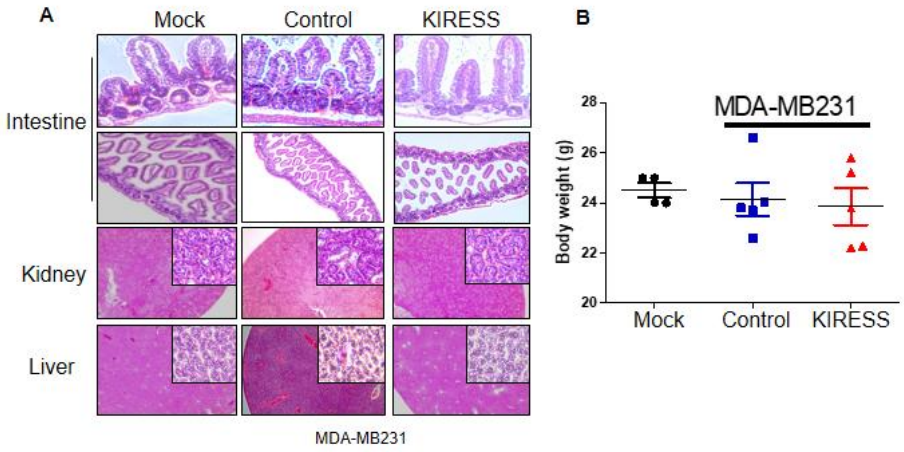

Figure39. Histopathological examination of organs from SOCS3 KIRESS peptide treated mice. (A) Intestine, kidney and liver from control (mock) or MDA-MB-231-Luci tumor-bearing NOD/SCID mice that were either treated with control or KIRESS peptide for 3 weeks show no pathological toxicity in these organs. Insets are the 403 magnification of selected areas in respective organs. (B) Body weight of control and KIRESS peptide treated animals were not significantly different. Results are presented as mean±SD (n=5).

2.1.1.2. 2nd generation of mimetics: KIRCONG chim$_{25\text{-}33/46\text{-}52}$

A deeper insight into the crystal structure of SOCS3/JAK2/gp130 allows to argue that other contacts involving some residues in a "hinge" region between ESS and helix A (HA) of the SOCS3-SH2 domain appeared crucial for the formation of the ternary complex. In particular, residues Tyr^{47}, Ser^{49} and Ala^{50} of SOCS3 resulted located close to Asp^{1068}, Lys^{1069}, Met ^{1073} (3.8 Å from Tyr^{47}), His^{1077} (4.1 Å from Ser^{49}) and Gln^{1070} (< 3.7 Å from Ala^{50} and <3.4 Å from Thr^{52} which is the first residue of HA of SOCS3) of JAK2. Interestingly, the region spanning 46-52 residues, here named CONG, bears three adjacent aromatic amino acids ^{46}FYW^{48} out of seven residues. To speculate a potential contribution of this region on the ability of SOCS3 to recognize JAK2 we designed several new chimeric peptides: ESSCONG (34-52) connecting contiguous ESS (34-45) and CONG(46-52) fragments, the other two sequences contain a shorter version of KIR sequence (named restricted KIR, deleted of three residues at the N-termini) in restKIRESSCONG (spanning 25-52 residues) and a chimeric linear peptide named KIRCONG chim including two not contiguous fragments restKIR (25-33) and CONG (46-52) connected by β-Alanines as spacers (**Table 7**).

Table 7. Sequences and names of sequences investigated in this study.

Name	Sequence	pI	MW
KIRESS	^{22}LKTFSSKSEYQLVVNAVRKLQESG^{45}	10.52	2753
ESSCONG	^{34}VVNAVRKLQESGFYWSAVT^{52}	10.37	2195
RestKIRESSCONG	^{25}FSSKSEYQLVVNAVRKLQESGFYWSAVT^{52}	9.86	3265
KIRCONG chim	KβAla^{25}FSSKSEYQL^{33}βAlaβAla^{46}FYWSAVT^{52}	9.86	2325
NC	AAARAAARAAARAAARAAARAAAA	14	2148

To evaluate the ability of new derived SOCS3 peptides to recognize JAK2 catalytic domain we decided to perform a MST experiments (**Figure 40,** upper panels). As shown, signals exhibit a dose-response curve for all three peptides but for ESSCONG signal variation was not meaningful and for restKIRESSCONG did not reach saturation. The fitting of experimental data for KIRCONG chim

provided K_D value of 11±3 µM (**Figure 40 C**) that is comparable with that reported for KIRESS previously[221]

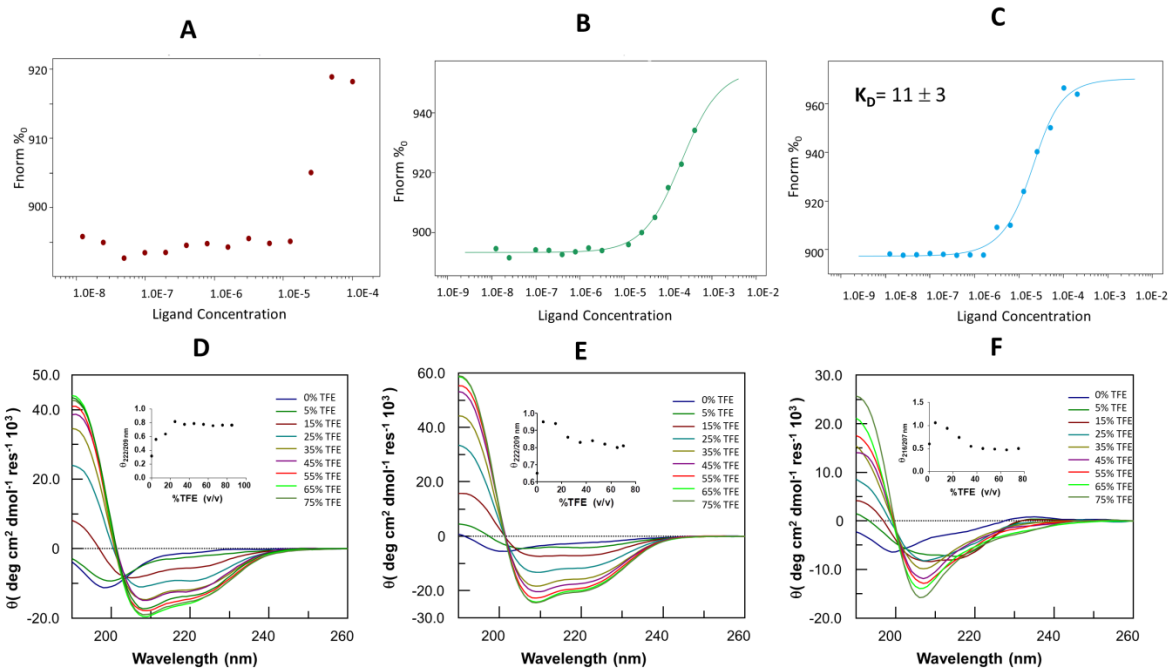

Figure 40. Upper panel: binding isotherms for MST signals versus peptide concentrations. Lower panel: Overlay of CD spectra in TFE/H20 0-75% v/v; (A, D) ESSCONG, (B, E)restKIRESSCONG, (C, F) KIRCONG chim.

Conformational analysis of SOCS3 was performed through CD and NMR. Particularly, CD spectra were recorded in the far UV region at 100 µM in10 mM phosphate buffer, pH 7 and in the presence of structuring agents like TFE (2,2,2-Trifluoroethanol) [222-223]. Spectra in phosphate buffer (**Figure 40** lower panels) present one minimum around 200 nm indicating a prevalent random content even if the presence of a shoulder at ~215 nm suggests a small contribution of helical conformations and, in the case of KIRCONG chim, a positive slight band at ~235 nm suggests a direct involvement of aromatic residues in the conformational features of the sequence [224]. To evaluate the effects of the addition of TFE to the conformational features of designed sequences we also followed the Θ_{ratio} value at increasing concentration of the co-solvent, reported as insets of **Figure 40 D** and **F**. For ESSCONG and restKIRESSCONG we evaluated the ratio between ellipticity at 222 and 209 nm and for KIRCONG chim at 216 and 207nm, respectively. The presence of TFE for all three sequences allows to reach more ordered and helical concentrations, as expected. In detail, for restKIRESSCONG and KIRCONG chim the lower TFE concentration, 5%, tends to partially induce coiled coil conformations, since the maximum value of Θ_{ratio} is observable (~1 for KIRCONG chim and 0.95 for restKIRESSCONG (Figure 1 F-E, respectively). However the addition of higher amounts of TFE stabilizes single helices,

indeed Θ_{ratio} values decrease till 20% and then remain constant. For ESSCONG the Θ_{ratio} profile increases exclusively till 20%, when, similarly to other sequences, reaches a constant value of ~0.8 (**Figure 40 D**).

To get further structural insights of the most potent ligand, KIRCONG chim peptide, NMR studies were carried out in H_2O and H_2O/TFE mixtures (15% and 40% v/v) [225].

Initial studies were performed in H_2O and revealed a flexible conformation lacking regular secondary structure elements. Comparison of 2D [^{1}H, ^{1}H] TOCSY[226] and 2D [^{1}H, ^{1}H] ROESY[151] spectra (**Figure 41A**) allowed to get almost complete proton resonance assignments[227]. The ROE pattern (**Figure 42B**, blue panel) was dominated by strong $H\alpha_i$-H_{Ni+1} peaks in between sequential residues (i and i+1) which are canonical of extended and random coil species[227]. A complete structure calculation further stressed out the absence of an ordered conformation for the peptide in water but the coexistence of multiple conformations (**Figures 41C**,**42A**); in the C-terminal peptide region, encompassing residues Tyr[15]-Ala[18], a tendency to form a bend is observed (**Figure 41C**).

A similar investigation carried out at 15% TFE demonstrated only a slight decrease of the conformational freedom of the peptide. Proton resonance assignments were obtained from combined analysis of TOCSY[226] and NOESY[228] spectra (**Figure 41B**). A complete 3D structure calculation indicates that the NMR conformers remain largely disordered (**Figure 41D**). Indeed the NOESY spectrum still contains mostly strong sequential contacts characteristic of a random coil status (**Figure 42B**, red panel)[227], although, a few NOE correlations of the type HN_i-HN_{i+2} point out the beginning of a certain helical conformation even if distorted (**Figure 42B**, red panel) [227]. Coherently the inspection of the NMR calculated conformers with the software MOLMOL[229] reveals the presence of a 3.10 helix at the C-terminus between residues Tyr[15]-Ser[17] in 4 over 20 structures (**Figures 42A** and **41D**).

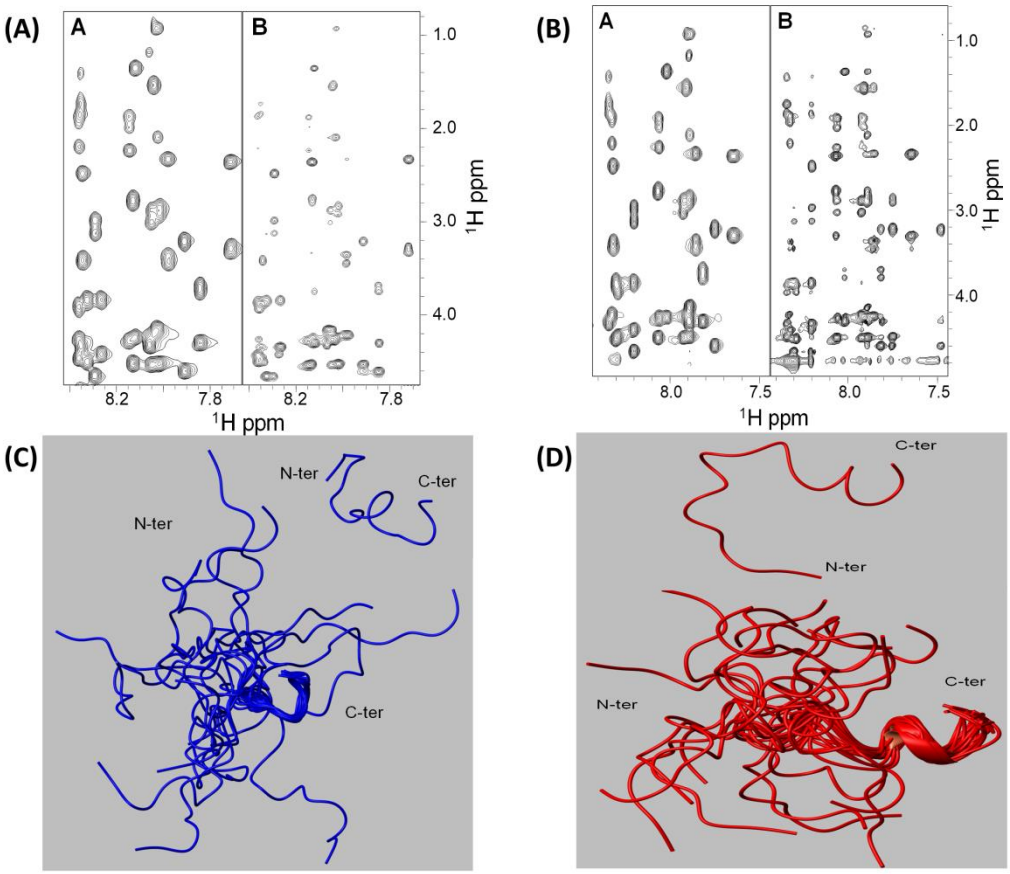

Figure 41. A) 2D [1H-1H] TOCSY (A) and ROESY 250 (B) spectra of KIRCONG chim peptide in H2O. The figure shows spectral regions containing HN/aliphatic protons correlations.**B)**2D [^{1}H-^{1}H] TOCSY (A) and NOESY 300 (B) spectra of KIRCONG chim peptide in H_2O/TFE (85/15, v/v). The regions of the spectra containing H_N/Hα and side chains correlations are shown.**C)** NMR structure of KIRCONG chim peptide calculated in H_2O: the best 20 conformers are superimposed on the backbone atoms of residues 14-20 (RMSD=1.11 Å). The first conformer of the NMR ensemble is also shown in the upper right corner. Structure calculations included 77 upper distance limits (38 intraresidue, 36 short-range, and 3 medium-range) and 91 angular constraints. **D)** NMR structure of KIRCONG chim peptide in H_2O/TFE (85/15, v/v): the best 20 conformers are superimposed on the backbone N,C,O,CA atoms of residues from 10 to 20 and the CB atoms of the b-Ala residues 12 and 13 (RMSD=1.93 Å). The first conformer of the NMR ensemble is shown in the upper panel. The NMR structure was calculated from 121 upper distance limits (60 intraresidue, 58 short-range, and 3 medium-range) and 79 angle constraints.

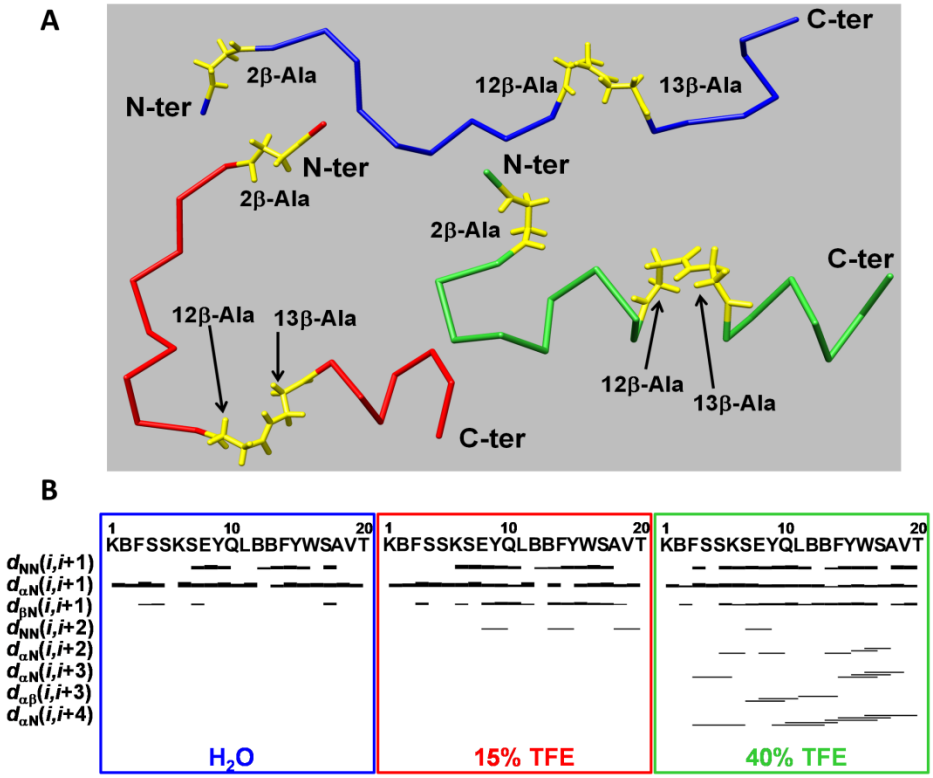

Figure 42.A) First conformers of KIRCONG chim peptide NMR ensembles in H_2O (blue), H_2O/TFE (85/15, v/v, red), and H_2O/TFE (60/40, v/v, green). The structures are reported in the Cα trace mode with all backbone and side chains atoms of the β-alanines shown and colored yellow.**B)** ROE pattern in H_2O (enclosed in the blue square) obtained from analysis of the ROESY 250 spectrum of the KIRCONG chim peptide; NOE patterns of KIRCONG chim obtained from analyses of NOESY 300 spectra acquired in 15% TFE and 40% TFE (highlighted within red and green squares, respectively); "dxy(i,i+z)" denotes a cross-peak between "x" and "y" protons in residues "i" and "i+z", respectively; the thickness of the lines is proportional to the distance: shorter distances are represented by thicker bars. The amino acid sequence is shown on top with the one letter code; B indicates the β-Ala residue.

By increasing TFE from 15% to 40%, NMR spectra, in agreement with CD ones, clearly indicate an increase of order. The NOE pattern (**Figure 42B**, green panel) shows many inter-residue correlations indicative of α and 3.10 helices including $H\alpha_i$-HN_{i+2}, $H\alpha_i$-H_{Ni+3}, $H\alpha_i$-$H\alpha_{i+3}$ and $H\alpha_i$-$H\alpha_{i+4}$[227] (**Figure 42B**, green panel). The analysis with MOLMOL[229] of the structure, identifies in most conformers an α-helix encompassing the two β-Ala residues 12 and 13, within the segment Gln^{10}-Ser^{17} and extending in a few members of the NMR structure bundle from Gln^{8}/Tyr^{9} till Val^{19} while, the N-terminal segment lacks canonical secondary structure elements (**Figures 43 B-C** and **42B**). Nevertheless, the presence of two consecutive β-Alanines is likely perturbing the regular α-

helical organization as not all the backbone CO_i-NH_{i+4} H-bonds required in a stable α-helical organization can be detected in the NMR conformers.

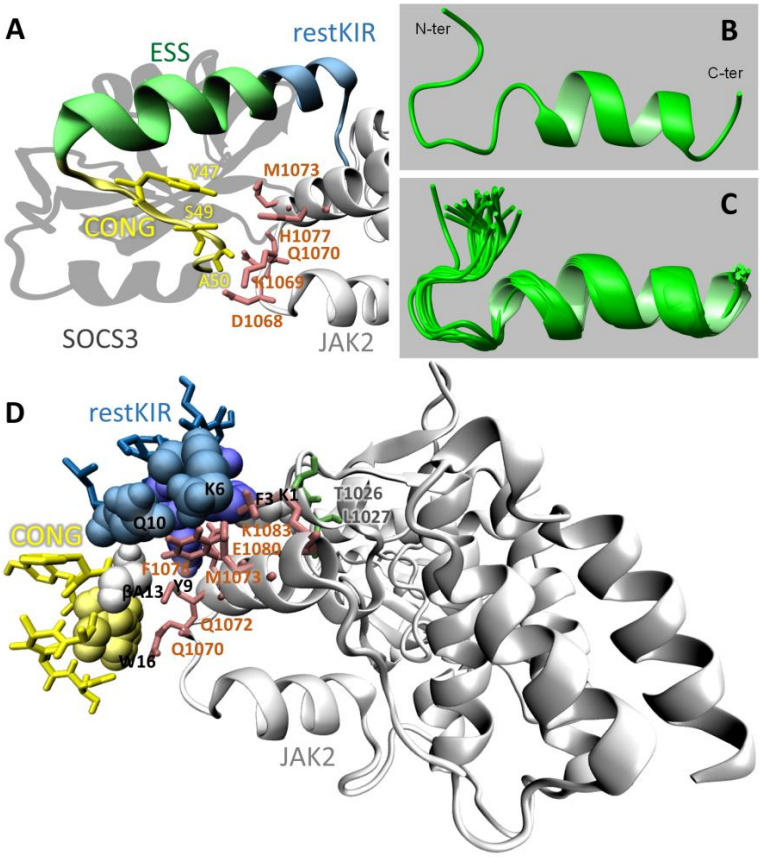

Figure 43. Structural features of KIRCONG fragment in complex with JAK2. **(A)** SOCS3/JAK2 (PDB: 4GL9 41, chains A and E) where the fragment restKIRESSCONG and residues described in the text are highlighted; (B, C) NMR structure of the KIRCONG chim peptide calculated in H2O/TFE (60/40, v/v). **(B)** Thefirst conformer of the NMR ensemble and **(C)** the best 20 conformers superimposed on the N, C, O, CA backbone atoms of residues 3-20 and CB atoms of residues 12-13 (RMSD=0.59 Å). The NMR structure was generated from 204 upper distance limits (59 intraresidue, 85 short-range, and 60 medium-range) and 86 angular constraints (KIRCONG chimresidues are numbered asreported in figure S3), **(D)** putative pose of KIRCONG chimpeptide docked to JAK2: KIRCONG chiminteracting residues are highlighted with their van der Waals sphere, while those on JAK2 are reported in pink.Thr1026 and Leu1027 forming a hydrogen bond with Lys1 are also highlighted (dark green). Colour code: JAK2 (white), SOCS3 (gray), restKIR (blue), ESS(green), CONG (yellow).

The NMR result (**Figure 43C**) was used to model the peptide/JAK2 complex. Each NMR conformation of KIRCONG chim was docked to the SOCS3 binding site on JAK2 PDB: 4GL9 [230], chain A, (**Figure 44 a**). One pose was selected for each NMR conformation and, among the twenty

identified poses, seven presented the root mean squared deviation (RMSD) of heavy atoms of KIRCONG chim peptide with respect to the same atoms of SOCS3 below 1.30 nm (**Figure 44 b**). In particular, the closest pose (**Figure 44 d**) had RMSD 0.88 nm for restKIR, 0.69 nm for CONG and 0.80 nm for both fragments.

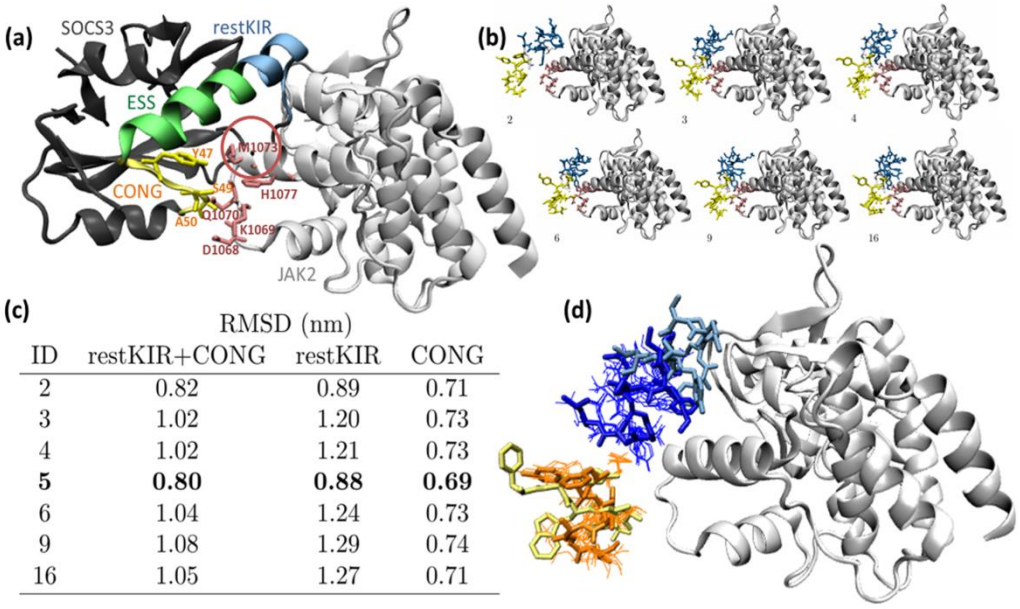

ID	restKIR+CONG	restKIR	CONG
2	0.82	0.89	0.71
3	1.02	1.20	0.73
4	1.02	1.21	0.73
5	**0.80**	**0.88**	**0.69**
6	1.04	1.24	0.73
9	1.08	1.29	0.74
16	1.05	1.27	0.71

Figure 44. (a) SOCS3/JAK2 (PDB): 4GL9 [230], chains A and E) with the fragment restKIRESSCONG and residues described in the text highlighted, and **(b)** selected putative poses of KIRCONG chim docket to JAK2, colour code: JAK2 (white), SOCS3 (gray), restKIR (blue), ESS(green), CONG (yellow). **(c)** Root mean squared deviation of the restKIR and CONG heavy atom fragments with respect to the same atoms in SOCS3, and **(d)** their overlap where the optimum pose (ID5 with RMSD=0.80) represented in orange/dark blue and the SOCS3 fragment yellow/blue are highlighted for comparison.

In this pose some peptide contacts are maintainedwith respect to SOCS3 (**Figure43D**): Phe^{25}, Lys^{28}, and Thr^{31} (Phe^{3}, Lys^{6} and Thr^{9} in the peptide numeration). Novel interactions are also formed: the new residue Lys^{1} is forming hydrogen bonds with both Thr^{1027} and Leu^{1026} and the βAla^{13} is interacting with JAK2 through van der Waals interactions. In comparison with the SOCS3/JAK2 crystal structure, JAK2 in complex with KIRCONG chim maintains contacts with both the restKIR fragment through Leu^{1026} and Thr^{1027} and with the CONG fragment through Gln^{1070}, Phe^{1076} and Glu^{1080} and new contacts involve Gln^{1072}, Met^{1073} and Lys^{1083}.

On the basis of the primary role exerted by both SOCS1 and SOCS3 proteins in the formation of atherosclerotic plaque[109, 231], we checked the activity of KIRCONG chim peptide in VSMCs and

macrophages, two major cellular constituents of atheroma plaques with an active role in atherogenesis. In these cellular assays with murine primary VSMCs and macrophage-like cell line (RAW264.7), we employed as control KIRESS peptide that, although had already demonstrated to act as mimetic of SOCS3, it has never been tested in these cells.

With the aim to check the stability of designed sequences during cellular experiments, the decrease of chromatographic peaks of pure SOCS3 derived peptides was followed during time. In **Figure 45 A,** the area percentages of peptides versus time of analysis is reported: after 2 h of incubation restKIRESSCONG peptide appeared completely degraded while KIRESS, and importantly KIRCONG chim, peptides present a residual concentration of 40% and 70 %, respectively. The greater stability shown by KIRCONG chim is likely due to the presence of three β-alanines as unnatural amino acid. On this basis, we checked the cellular effects of only KIRESS and KIRCONG chim sequences, excluding restKIRESSCONG that appeared to be easily degraded in cellular media and ESSCONG that did not provide a significant binding in MST experiments (**Figure 40A**). Confocal microscopy images of mouse VSMCs treated with fluorescent-SOCS3 peptides are reported in **Figure 45 B-C**: their inspection revealed an efficient and similar uptake of KIRESS and KIRCONG chim peptides after 2h, exhibiting a prevalent cytoplasmic distribution. Subsequently, immunofluorescence experiments in VSMCs revealed that both KIRESS and KIRCONG chim inhibited cytokine-induced STAT3 activation, as evidenced by a 65% reduction of STAT3 phosphorylation (P-STAT3) and nuclear translocation (**Figure 45 D-H**).

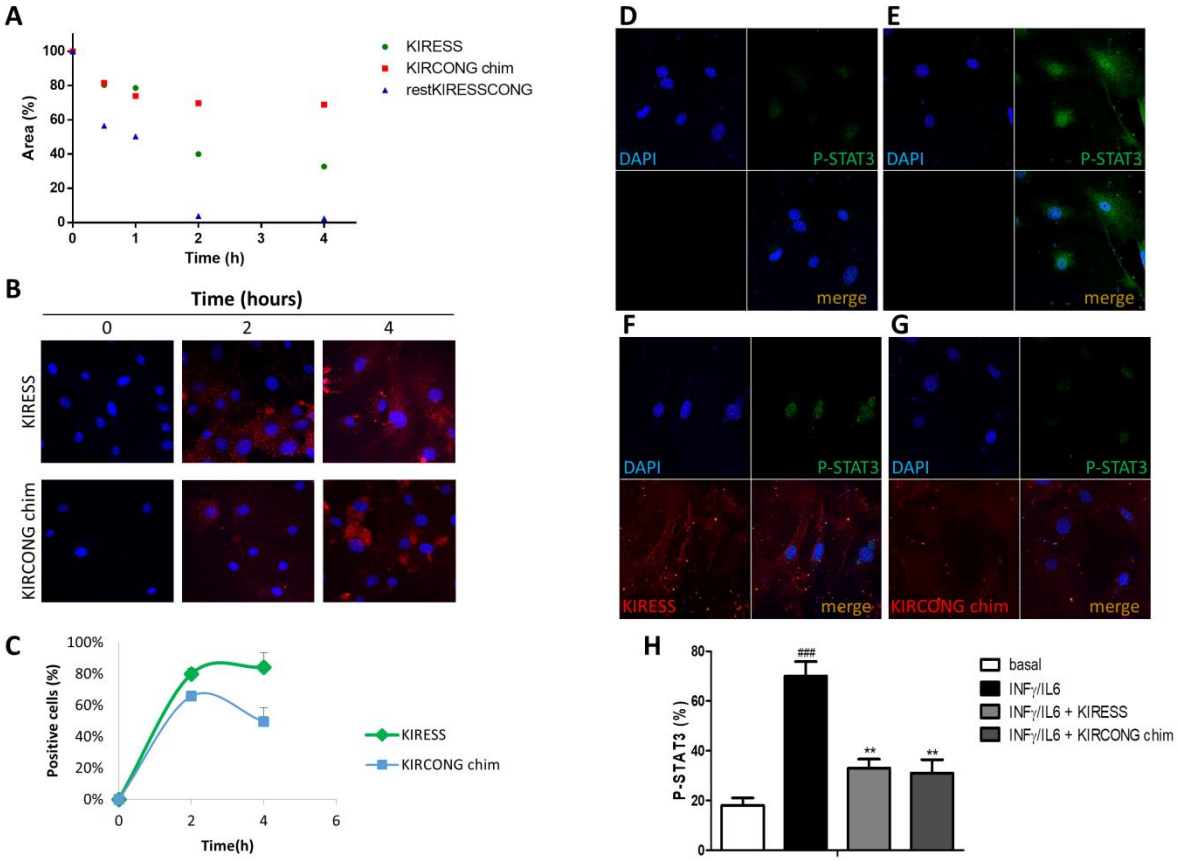

Figure 45. Effects of SOCS3 derived peptides on JAK/STAT pathway. Serum stability (A) and confocal images of VSMC (B) showing peptide internalization at different times. (C) Quantification of peptides internalization on the basis of TAMRA fluorescence intensity. (D-F) Representative confocal images of VSMCs under basal conditions (D) and stimulated with IFNγ+IL-6 in the absence (E) or presence of TAMRA-KIRESS (F) and TAMRA-KIRCONG chim (G) peptides (red, SOCS3 derived peptides; green, P-STAT3; blue, DAPI stained nuclei). (H) P-STAT3 fluorescence intensity percentages. Results are mean±SEM of 3 independent experiments (###P<0.001 vs basal; **P<0.01 vs cytokines).

The effects of SOCS3 derived peptides were also investigated in RAW264.7 macrophages under cytokine stimulation. The pretreatment of cells with KIRESS and KIRCONG chim peptides significantly reduced the mRNA expression of STAT-regulated pro-inflammatory genes such as *Cxcl10* and *Ccl5* chemokines[232](**Figure 46 A-B**). Moreover, as reported in **Figure 46C**, both peptides inhibited the gene expression of NADPH oxidase 2 (*Nox2*), a superoxide-generating enzyme that can be modulated by SOCS3 expression[233]. As expected, negative control (NC) peptide resulted inactive in cellular assays. Together, these *in vitro* results suggest an anti-inflammatory and anti-oxidant effect of SOCS3-derived peptides and support further investigation of their potential in inflammatory diseases, including atherosclerosis.

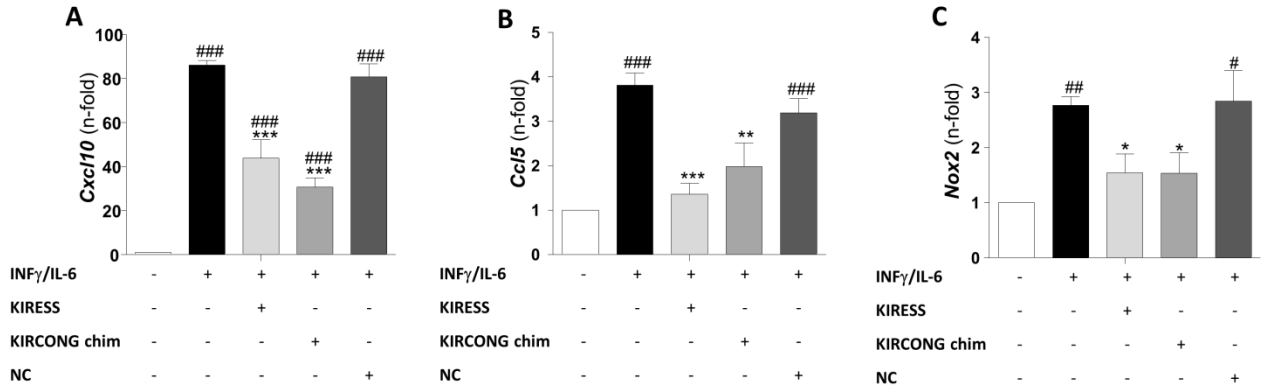

Figure 46. Real-time PCR analysis of STAT-dependent genes in macrophages. RAW264.7 cells were stimulated with IFNγ+IL-6 for 1 hour in the absence or presence of 12.5μM of SOCS3 peptidomimetics and NC peptide. The mRNA expression levels of CXCL10 (A), CCL5 (B) and NOX2 (C) were normalized to 18S and expressed as fold increases over basal condition. Mean±SEM (#P<0.05, ##P<0.01, ###P<0.001 vs basal; *P<0.05, **P<0.01, ***P<0.001 vs cytokines) of 3 independent experiments.

2.1.2. SOCS1: Analogues of PS5 compound

2.1.2.1. 1st generation of PS5 analogues

With the aim to develop a new SPR-based binding experiment for further identification of mimetics of KIR of SOCS1, we initially set up an assay in which the biotinylated catalytic domain of JAK2 (826-1132 aa) was immobilized on a SA chip. We employed a sandwich immobilization by using commercially available biotinylated catalytic domains of JAKs on SA-coated chip. To assess the correctness of the designed assay, we analyze the binding affinities of known KIRESS derived peptides of SOCS1 (reported in **table 8**) toward JAK kinase domains: in **Figure 47** the overlays of sensorgrams for KIR, KIRESS and PS5 on immobilized JAK2 protein are reported.

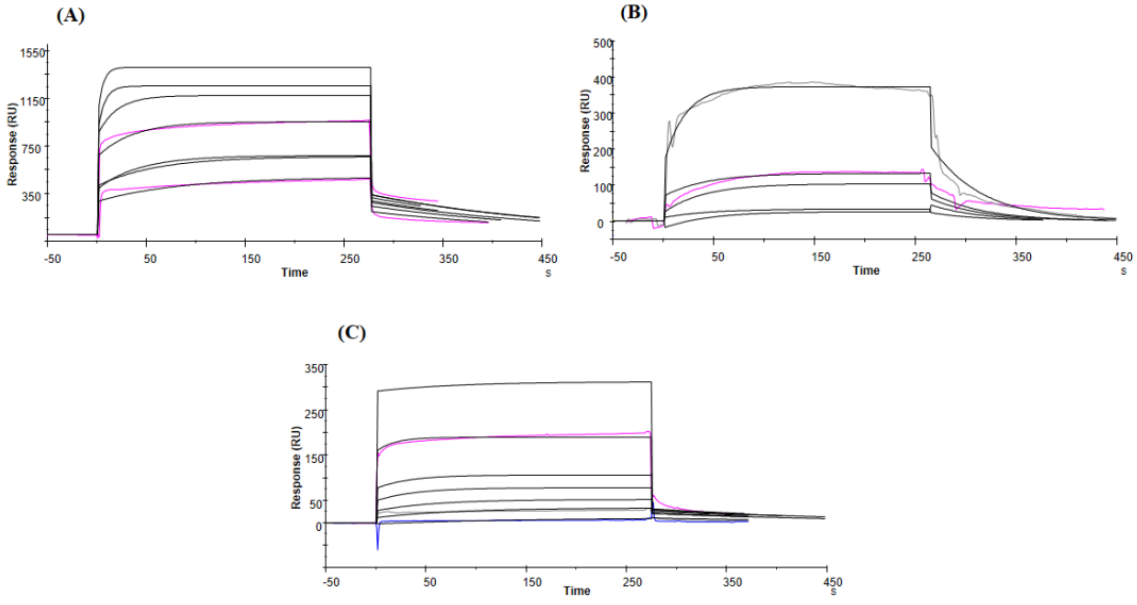

Figure47. Overlays of sensorgrams for A) KIR, B) KIRESS and C) PS5 on immobilized JAK2 protein.

Dose-response signals clearly indicate association, and kinetic parameters allowed to estimate K_D values, reported in **table 8**, that are in good agreement with those obtained with enzyme-linked immunosorbent assay (ELISA) [139] and fully consistent with those reported for the entire proteins [234].

Table 8: Kinetic (k_a, k_d) and dissociation constants (K_D)values of the affinity of SOCS1 peptidomimetics analyzed in this study toward JAK2.

Peptide	Sequence	ka (1/Ms)	kd (1/s)	K_D (μM)
KIR SOCS1	^{52}DTHFRTFRSHSDYRRI^{67}	66.3	0.00504	76.6
KIR ESS SOCS1	^{52}DTHFRTFRSHSDYRRITRASALLDACGF^{79}	142	0.0199	139
linear PS5	AcDTC(Acm)RQTFRSH	544	0.00272	7
cyclic PS5	Ac**C**GDTC(Acm)RQTFRSHG**C**	90.2	0.00586	65
linear PS5 Nal1	AcDTC(Acm)RQTNalRSH	235	0.00400	17
cyclic PS5 Nal1	Ac**C**GDTC(Acm)RQTNalRSHG**C**	165	0.00425	25.8

For the first time, we analyzed the contribute of ESS region to the binding of KIR domain of SOCS1 to JAK proteins, since an important crucial synergy between these fragments in the analysis of mimetics of SOCS3 in the interaction with JAK2 was recently discovered by us [235]. Interestingly and differently from SOCS3, we argued a negative interference of ESS sequence to the binding of KIR domain by both analyzing the peptide ESS alone and in combination with KIR (**table 8**): indeed, the presence of ESS led to a minor affinity of KIR toward JAK2 (**figure 47B**), while ESS sequence alone gave no association signals (**table 8**) (data not shown). These observations also support the minimizing process we followed on the KIR peptide (16 residues) to generate the shorter peptidomimetic PS5 (10 residues) [139]. PS5 demonstrated able to bind to JAK domain (**figure 47C**) in our SPR assay with an affinity in good agreement with that estimated *via* ELISA isothermal binding (K_D ~5 μM)[139].

With the aim to test the versatility of PS5 compound to mimic SOCS1 protein functions, we analyzed the impact of PS5 on the response of VSMCs, the most abundant cells of blood vessels that directly control vascular tone and are involved in the pathogenesis of inflammatory vascular disease. To allow and evaluate cell penetration, we conjugated PS5 to TAT derived cell penetrating sequence [139] labelled with a TAMRA fluorophore. Confocal microscopy in mouse VSMCs revealed efficient uptake of fluorescent PS5 peptide over time and cytoplasmic distribution (**Figure 48A**).

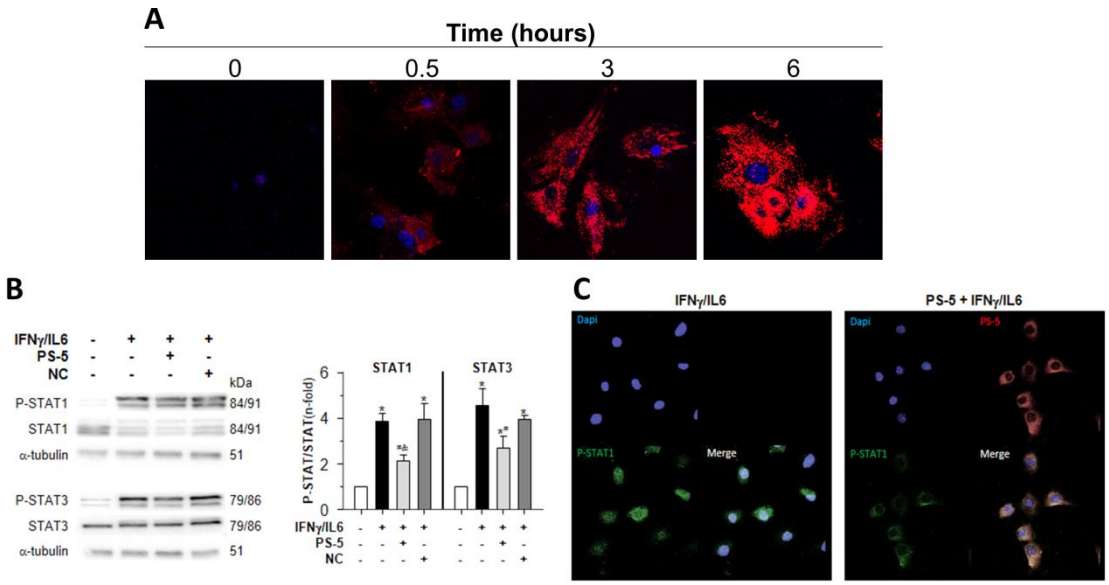

Figure 48. Biodistribution and functional effect of PS5 peptide *in vitro*. **A)** Representative fluorescent confocal images (n=3) showing cytosolic distribution of TAMRA-conjugated PS5 peptide (75 µM) over time; **B)** Western blot analysis of P-STAT1/3, total STAT1/3 and α-tubulin (loading control) in mouse VSMCs stimulated with cytokines (IFNγ plus IL-6, 60 min) in the absence or presence of PS5 and NC peptides (41 µM). Representative immunoblots are shown, with summary of normalized densitometry data expressed as fold increases over basal conditions. Mean±SD (*P<0.05 vs basal, $^{\#}$P<0.05 vs cytokines, $^{\&}$P<0.05 vs NC). **C)** Confocal images (red, PS5; green, P-STAT1; blue, DAPI stained nuclei; n=2) showing P-STAT1 localization in cytokine-stimulated VSMCs and the inhibitory effect of PS5 peptide.

Further, we analyzed the ability of PS5 to inhibit cytokine-induced STAT activation and downstream gene expression. Western blot analysis (**Figure 48B**) demonstrated that pretreatment of VSMCs with PS5 peptide, but not with the unrelated sequence NC, reduced STAT1 and STAT3 phosphorylation induced by a combination of pro-inflammatory cytokines (IFNγ plus IL-6). Internalized PS5 peptide was also able to inhibit STAT1 nuclear translocation (**Figure 48C**). Finally, quantitative real-time PCR analysis showed a reduced expression of STAT-dependent genes (*Ccl2* and *Ccl5*) by PS5 peptide in cytokine-stimulated VSMCs (**Figure 49**).

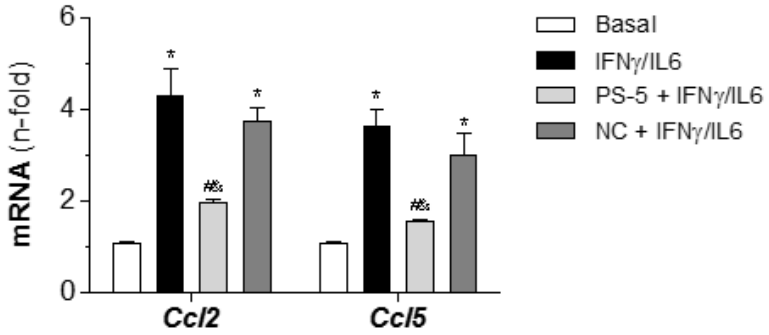

Figure 49. PS5 prevents chemokine expression in vascular cells. Quantitative real-time PCR analysis of chemokine genes in VSMCs treated with PS5 and NC peptides (41 μM, 90 min) prior to cytokine stimulation (IFNγ plus IL-6, 6 hours). Ccl2 and Ccl5 mRNA expression levels were normalized by 18S endogenous control and expressed as fold increases vs basal. Mean±SD (*P<0.05 vs basal, $^{\#}$P<0.05 vs cytokines, $^{\&}$P<0.05 vs NC).

PS5 peptide (**table 8**) contains a non-natural residue (Cys(Acm)) that renders this sequence more stable to protease degradation with respect to natural sequences [139, 141]. To increase this stability, firstly we designed a cyclic analog, cyclic PS5, in which a disulfide bridge between two cysteines added at the extremities was inserted. N-terminally respect to the cysteines two glycines were added to the PS5 sequence as spacers to allow a better exposure of the recognition sequence. The phenylalanine at position 58 appeared crucial from both point mutations analyses on the entire protein [236-237] and Ala-scanning of KIR sequence [139]. To investigate the role of this residue and to further rigidify the structure of the peptidomimetic, we have developed two similar cyclic analogues in which Phe[58] was substituted with non-natural naphthyl, obtaining two variants bearing Nal1, one linear (named linear PS5 Nal1) and its cyclic form (named cyclic PS5 Nal1). The naphthyl group, being formed by two aromatic rings, once inserted, increases the structural rigidity of the peptide sequences[238].

New designed PS5 derived peptides were assayed for their ability to bind to JAK2 catalytic domain through the above-described assay. Linear PS5 Nal1 sequence demonstrated a similar affinity with respect to PS5 (data not shown). The overlays of sensorgrams relative to the binding of cyclic PS5 and cyclic PS5 Nal1 are reported in **Figure 50 A and B**, respectively and kinetic parameters allowed to estimated dissociation constants in the micromolar range. If compared none of new analogues provided greater affinity toward JAK2 with respect to linear PS5 but several differences in kinetic features allow to suppose diverse mechanism of recognition. Indeed, the substitution of Phe with un-natural Naphthyl-alanine provided similar affinity with respect to linear PS5 (**table 8**). On the

other hand, the cyclization seemed to interfere negatively with recognizing ability of PS5 sequence lowering its affinity of almost ten-fold factor but in a similar cyclic context, the naphthyl group induces an enhancement of affinity of two fold. In detail, the naphthyl moiety delays the dissociation phase, lower kd values in both analogue peptides, prompting to supposed to an enhancement of aromatic interactions within the catalytic site of the kinase.

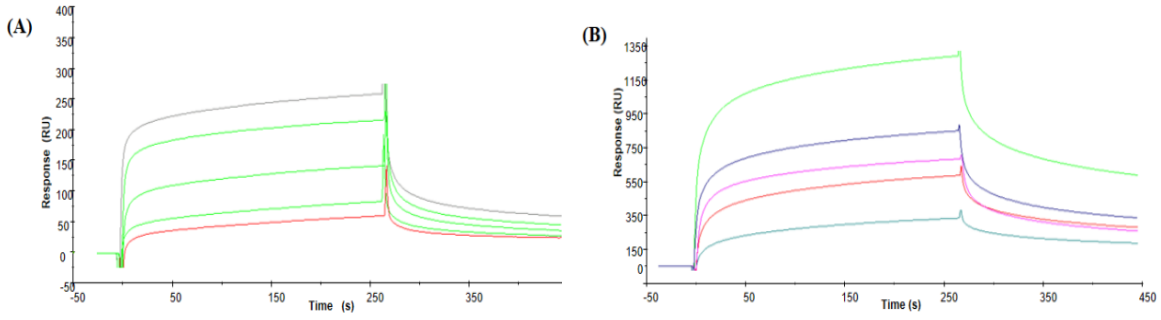

Figure 50. Overlay of sensorgrams related to the binding of **(A)** cyclic PS5, **(B)** cyclic PS5 Nal1 on biot-JAK2 immobilized on a SA-chip.

In order to evaluate the conformational properties of designed peptidomimetics, preliminary CD [239] and NMR spectroscopic analyses were carried out. In a predicted model of SOCS1, the KIRESS domain contained two short α- helices (R56–R69 and L73–A76) linked by a small coil segment [215] that are almost left out in PS5 sequence, indeed its CD spectrum suggested a prevalent random coil content[139] as also predicted through disorder propensity algorithms (as PONDR-FIT [240, 32]). The intrinsic flexibility of the sequence was confirmed by the linear version of PS5 Nal1 that showed a CD spectrum with the minimum at a wavelength minor to 200 nm.

In **Figure 51A** the overlay of CD spectra of cyclic peptides PS5 and PS5 Nal1 is reported. They show profiles not ascribable to canonical structures but the slight shift of their minima at ~203 nm suggests that the disulfide bridge could induce a certain level of restriction with respect to linear version of these sequences. 2D [^{1}H, ^{1}H] NMR spectroscopic investigations **Figure 51B-C** clearly indicate that these cyclic peptides are too flexible, in aqueous buffer, to be deeply investigated. The 2D TOCSY spectra (**Figure 51B**) are characterized by a poor chemical shift dispersion, while only a reduced number of signals are evident in the 2D [^{1}H, ^{1}H] NOESY experiments (**Figure 51C**). These features are indicative of conformational disorders[6] and, in agreement with CD data, point towards the lack of canonical secondary structure elements.

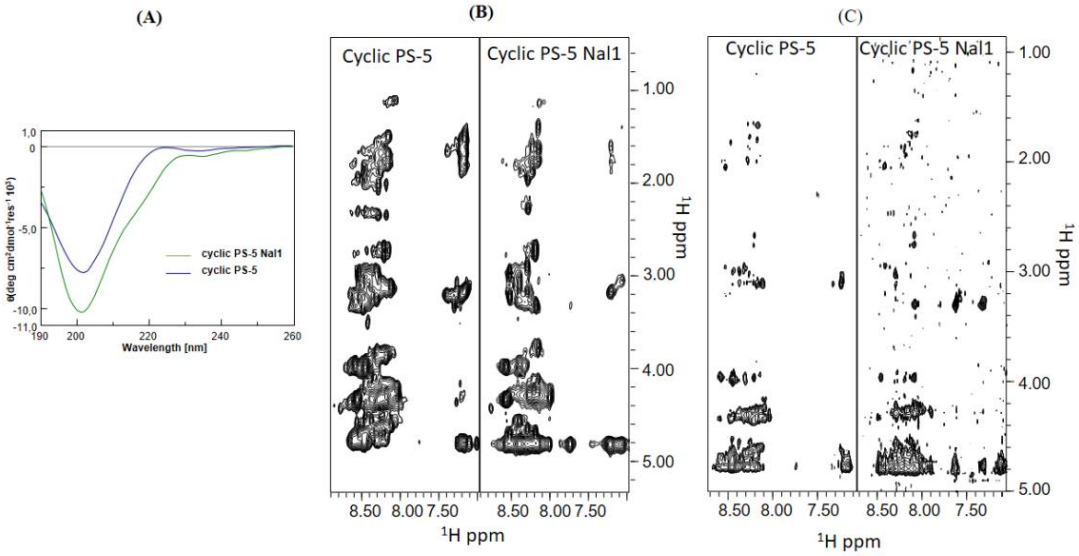

Figure51. (A) Overlay of CD spectra of cyclic PS5 and PS5 Nal1, comparison between 2D [^{1}H,^{1}H] TOCSY **(B)** and NOESY **(C)** spectra of cyclic PS5 peptides. The correlations region containing signals involving H_N protons are reported in each panel (B, C).

To investigate the effects of the modifications of PS5-derived sequences on their proteolytic susceptibility, we followed the decrease of chromatographic peaks of pure peptides incubated in diluted serum at 37°C (**figure 52**). After 16 h of treatment PS5 sequence appeared almost completely degraded while cyclization induce a residual concentration of ~ 50%, while for other analogues it is higher than 80% of the initial concentration. The higher level of stability shown by linear and cyclic PS5 Nal1 is due to the presence of the non-natural Naphthylalanine residue in addition to Cys (Acm) of PS5.

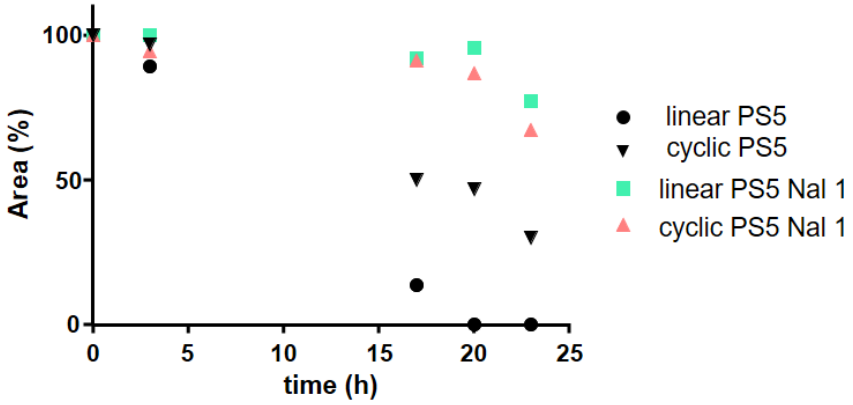

Figure52. Serum stability assay of 1st generation PS5 derived peptides.

2.1.2.2. 2nd generation of PS5 analogues

The structure of SOCS1/JAK1 complex showed that it is mediated by a continuous six residue segment of the KIR (His54 to Arg59), each is involved both in polar and/or hydrophobic interaction. The first of these, His54,is located between two planar side chains (His885 and Pro1044) from JAK1 while, Phe55 is the P + 1 residue of the pseudosubstrate of the kinase and, together with Phe58, form most of hydrophobic interactions that wedge KIR between the activation loop and the αG helix of JAK1. In this structure Phe58 sits in a hydrophobic pocket formed by the interface of JAK1 and SOCS1. Additional contacts are formed via hydrogen bonds between the sidechains of Arg56 and Arg59 with residues in the activation loop as well as a hydrogen bond between the side chains of Thr57 (SOCS1) and Ser1056 (JAK1) [99].

In order to increase its stability and affinity toward JAKs, we designed new analogues in which Phe58, crucial for the interaction with JAK2, was substituted with non-natural naphthylalanine, additional to Cys(Acm) already present in PS5 sequence, and a new small lactame bridge was introduced. Often the presence of naphthyl group, being formed by two aromatic rings, increases the structural rigidityof the peptides[238]. Thesenew cycles, constituted by 10 amino acids, were obtained through a peptide bond between side chains of aspartic acid and lysine and their chemical structures of new PS5 analogues are reported in **Figure 53**.

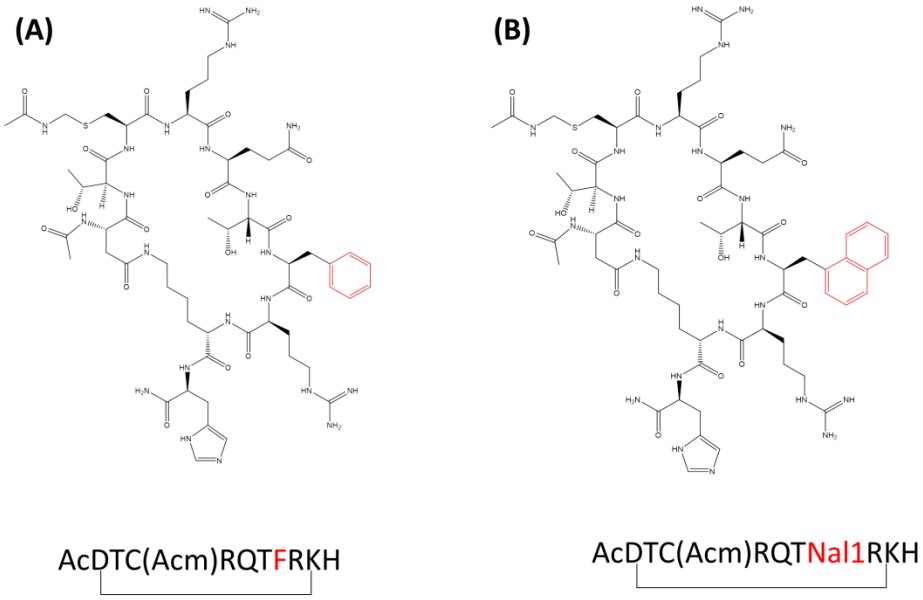

Figure 53. Chemical structure of **A)** Internal cyclic PS5 and **B)** Internal cyclic PS5 Nal1

New PS5 cyclic analogues were assayed for their ability to bind to JAK2 catalytic domain through SPR assay. The overlays of sensorgrams relative to the binding of internal cyclic PS5 and internal cyclic PS5 Nal are reported in **Figure 54 A** and **B** respectively. Employing kinetic parameters (**Figure 54**) estimated K_D values are in the micromolar range for both analogues but, interestingly, the analogue bearing the naphthyl group provided a slightly major affinity toward JAK2 with respect to linear PS5, showing a K_D= 5.45 µM, likely due to a faster association phase. Moreover, the "internal cyclization" seemed to negatively interfere with recognizing ability of linear PS5 sequence since it implies a 10-fold reduction internal of affinity.

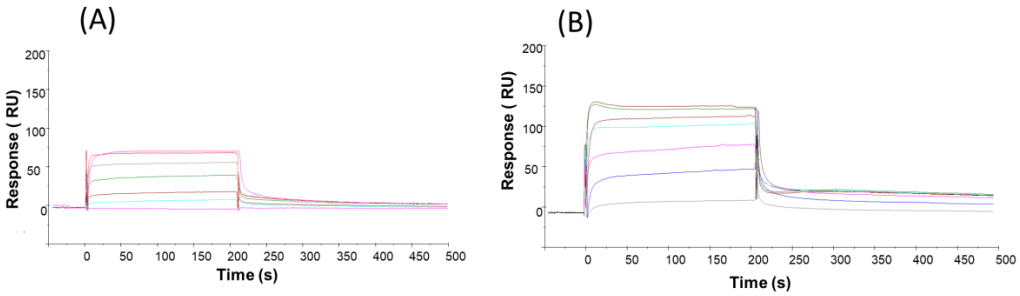

Peptide	ka (1/Ms)	kd (1/s)	K_D (µM)
Internal cyclic PS5	188	0.0148	82.3
Internal cyclic PS5 Nal1	713	0.00388	5.45

Figure 54. Overlay of sensorgrams related to the binding of **(A)** Internal cyclic PS5 and **(B)** Internal cyclic PS5 Nal1 on Btn-JAK2 catalytic site on a SA-chip.

In order to evaluate the conformational properties of designed peptidomimetics, CD and NMR spectroscopic studies were carried out. CD experiment reveal that both analogues do not show canonical profiles with a prevalent random contribution due to fact that absolute minima are located at λ≤ 200 nm. Moreover, in both cases "aromatic" bands are present: a negative shoulder for PS5 internal cycle (**Figure 55A**) and a more pronounced positive band for Internal cyclic PS5 Nal1 (**Figure 55B**), centered at 230 nm. For both compounds the evidence of aromatic contribution to the Cotton effect is likely due to the presence of a constrained cycle, indeed in the linear versions of these peptidomimetics these bands are absent [241]. In detail, Internal cyclic PS5 Nal1 presents also a shoulder at 222 nm suggesting a major helical content for 1-Nal containing sequence.

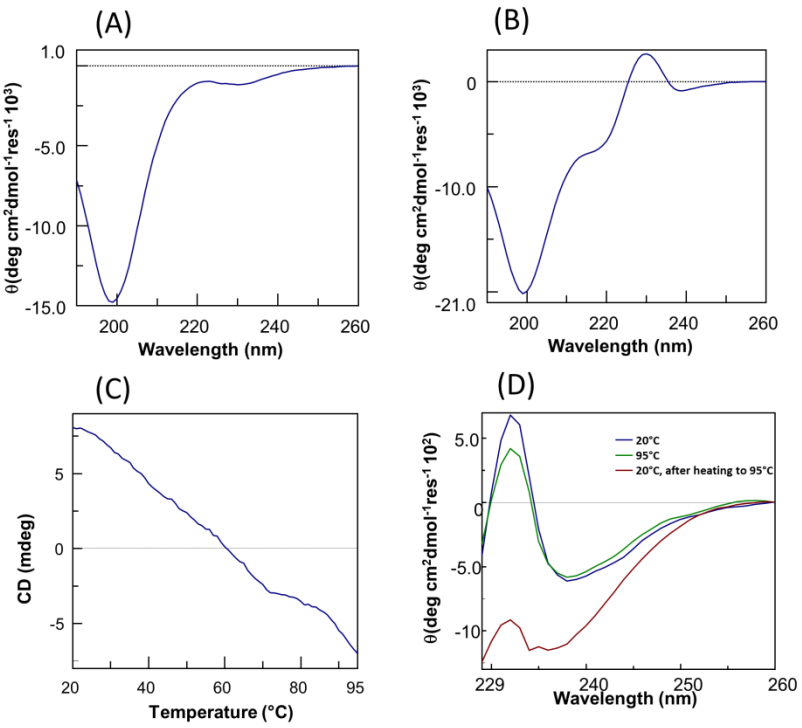

Figure 55. CD spectra of **A)** Internal cyclic PS5 and **B)** Internal cyclic PS5 Nal. **C)** Overlay of CD spectra of Internal cyclic PS5 Nal1 at indicated temperatures and **D)** variation of CD signal at 232nm in the range of 20-95°C.

On the other hand, the positive band at 232 nm for this compound could be due to an exciton effect [242] since it is lost upon increase of temperature in the range 20-95°C (**Figure 55C**). By comparing CD spectra at different temperatures, after cooling back the sample to 20°C this spectral change appeared reversible (**Figure 55D**).

The conformational properties of internal cyclic PS5 and internal cyclic PS5 Nal1 peptides were also investigated by means of NMR in H_2O/D_2O. To this aim different 2D [^{1}H, ^{1}H] NMR spectra were registered, and the analysis of TOCSY [149] and ROESY [151] experiments allowed to obtain complete peptide resonance assignments (**Figures 56**).

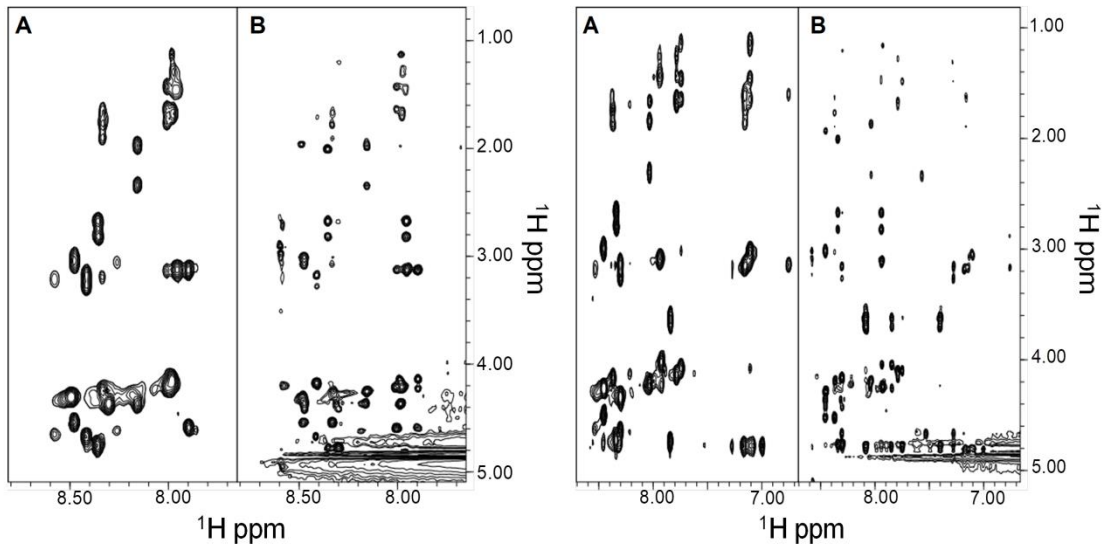

Figure 56. Aromatic/aliphatic regions of: right) Internal cyclic PS5 and left) Internal cyclic PS5 Nal1 2D [^{1}H-^{1}H] TOCSY **(A)** and ROESY **(B)** NMR spectra.

Inspection of NOESY [150] and ROESY spectra indicated that both peptides do not assume a rigid structure. In fact, analysis of ROEs patterns (**Figure 57**) in which sequential H_N-H_Ni+1 and Hα-H_Ni+1 contacts prevail, pointed out the absence of precise secondary structure elements [154]. Complete 3D solution structure calculations were conducted with the software CYANA [155] and confirmed a substantial flexibility of both compounds.

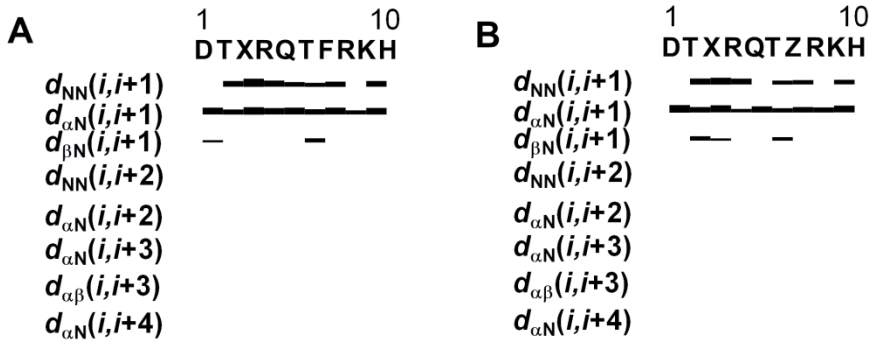

Figure 57. ROEs pattern of Internal cyclic PS5 **(A)** and Internal cyclic PS5 Nal1 **(B)** peptides. In the peptide sequences –shown on top- "X" and "Z" stand for C(Acm) and Nal1, respectively.

NMR structures were subjected to an unrestrained energy minimization procedure after which only 3/20 conformers of internal cyclic PS5 assumed a 3.10 helical conformation between Gln5 and Arg8 whereas just 2/20 conformers of internal cyclic Nal1 PS5 assumed a 3.10 helical/bend like conformation between Thr6 and Arg8.A cluster analysis of minimized structures was next carried out with the software Chimera [156, 243] by superimposing the twenty NMR conformers on

the backbone atoms (**Figures 58**). Clusterization further stressed out the conformational variability of the peptides in water. In fact, internal cyclic PS5 can be represented by 6 clusters of conformational related subfamilies (**Figure 58**), the two most populated ones contain 7 and 5 models, respectively (**Figure 58** upper panel B-C). Internal cyclic PS5 Nal1 NMR conformers can be grouped instead into 9 clusters, 5 of them represented by only 1 model (Table S3), and the two most populated ones containing each 6 and 5 conformers, respectively (**Figure 58** lower panel B-C).

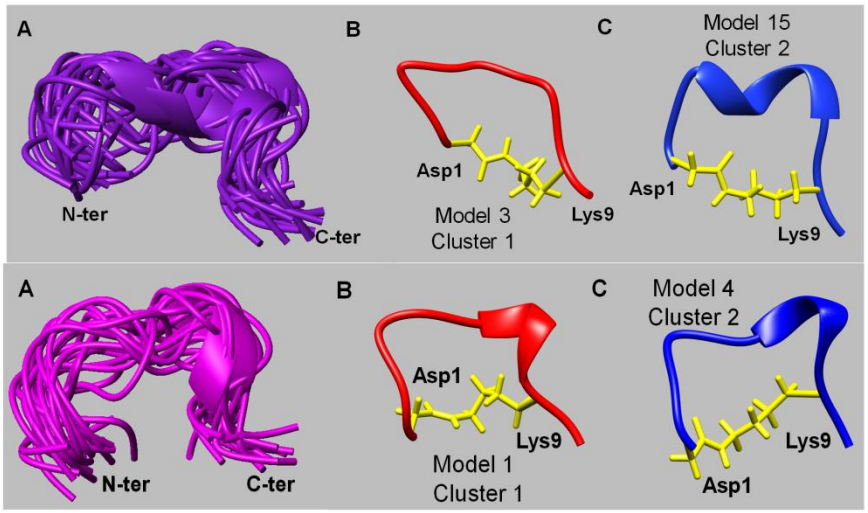

Figure 58. Upper panel) Internal cyclic PS5 peptide minimized NMR structure. (A) Twenty calculated conformers superimposed on the backbone atoms (ribbon representation, RMSDbb= 1.93 Å). (B, C) Representative models from most populated clusters. Peptide cyclization through Asp1 and Lys9 side chains is highlighted in yellow (B, C). Lower panel) Internal cyclic PS5 Nal1 peptide NMR structure after unrestrained minimization procedure (A) 20 NMR minimized conformers superimposed on the backbone atoms in ribbon representation ($RMSD_{bb}$= 1.71 Å). (B, C) Representative models from the most populated clusters. Peptide cyclization by means of Asp1 and Lys9 side chains linkage is shown in yellow.

The effect of internal cyclic PS5 analogues treatment of cells over time was consistent with their proteases' stability; indeed, in parallel with cellular assays we compared their stability in serum in comparison with linear PS5. As shown in **Figure 59**, during 17 hours, the cyclization was able to stabilize both internal cyclic analogues with respect to linear PS5 peptide that shows a degradation level of ~40%. However, after 20 h of treatment, the proteolytic degradation level of internal cyclic PS5 Nal1 was lower (~20%) with respect to internal cyclic PS5 (~40%) due to the presence of a non-natural naphthylalanine. This tendency was also confirmed at 42 h where the residual

concentration of internal cyclic PS5 Nal1 was still at ~40%, while the two other peptides appeared almost completely degraded.

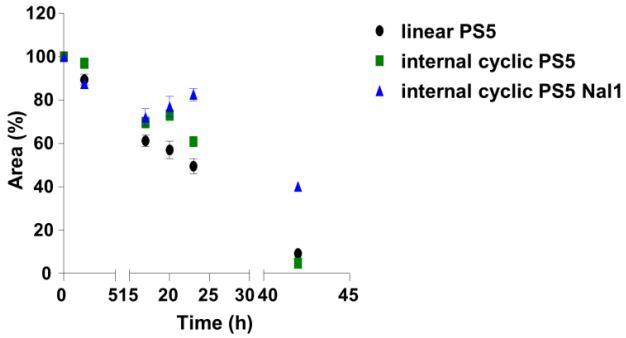

Figure 59. Serum stability assay of PS5 peptidomimetics. The serum stability of PS5 analogues was evaluated by incubation in 25% FCS for 42h. Residual peptide amount is expressed as the percentage of the initial amount versus time (n=3).

With the aim to test the activity of both internal cyclic peptides, and to compare their activity with linear PS5, we analyzed their effects in VSMCs. To allow and evaluate cell penetration, we conjugated PS5 analogues to TAT derived cell penetrating sequence labelled with a TAMRA fluorophore. As shown in **Figure 60**, confocal microscopy in mouse VSMCs revealed efficient uptake of fluorescent peptides over time and cytoplasmic distribution.

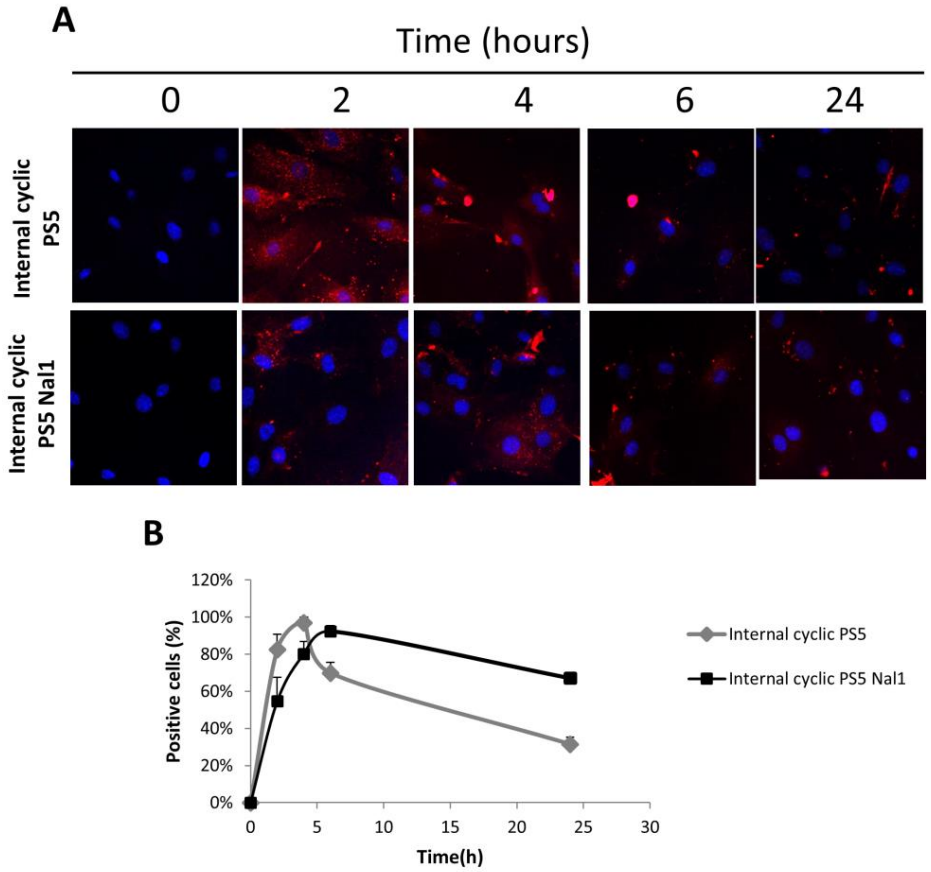

Figure 60. Biodistribution of PS5 analogues *in vitro*. A)Representative fluorescent confocal images (n=3) showing cytosolic distribution of TAMRA-conjugated internal cyclic peptides over time. **B)**Quantification of peptides internalization on the basis of TAMRA fluorescence intensity.

In **Figure 60B**, is reported the quantification of peptides internalization. As observed, both peptides show an efficienct uptake after ~2h; however, at 24h the internal cyclic PS5 peptide appear almost completely degraded while, instead internal cyclic Nal1 only for 40 % . This result is in line with previous observation: the presence of a non-natural naphthylalanine is able to reduce the proteolytic degradation.

Moreover, we checked how these peptides could interfere with cell viability and proliferation. As shown, both internal cyclic peptides as well as linear PS5, do not alter VSMC viability after 6h of treatment with 0.5% of FBS (**Figure 61A**). Moreover, after 24h all peptides exhibit no effect on cell proliferation as indicated in **Figure 61B**.

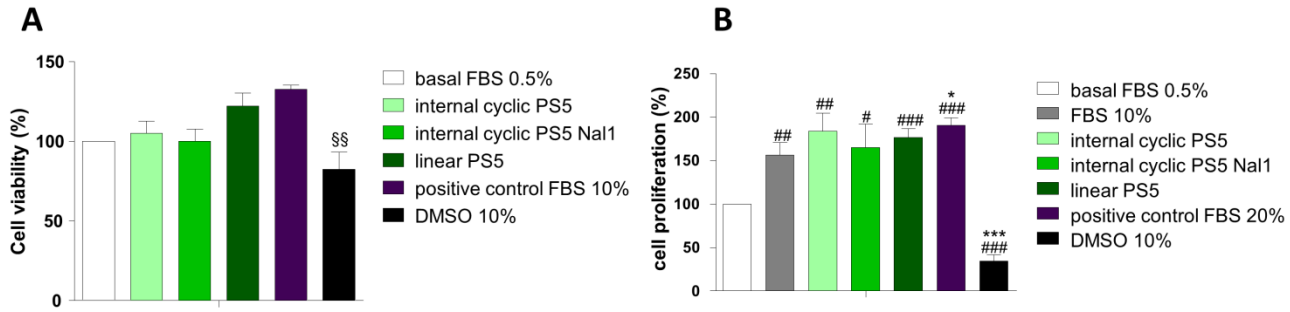

Figure 61. Effects of PS5 peptide and analogues on cell viability and proliferation. **A)** MTT Cell viability assay. Mean±SEM (§§P<0.01 vs positive control). **B)** MTT Cell proliferation assay. Mean±SEM ($^{\#}$P<0.05, $^{\#\#}$P<0.01, $^{\#\#\#}$P<0.001 vs basal, *P<0.05, ***P<0.001 vs positive control).

Since cell migration is an important process involved in plaque formation, we further analyzed the effects of peptides on VSMC migration (**Figure 62**). *In vitro* wound-healing assay with VSMCs demonstrated that IFNγ/IL-6 promoted a time-dependent increase of cell migration, while all three peptides exhibited an anti-migratory effect. The quantifications of covered healing areas (**Figure 62B**) showed that internal cyclic PS5 Nal1 was the most able to inhibit wound healing among peptides.

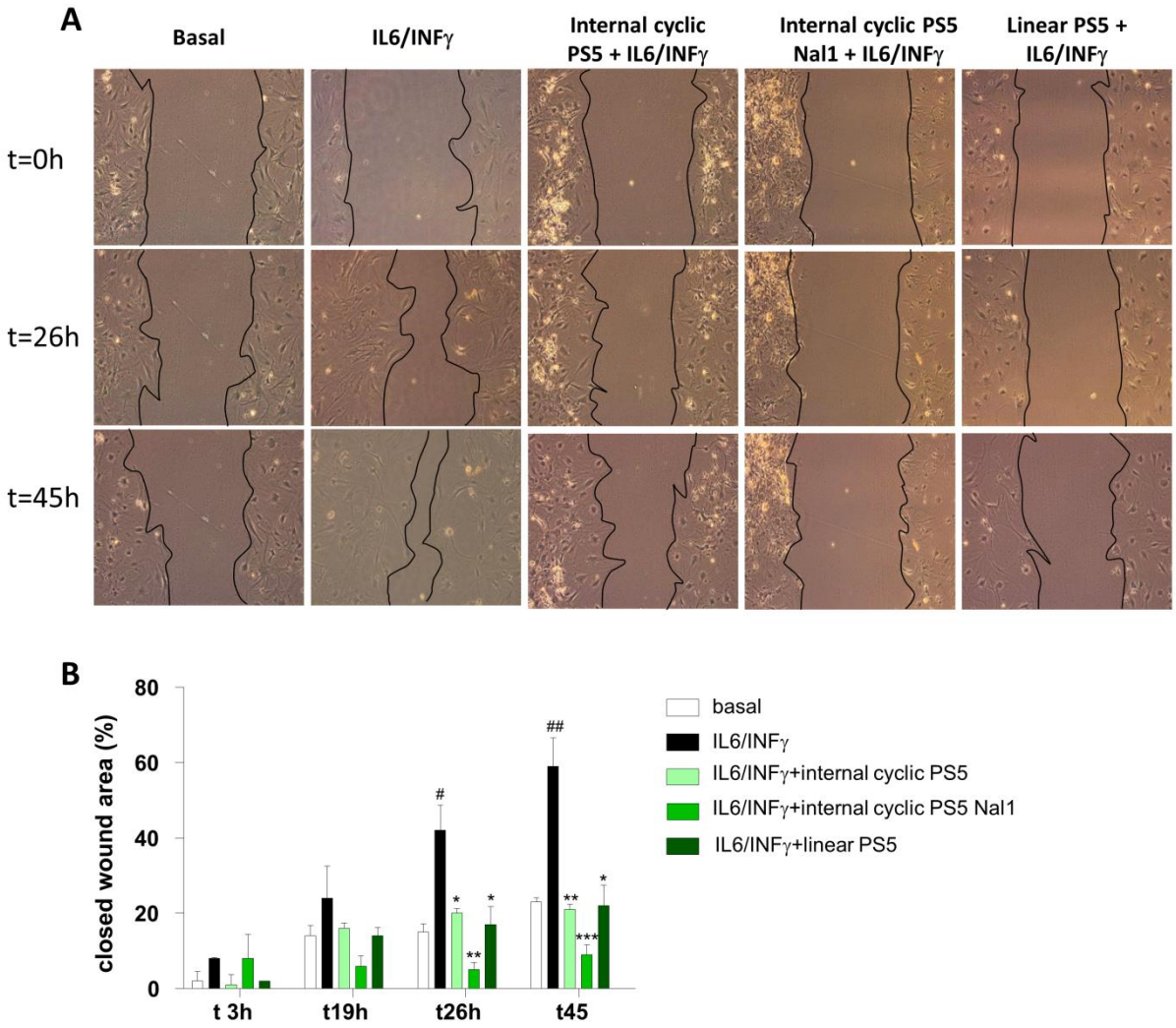

Figure 62. *In vitro* effects of PS5 peptide on cell migration. **A)** Representative images of scratch wound healing assay in VSMCs. **B)** Quantifications of covered healing areas at the indicated times are expressed as percentage of the initial wound area (n=3).

Further, we analyzed the ability of internal cyclic PS5 and internal cyclic PS5 Nal1 to inhibit cytokine-induced STAT activation and downstream gene expression. Immunofluorescence experiments revealed that internalized peptides were able to inhibit STAT1 phosphorylation (P-STAT1) and nuclear translocation in a significant way (**Figure 63A-E**).

Moreover, western blot analysis (**Figure 63F**) demonstrated that pretreatment of VSMCs with both internal cyclic peptides and linear PS5 reduced STAT1 phosphorylation induced by the combination of pro-inflammatory cytokines (IFNγ plus IL6). As expected, the unrelated sequence NC, did not show significant inhibitory activity.

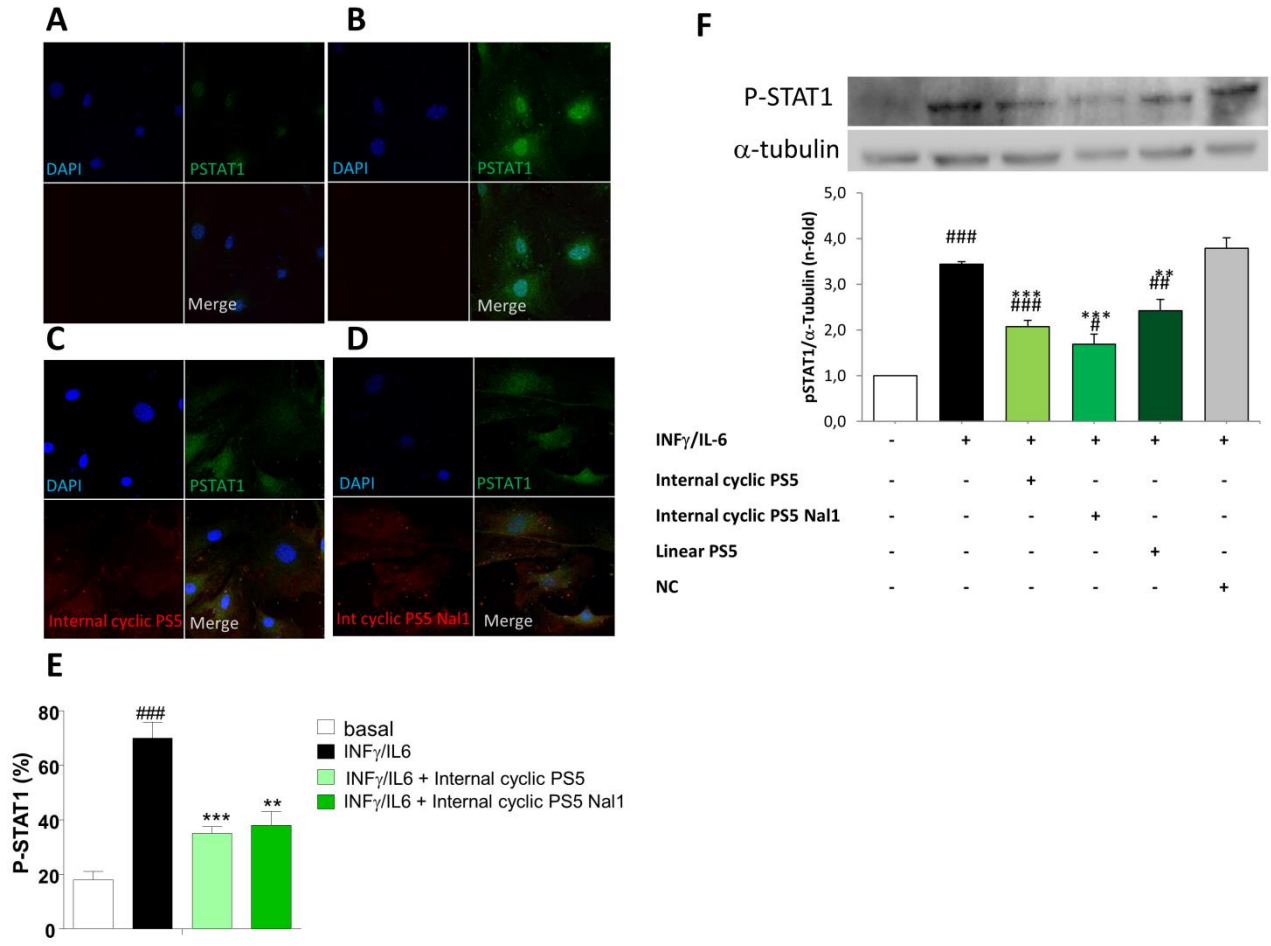

Figure 63. Inhibition of STAT phosphorylation by PS5 and analogues. **(A-D)** Representative confocal images (n=3 independent experiments; red, SOCS1 derived peptides; green, P-STAT1; blue, DAPI stained nuclei) of VSMCs under basal conditions **(A)** and stimulated with IFNγ+IL-6 in the absence **(B)** and presence of TAMRA-Internal cyclic PS5 **(C)** or TAMRA-Internal cyclic PS5 Nal1 **(D)**. **(E)** P-STAT1 fluorescence intensity percentages expressed as mean±SEM (###P<0.001 vs basal; **P<0.01, ***P<0.001 vs cytokines). **(F)** Representative immunoblots and densitometric analysis of P-STAT1 and α-tubulin (loading control) in mouse VSMCs stimulated with cytokines (IFNγ plus IL-6, 60 min) in the absence or presence of PS5 analogues and NC peptide (12.5 μM). Mean±SEM ($^{\#}$P<0.05, $^{\#\#}$P<0.01, $^{\#\#\#}$P<0.001 vs basal, **P<0.01, ***P<0.001 vs cytokines).

Furthermore, PS5 peptidomimetics significantly reduced mRNA expression of STAT-regulated pro-inflammatory genes such as *Cxcl10*, *Ccl2* and *Ccl5* chemokines (**Figure 64 A-C**). Moreover, the ability of 2nd generation analogues of PS5 to reduce the gene expression of NADPH oxidase subunits (N*ox1* and Nox4), was investigated since these enzymes are reported to generate ROS in VSMC[244]. Interestingly, as reported in **Figure 64D-E**, all peptidomimetics showed anti-oxidant effects by reducing the expression of both *Nox1* and *Nox4* genes.

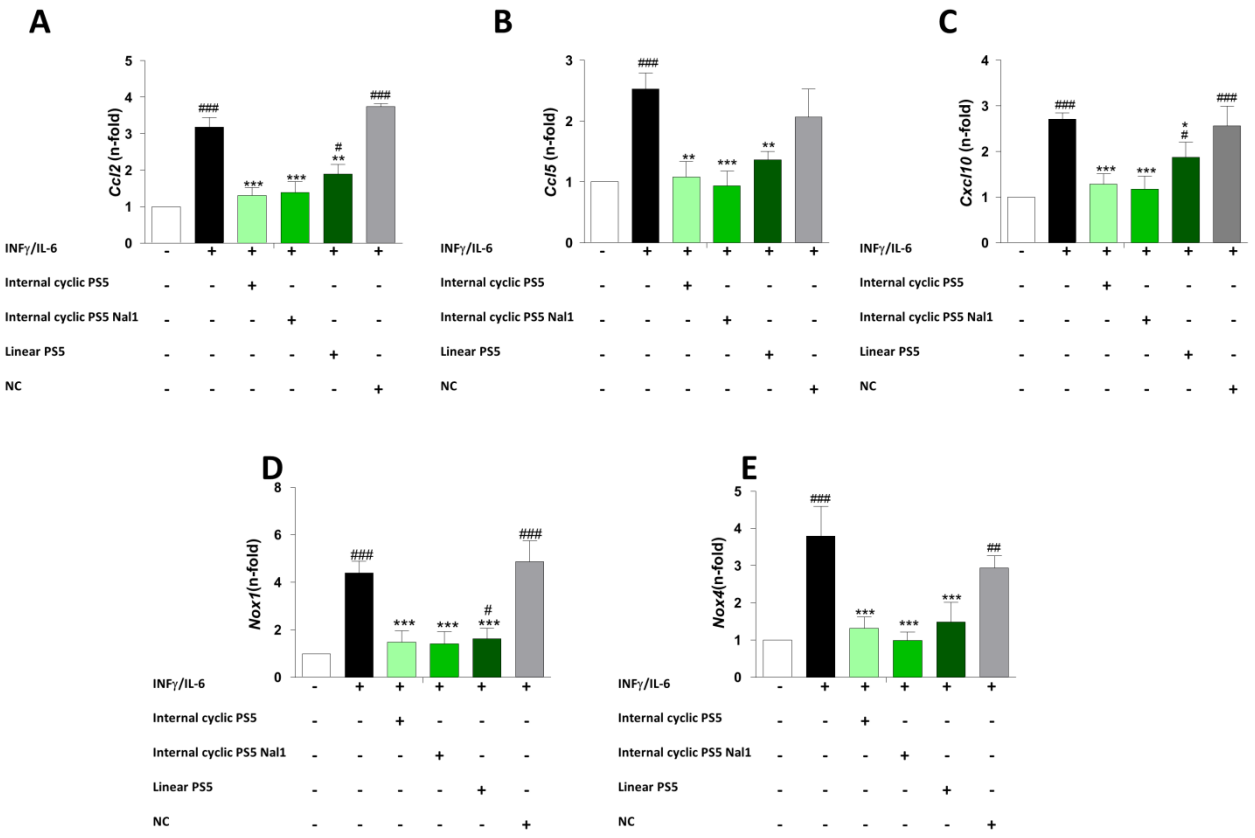

Figure 64. Real-time PCR analysis of STAT-dependent genes in VSMCs. Cells were stimulated with IFNγ+IL-6 for 6 hours in the absence or presence of 12.5µM of PS5 peptidomimetics and NC peptide. The mRNA expression levels of *Ccl2***(A)**, *Ccl5***(B)**, *Cxcl10***(C)**, *Nox1* **(D)** and *Nox4* **(E)** were normalized to 18S and expressed as fold increases over basal condition. Mean±SEM (#P<0.05, ##P<0.01, ###P<0.001 vs basal; *P<0.05, **P<0.01, ***P<0.001 vs cytokines).

In this field the production of superoxide anion in the VSMC was also analyzed by staining cells with DHE, a dye able to cross cell membranes and to emit fluorescence upon ROS oxidation. As shown in **Figure 65**, the DHE fluorescence induced by cytokine stimulation was reduced in the presence of PS5 analogues (at concentrations of 12.5 and 25µM), thus indicating an antioxidant effect.

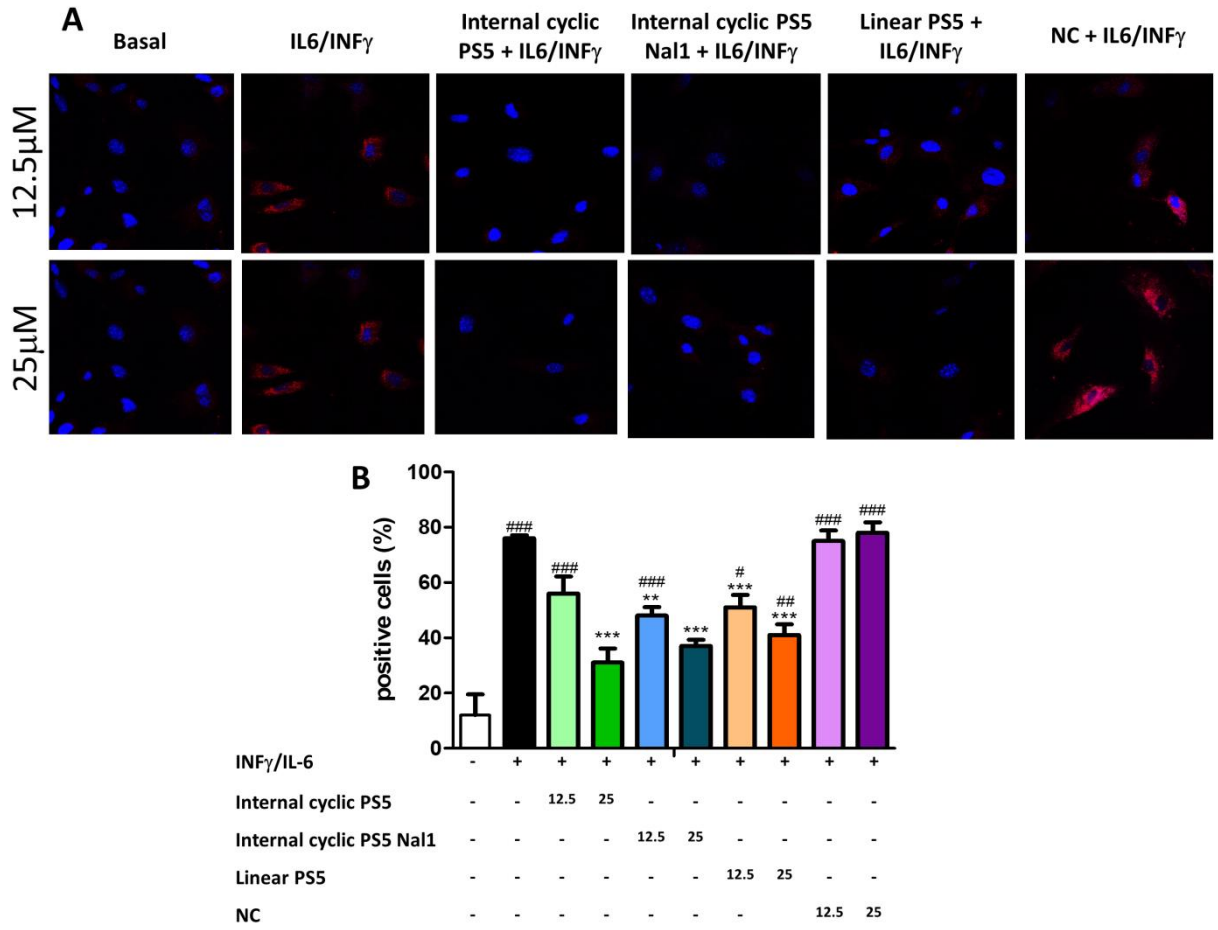

Figure 65. Antioxidant effect of PS5 peptides. **A)** Representative images (n=3) of DHE staining in VSMC that show an intense red fluorescence after 3 hours of stimulation with cytokines and a reduce fluorescence in presence of two differente concentrations of PS5 peptidomimetics (DHE, red; DAPI, blue). **B)** Quantification of peptides activity on the basis of DHE fluorescence intensity.

To further assess the anti-inflammatory and atheroprotective potential of PS5 derived peptides, their effects were investigated *in vivo* using an experimental model of atherosclerosis, the ApoE KO mouse. Firstly, biodistribution of TAMRA-peptides in mouse tissues was analyzed after by IVIS imaging after 6 and 12h ofintraperitoneal injection in ApoE KO mice and they were sacrificed. As reported in **Figure 66A**, all peptides were primarily localized in the liver and showed a clearance through the renal system. Subsequently, it was verified whether peptides effectively reached the target tissues, in this case the aorta of the ApoE KO mice. Confocal microscopy analysis (**Figure 66B**) revealed an accumulation of labelled peptides in the aortic plaques of mice, mostly at 6 hours after injection. After 24h, only internal cyclic PS5 Nal1 was detected due to its better resistance to the proteases degradation with respect to internal cyclic PS5 and linear PS5.

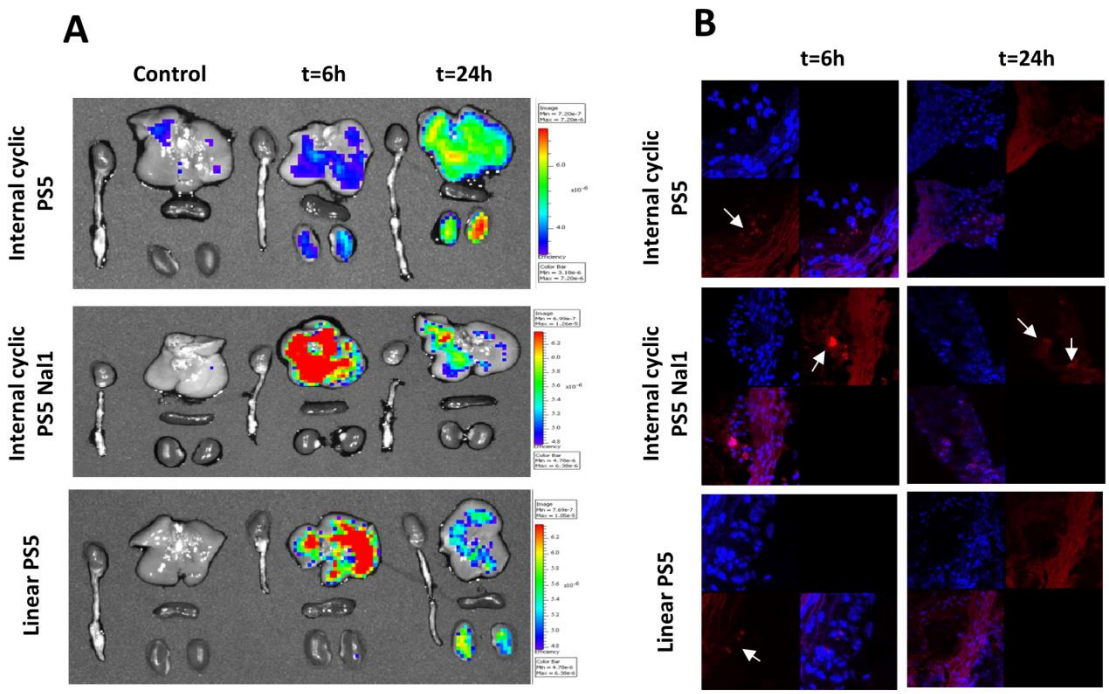

Figure 66. *In vivo* biodistribution of internal cyclic PS5, internal cyclic PS5 Nal1 and linear PS5 in ApoE KO mice. **A)** *Ex vivo* images showing tissue biodistribution of peptide at 6 and 24h post-injection. **B)** Representative confocal images of aorta cross-sections showing the localization of peptides (arrows) in the atherosclerotic lesion (TAMRA, red; DAPI, blue).

Subsequently, the effects of linear PS5 peptide on progression of atherosclerotic disease were investigated. Atherosclerotic phenotype was established in male ApoE KO mice (aged 8-10 weeks) by 8 weeks feeding of a high-fat diet. Mice were divided into 3 groups: 1) control, 2) mice treated with a low dose of peptide (~38μg/mouse) and 3) mice treated with high dose of peptide(~79μg/mouse). For the entire period, treated mice received intraperitoneal injections of linear PS5 peptide.

Quantification of aortic sections after oil-red-O/hematoxylin staining (**Figure 67A-B**) demonstrated that linear PS5 treatment at both doses resulted in a significant decrease in the size of atheroma plaques (40-45%) when compared with untreated control group. Atherosclerotic lesions from PS5-treated mice also exhibited a reduced content of neutral lipids (**Figure 67C**).

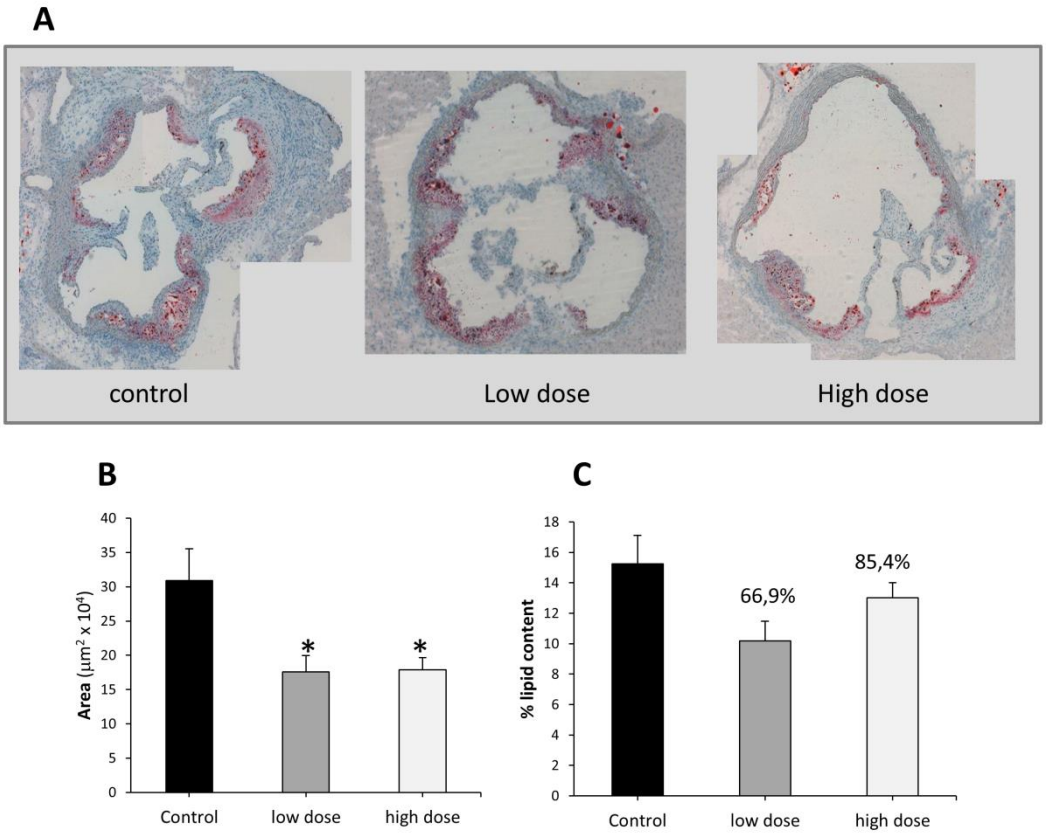

Figure 67. PS5 peptide therapy alters the size and lipid content of mouse atheroma plaques. **(A)** Representative images of Oil-red-O/hematoxylin staining in aortic sections from ApoE KO mice untreated (control) and treated with low and high doses of PS5 peptide. Quantifications of atherosclerotic lesion area (μm^2, **B)** and lipid content (% oil-red-O per lesion area; **C**) are shown. Values are expressed as mean±SEM of n=6-7 animals per group (**P*<0.05 vs control).

Moreover, quantitative real-time PCR analysis (**Figure 68**) in aortic samples of linear PS5-treated mice demonstrated a reduced local expression of CCL2/CCL5 and CXCL10 chemokines compared with controls (**Figure 68 A**). Finally, we also observed an *in vivo* antioxidant effect of PS5, as evidenced by increased expression of the antioxidant enzymes superoxide dismutase 1 (S*od1*) and catalase (C*at*) (**Figure 68 B**) and downregulation of superoxide-generating enzyme *Nox1* (**Figure 68 C**) .

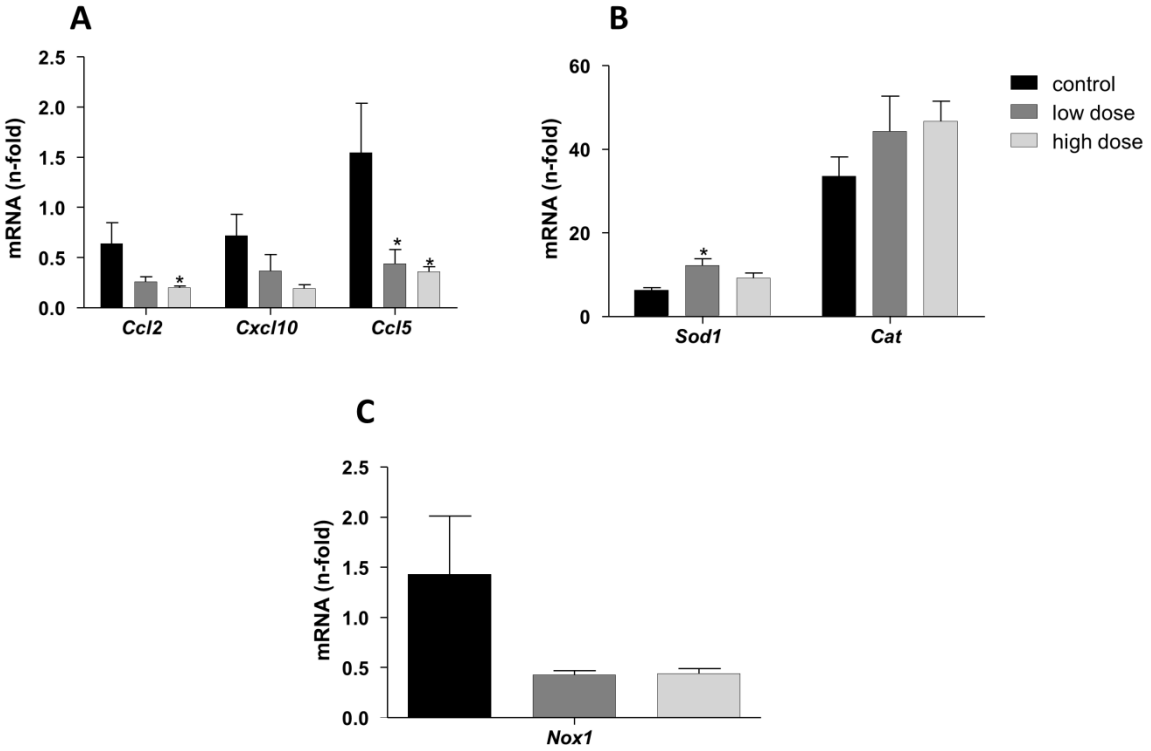

Figure 68. Real-time PCR analysis in aortas of used mice. The mRNA expression levels of *Ccl2*, *Ccl5* and *Cxcl10* **(A)**, *Sod1* and *Cat* **(B)**, *Nox1* **(C)** were normalized to 18S and expressed in arbitrary units (a.u.). Mean±SEM of n=6-7 animals per group (**P*<0.05 vs vehicle).

2.2 Discussion

SOCS family of proteins exert a primary role in the regulation of cytokine signaling [237,245] . Indeed, many studies on gene-disrupted mice revealed profound roles exerted by SOCS proteins in many immunological and pathological processes. On the other hand, the effects of their over-expression or exogenous administration suggested them as crucial pharmaceutical targets in several inflammation-related diseases as rheumatoid arthritis[246], severe acute pancreatitis[247]and metabolic dysfunction induced by obesity[248]. In particular, mimetics of SOCS1 demonstrated endowed with potential therapeutical applications[96-98, 249,231,250-251].

In this thesis we focused our attention on the design of more potent mimetics of KIR SOCS1 and *de novo* mimetics of SOCS3 proteins.

On the basis of protein interfaces between SOCS3 and JAK2, a linear peptide named KIRESS, encompassing the N-terminal region of SOCS3 was designed. This peptide demonstrated to contain the main hot-spots for the recognition of JAK2, and to be endowed with a prevalent α-helical propensity. Its therapeutic potential for the treatment of TNBC was investigated in human breast tumor xenografts: it demonstrated an ability to reduce tumor growth and eliminate pulmonary metastasis.

Subsequently, we decided to focus the attention on other regions involved in the interaction with JAK2: sequences spanning several SOCS3 fragments, contiguous and not, including the so-called CONG motif that in the protein architecture acts as a hinge between N-terminal KIR region and SH2 domain, and that seemed to have hot spots of interaction with JAK2 catalytic domain. All designed sequences were analyzed in their recognition ability to bind to JAK2 through MST assay. In detail, a chimeric peptide including not contiguous protein fragments, KIR and CONG sequences, named KIRCONG chim, revealed able to recognize JAK2 exhibiting a low micromolar value of dissociation constant. This sequence resulted endowed with a good propensity to assume α-helical conformations, as outlined by NMR investigations. Its anti-inflammatory properties were further investigated in primary mouse VSMCs and RAW264.7 macrophage cell line. The presence of KIRCONG chim as well as of KIRESS reduced the phosphorylation and nuclear translocation of STAT3, further preventing the expression of several STAT-dependent genes. Overall data indicate the importance of helical content and aromatic contribution in the recognition of SOCS3 peptidomimetics toward JAK2, and that may possess a therapeutic potential in many diseases with activated inflammatory cytokines. The limited water solubility and high molecular weights of

KIRCONG chim as well as of KIRESS sequences make these compounds unsuitable to be used as they are as drugs, but pave the way for the design of new molecules preferably macrocycles[252] through structural and chemical modifications of investigated linear sequences.

The research group in which I spent my PhD thesis, have developed a KIR SOCS1 derived peptidomimetic, named PS5. It demonstrated able to bind to JAK2 both in phosphorylated and not-phosphorylated form, and its peptoid nature makes it more stable to protease degradation and suitable for testing in cellular based experiments. In IFNγ-activated human keratinocytes, PS5 impaired JAK2, IFNγRα, and STAT1 phosphorylation and reduced the gene expression of the IRF-1 transcription factor, and several inflammatory genes including ICAM-1, HLA-DR, CXCL10 and CCL2. Here with the aim to ameliorate the affinity toward JAK2 and to improve drug-like properties, new PS5 peptidomimetics were designed.

First of all, to further shed light on the versatility of the anti-inflammatory actions of PS5-based compounds, PS5 were tested in the most abundant cells of blood vessels involved in inflammatory vascular diseases, the VSMCs. In these experiments, PS5 drastically reduced STAT1 and STAT3 phosphorylation induced by a combination of cytokines (IFNγ and IL-6).. In parallel, several STAT-dependent genes, such as *Ccl2* and *Ccl5* chemokines*,* were repressed by PS5.

Based on these results, we designed several 1st generation peptidomimetics derived from PS5 bearing two unnatural features: i) a disulfide bridge between additional external cysteine residues; and ii) one additional un-coded amino acid, Nal1, substituting the well conserved Phe^{58}. Binding affinity experiments and conformational studies did not suggest an improvement of the affinities toward JAK2 since the head-to tail cycle partially masks the recognizing sequence, in cyclic PS5, while an affinity comparable to linear PS5 was rescued in the cyclic PS5 Nal1 maybe for an enhancement of aromatic interactions due to the presence of Nal 1 building block. Noticeably, serum stability experiments clearly indicate that the insertion of un-natural building blocks further improved proteases' resistance and it appears a powerful tool to deeper investigate cellular effects of synthetic mimetics of SOCS1.

Starting from these considerations, the design of 2nd generation peptidomimetics derived from PS5 was performed. Particularly two internal cyclic peptides, named internal cyclic PS5 and internal cyclic PS5 Nal1 were synthetized. The cycles, constituted by 10 amino acids, were obtained through a peptide bond between side chains of aspartic acid and lysine. New PS5 cyclic analogues were assayed for their ability to bind to JAK2 catalytic domain through SPR assay. The results

revealed that the analogue bearing the naphthyl group provided a slightly major affinity toward JAK2 with respect to linear PS5 while, the “internal cyclization” seemed to negatively interfere with recognizing ability of linear PS5 sequence since it implies a 10-fold reduction internal of affinity. As expected, the presence of a non-natural naphthylalanine in internal cyclic PS5 Nal1 reduced the proteolytic degradation level with respect to internal cyclic PS5. Cellular experiments in cytokine-stimulated VSMCs confirmed that both internal peptides are able to impair STAT1 phosphorylation and suppress the expression of JAK/STAT dependent genes, such as *Ccl2*, *Ccl5* and *Cxcl10* chemokines. In addition, cyclic and linear forms of PS5 peptide reduced superoxide anion production and *Nox1* gene expression and effectively inhibited proliferation and migration of VSMCs, without affecting cell viability. Based on these results, the potential anti-inflammatory and anti-atherosclerotic activity of PS5 peptide was investigated in ApoE KO mice fed a high-fat diet, a well-established experimental model of atherosclerosis. Interestingly, PS5 therapy caused a decrease in the lesion size and lipid content of mouse atherosclerotic plaques, and also reduced the aortic expression of pro-inflammatory and pro-oxidant genes, while increasing antioxidant enzymes. Further *in vivo* studies using cyclic peptides will be required to confirm these interesting findings.

Overall data indicate that these small sequences can be used as promising scaffolds into higher-affinity compounds and could aid the design of more efficient inhibitors of JAK2’s activity through medicinal-chemistry approaches.

VI. CONCLUSIONS

Nowadays, the need for selective anti-inflammatory treatments without (or low) undesirable side effects leads to constant research for pioneering targets that could satisfy this purpose [253]. Although small-molecule drugs still have a primary role in the pharmaceutical market, recent studies reveal that they are losing the dominance acquired in these years [254]. Recently, an improved interest in peptides and peptidomimetics as potential therapeutic agents has raised (The emergence of peptides in the pharmaceutical business: From exploration to exploitation 2014). Peptides indeed, represent compounds characterized by unique chemical-physical and therapeutic characteristics: i) low toxicity due both to their short half-life and to the fact that their degradation products are amino acids [22,21]; ii) high specificity, target affinity and potency; and iii) low cost and robust synthesis and storage. All these features make them competitive in pharmaceutical market [20]. Natural or synthetic peptides have been largely developed as potential drug candidates to disrupt PPIs and target or inhibit intracellular molecules such as receptor tyrosine kinases [255]. The concept of IPs has been validated for several PPIs, generating great expectations for their application. Actually, there are more than 20 new peptide-based clinical trials annually and more than 400 peptide drugs are under global clinical developments, with over 60 already approved for clinical use in the United States, Japan and Europe [256].

In the present thesis, rational approaches for the identification of protein interacting regions provide deeper insights into the recognition molecular mechanisms including mutated proteins associated with pathologies. In the case of SOCS family members, a protein dissection and/or the chemical modification through medicinal chemistry roles of existing lead compounds allowed us to identify new potential therapeutics and similarly, the miniaturization of functional domains paves the way to deepen mechanisms at the basis of pathologies as in the case of NPM1.

VII. COLLABORATIONS

SHG experiment was performed at Istituto Italiano di Tecnologia in collaboration with Dott.ssa Di Natale Concetta.

WAXS was performed at Institute of Crystallography (IC), National Research Council, Bariin collaboration with Dott.ssa Cinzia Giannini and Dott.ssa Teresa Sibillano.

SEM was performed at Analytical Chemistry for the Environment and CeSMA (Advanced Metrologic Service Center), University of Naples "Federico II" in collaboration with Dott.ssa Valentina Roviello and at Istituto Italiano di Tecnologia in collaboration with Dott.ssa Di Natale Concetta.

NPM1 cellular experiments were performed at Department of Translational Medicine, Federico II University of Naples in collaboration with Dott.ssa Anna Maria Malfitano and at Department of Experimental and Clinical Biomedical Sciences, Section of Biochemistry, University of Florence, in collaboration with Dott.ssa Alessandra Bigi and Dott.ssa Cristina Cecchi.

ESI experiments were performed at Istituto Italiano di Tecnologia in collaboration with Dr. PL. Scognamiglio.

NMR experiments were performed at IBB - CNR, Naples, in collaboration with Dr. M. Leone.

Cellular and *in vivo* experiments on KIRESS peptide were performed at Georgia Cancer Center, Augusta University in collaboration with Prof. H. Korkaya.

Cellular and *in vivo* experiments on SOCS1 mimetics and KIRCONG chim peptide were performed by Sara La Manna in the laboratory of Prof. Carmen Gomez Guerrero at Instituto de Investigacion Sanitaria-Fundacion Jimenez Diaz, Autonoma University of Madrid (Spain).

VIII. ABBREVIATIONS

AML: acute myeloid leukemia

ApoE KO: Apolipoprotein E knockout

ATCC: American Type Culture Collection

ATP: Adenosine 5'-triphosphate

Biotin-SA:Biotin-streptavidin

CCL: C-C motif chemokine ligand

CD:Circular Dichroism

CNS: Central Nervous System

CR: Congo Red

CTD: C-terminal Domain;

CXCL: C-X-C motif chemokine ligands

Cys(Acm):Acetaminomethyl-L-cysteine

DNMT3A: DNA (cytosine-5)-methyltransferase 3A

EAE: Experimental autoimmune encephalitis

EDTA: Ethylenediaminetetraacetic acid

EGFR: Epidermal Growth Factor Receptor

ELISA: Enzyme-Linked Immunosorbent Assay

ESS: Extended SH2 Subdomain

ETD: Everhart Thornley Detector

FBS: Fetal Bovine Serum

GST-JH1: GST-fused catalytic kinase domain

Hepes: 4-(2-hydroxyethyl)-1-piperazineethanesulfonic acid

HTS: High throughput screening

ICAM-1: Intercellular Cell Adhesion Molecule-1

IDH1: Isocitrate Dehydrogenase 1

IDR: Intrinsically disordered regions

IL: Interleukin

INFγ: Interferon gamma

IP: Image Plate

ITC: Isothermal Titration Calorimetry

JAK: Janus Kinases

KIR: Kinase Inhibitory Region

LC-MS: Liquid Chromatography Mass Spectrometry

LPS: Lipopolysaccharide

MHC: Major Histocompatibility Complex

MTS: Medium throughput screening

MTT: 3-(4,5-dimethylthiazol-2-yl)-2,5-diphenyltetrazolium bromide.

Nal: Naphtyl

NC: Negative Control

NES: Nuclear Export Signal

NMR: Nuclear Magnetic Resonance

NOESY: Nuclear Overhauser Enhancement Spectroscopy

NoLS: Nucleolar Localization Signal

NPM1: Nucleophosmin 1

PCR: Polymerase Chain Reaction

PDGF: Platelet-Derived Growth Factor

RANKL: Receptor Activator of Nuclear Factor-kB Ligand

ROESY:Rotating Frame Overhauser Enhancement Spectroscopy

SH2: Src Homology 2

SOCS: Suppressors Of Cytokine Signaling

SPPS: Solid-Phase Peptide Synthesis

SPR: Surface Plasmon Resonance

SSI-1: STAT-induced STAT inhibitor 1

STAT: Signal Transducer and Activator of Transcription

TAMRA: Tetramethylrhodamine

TCA: Trichloroacetic acid

TCEP: tris (2-carbossietyl) phoshin

TGF: Transforming Growth Factor

ThT: Thioflavin T

TLD: Through the Lens Detector

TNBC: Triple-Negative Breast Cancer

TNF-α: Tumor Necrosis Factor

TOCSY:Total Correlation Spectroscopy

VSMCs: Vascular smooth muscle cells

WAXS: Wide-Angle X-ray Scattering;SEM: Scanning electron microscopy

IX. REFERENCES

1. Kuzmanov, U.; Emili, A., Protein-protein interaction networks: probing disease mechanisms using model systems. *Genome Med* **2013,** *5* (4), 37.
2. Zinzalla, G.; Thurston, D. E., Targeting protein-protein interactions for therapeutic intervention: a challenge for the future. *Future Med Chem* **2009,** *1* (1), 65-93.
3. Rao, V. S.; Srinivas, K.; Sujini, G. N.; Kumar, G. N., Protein-protein interaction detection: methods and analysis. *Int J Proteomics* **2014,** *2014*, 147648.
4. Kim, W. K.; Henschel, A.; Winter, C.; Schroeder, M., The many faces of protein-protein interactions: A compendium of interface geometry. *PLoS Comput Biol* **2006,** *2* (9), e124.
5. Nooren, I. M.; Thornton, J. M., Diversity of protein-protein interactions. *EMBO J* **2003,** *22* (14), 3486-92.
6. Fischer, G.; Rossmann, M.; Hyvonen, M., Alternative modulation of protein-protein interactions by small molecules. *Curr Opin Biotechnol* **2015,** *35*, 78-85.
7. Berggard, T.; Linse, S.; James, P., Methods for the detection and analysis of protein-protein interactions. *Proteomics* **2007,** *7* (16), 2833-42.
8. Sabetian, S.; Shamsir, M. S., Computer aided analysis of disease linked protein networks. *Bioinformation* **2019,** *15* (7), 513-522.
9. Stumpf, M. P.; Thorne, T.; de Silva, E.; Stewart, R.; An, H. J.; Lappe, M.; Wiuf, C., Estimating the size of the human interactome. *Proc Natl Acad Sci U S A* **2008,** *105* (19), 6959-64.
10. Zhang, Q. C.; Petrey, D.; Deng, L.; Qiang, L.; Shi, Y.; Thu, C. A.; Bisikirska, B.; Lefebvre, C.; Accili, D.; Hunter, T.; Maniatis, T.; Califano, A.; Honig, B., Structure-based prediction of protein-protein interactions on a genome-wide scale. *Nature* **2012,** *490* (7421), 556-60.
11. Modell, A. E.; Blosser, S. L.; Arora, P. S., Systematic Targeting of Protein-Protein Interactions. *Trends Pharmacol Sci* **2016,** *37* (8), 702-713.
12. Lobingier, B. T.; Huttenhain, R.; Eichel, K.; Miller, K. B.; Ting, A. Y.; von Zastrow, M.; Krogan, N. J., An Approach to Spatiotemporally Resolve Protein Interaction Networks in Living Cells. *Cell* **2017,** *169* (2), 350-360 e12.
13. Petta, I.; Lievens, S.; Libert, C.; Tavernier, J.; De Bosscher, K., Modulation of Protein-Protein Interactions for the Development of Novel Therapeutics. *Mol Ther* **2016,** *24* (4), 707-18.
14. Kaspar, A. A.; Reichert, J. M., Future directions for peptide therapeutics development. *Drug Discov Today* **2013,** *18* (17-18), 807-17.
15. Mabonga, L.; Kappo, A. P., Protein-protein interaction modulators: advances, successes and remaining challenges. *Biophys Rev* **2019,** *11* (4), 559-581.
16. Zhuang, C.; Wu, Z.; Xing, C.; Miao, Z., Small molecules inhibiting Keap1-Nrf2 protein-protein interactions: a novel approach to activate Nrf2 function. *Medchemcomm* **2017,** *8* (2), 286-294.
17. Villoutreix, B. O.; Kuenemann, M. A.; Poyet, J. L.; Bruzzoni-Giovanelli, H.; Labbe, C.; Lagorce, D.; Sperandio, O.; Miteva, M. A., Drug-Like Protein-Protein Interaction Modulators: Challenges and Opportunities for Drug Discovery and Chemical Biology. *Mol Inform* **2014,** *33* (6-7), 414-437.
18. Sulochana, K. N.; Ge, R., Developing antiangiogenic peptide drugs for angiogenesis-related diseases. *Curr Pharm Des* **2007,** *13* (20), 2074-86.
19. Jain, R.; Chawrai, S., Advancements in the anti-diabetes chemotherapeutics based on amino acids, peptides, and peptidomimetics. *Mini Rev Med Chem* **2005,** *5* (5), 469-77.
20. Scognamiglio, P. L.; Di Natale, C.; Perretta, G.; Marasco, D., From peptides to small molecules: an intriguing but intricated way to new drugs. *Curr Med Chem* **2013,** *20* (31), 3803-17.
21. Vlieghe, P.; Lisowski, V.; Martinez, J.; Khrestchatisky, M., Synthetic therapeutic peptides: science and market. *Drug Discov Today* **2010,** *15* (1-2), 40-56.
22. McGregor, D. P., Discovering and improving novel peptide therapeutics. *Curr Opin Pharmacol* **2008,** *8* (5), 616-9.
23. La Manna, S.; Di Natale, C.; Florio, D.; Marasco, D., Peptides as Therapeutic Agents for Inflammatory-Related Diseases. *Int J Mol Sci* **2018,** *19* (9).

24. Scognamiglio, P. L.; Morelli, G.; Marasco, D., Synthetic and structural routes for the rational conversion of peptides into small molecules. *Methods Mol Biol* **2015,** *1268*, 159-93.
25. Cerrato, C. P.; Kunnapuu, K.; Langel, U., Cell-penetrating peptides with intracellular organelle targeting. *Expert Opin Drug Deliv* **2017,** *14* (2), 245-255.
26. Frank, R., The SPOT-synthesis technique. Synthetic peptide arrays on membrane supports--principles and applications. *J Immunol Methods* **2002,** *267* (1), 13-26.
27. Causa, F.; Della Moglie, R.; Iaccino, E.; Mimmi, S.; Marasco, D.; Scognamiglio, P. L.; Battista, E.; Palmieri, C.; Cosenza, C.; Sanguigno, L.; Quinto, I.; Scala, G.; Netti, P. A., Evolutionary screening and adsorption behavior of engineered M13 bacteriophage and derived dodecapeptide for selective decoration of gold interfaces. *J Colloid Interface Sci* **2013,** *389* (1), 220-9.
28. Cohen, J. C.; Killeen, E.; Chander, A.; Takemaru, K.; Larson, J. E.; Treharne, K. J.; Mehta, A., Small interfering peptide (siP) for in vivo examination of the developing lung interactonome. *Dev Dyn* **2009,** *238* (2), 386-93.
29. Starzec, A.; Vassy, R.; Martin, A.; Lecouvey, M.; Di Benedetto, M.; Crepin, M.; Perret, G. Y., Antiangiogenic and antitumor activities of peptide inhibiting the vascular endothelial growth factor binding to neuropilin-1. *Life Sci* **2006,** *79* (25), 2370-81.
30. Yu, J.; Vavrusa, M.; Andreani, J.; Rey, J.; Tuffery, P.; Guerois, R., InterEvDock: a docking server to predict the structure of protein-protein interactions using evolutionary information. *Nucleic Acids Res* **2016,** *44* (W1), W542-9.
31. Nevola, L.; Giralt, E., Modulating protein-protein interactions: the potential of peptides. *Chem Commun (Camb)* **2015,** *51* (16), 3302-15.
32. Qvit, N.; Kornfeld, O. S., Development of a Backbone Cyclic Peptide Library as Potential Antiparasitic Therapeutics Using Microwave Irradiation. *J Vis Exp* **2016,** (107), e53589.
33. Eustache, S.; Leprince, J.; Tuffery, P., Progress with peptide scanning to study structure-activity relationships: the implications for drug discovery. *Expert Opin Drug Discov* **2016,** *11* (8), 771-84.
34. Arrouss, I.; Nemati, F.; Roncal, F.; Wislez, M.; Dorgham, K.; Vallerand, D.; Rabbe, N.; Karboul, N.; Carlotti, F.; Bravo, J.; Mazier, D.; Decaudin, D.; Rebollo, A., Specific targeting of caspase-9/PP2A interaction as potential new anti-cancer therapy. *PLoS One* **2013,** *8* (4), e60816.
35. Baar, M. P.; Brandt, R. M. C.; Putavet, D. A.; Klein, J. D. D.; Derks, K. W. J.; Bourgeois, B. R. M.; Stryeck, S.; Rijksen, Y.; van Willigenburg, H.; Feijtel, D. A.; van der Pluijm, I.; Essers, J.; van Cappellen, W. A.; van, I. W. F.; Houtsmuller, A. B.; Pothof, J.; de Bruin, R. W. F.; Madl, T.; Hoeijmakers, J. H. J.; Campisi, J.; de Keizer, P. L. J., Targeted Apoptosis of Senescent Cells Restores Tissue Homeostasis in Response to Chemotoxicity and Aging. *Cell* **2017,** *169* (1), 132-147 e16.
36. Macalino, S. J. Y.; Basith, S.; Clavio, N. A. B.; Chang, H.; Kang, S.; Choi, S., Evolution of In Silico Strategies for Protein-Protein Interaction Drug Discovery. *Molecules* **2018,** *23* (8).
37. Kang, Y. J.; Olson, M. O.; Jones, C.; Busch, H., Nucleolar phosphoproteins of normal rat liver and Novikoff hepatoma ascites cells. *Cancer Res* **1975,** *35* (6), 1470-5.
38. Okuwaki, M.; Matsumoto, K.; Tsujimoto, M.; Nagata, K., Function of nucleophosmin/B23, a nucleolar acidic protein, as a histone chaperone. *FEBS Lett* **2001,** *506* (3), 272-6.
39. Lindstrom, M. S., NPM1/B23: A Multifunctional Chaperone in Ribosome Biogenesis and Chromatin Remodeling. *Biochem Res Int* **2011,** *2011*, 195209.
40. Anensen, N.; Hjelle, S. M.; Van Belle, W.; Haaland, I.; Silden, E.; Bourdon, J. C.; Hovland, R.; Tasken, K.; Knappskog, S.; Lonning, P. E.; Bruserud, O.; Gjertsen, B. T., Correlation analysis of p53 protein isoforms with NPM1/FLT3 mutations and therapy response in acute myeloid leukemia. *Oncogene* **2012,** *31* (12), 1533-45.
41. Mitrea, D. M.; Kriwacki, R. W., On the relationship status for Arf and NPM1 - it's complicated. *FEBS J* **2018,** *285* (5), 828-831.
42. Namboodiri, V. M.; Akey, I. V.; Schmidt-Zachmann, M. S.; Head, J. F.; Akey, C. W., The structure and function of Xenopus NO38-core, a histone chaperone in the nucleolus. *Structure* **2004,** *12* (12), 2149-60.
43. Okuwaki, M., The structure and functions of NPM1/Nucleophsmin/B23, a multifunctional nucleolar acidic protein. *J Biochem* **2008,** *143* (4), 441-8.

44. Gallo, A.; Lo Sterzo, C.; Mori, M.; Di Matteo, A.; Bertini, I.; Banci, L.; Brunori, M.; Federici, L., Structure of nucleophosmin DNA-binding domain and analysis of its complex with a G-quadruplex sequence from the c-MYC promoter. *J Biol Chem* **2012,** *287* (32), 26539-48.
45. Federici, L.; Falini, B., Nucleophosmin mutations in acute myeloid leukemia: a tale of protein unfolding and mislocalization. *Protein Sci* **2013,** *22* (5), 545-56.
46. Wang, W.; Budhu, A.; Forgues, M.; Wang, X. W., Temporal and spatial control of nucleophosmin by the Ran-Crm1 complex in centrosome duplication. *Nat Cell Biol* **2005,** *7* (8), 823-30.
47. Falini, B.; Bolli, N.; Liso, A.; Martelli, M. P.; Mannucci, R.; Pileri, S.; Nicoletti, I., Altered nucleophosmin transport in acute myeloid leukaemia with mutated NPM1: molecular basis and clinical implications. *Leukemia* **2009,** *23* (10), 1731-43.
48. Hingorani, K.; Szebeni, A.; Olson, M. O., Mapping the functional domains of nucleolar protein B23. *J Biol Chem* **2000,** *275* (32), 24451-7.
49. Heath, E. M.; Chan, S. M.; Minden, M. D.; Murphy, T.; Shlush, L. I.; Schimmer, A. D., Biological and clinical consequences of NPM1 mutations in AML. *Leukemia* **2017,** *31* (4), 798-807.
50. Mitrea, D. M.; Kriwacki, R. W., Phase separation in biology; functional organization of a higher order. *Cell Commun Signal* **2016,** *14*, 1.
51. Mitrea, D. M.; Cika, J. A.; Guy, C. S.; Ban, D.; Banerjee, P. R.; Stanley, C. B.; Nourse, A.; Deniz, A. A.; Kriwacki, R. W., Nucleophosmin integrates within the nucleolus via multi-modal interactions with proteins displaying R-rich linear motifs and rRNA. *Elife* **2016,** *5*.
52. Mitrea, D. M.; Cika, J. A.; Stanley, C. B.; Nourse, A.; Onuchic, P. L.; Banerjee, P. R.; Phillips, A. H.; Park, C. G.; Deniz, A. A.; Kriwacki, R. W., Self-interaction of NPM1 modulates multiple mechanisms of liquid-liquid phase separation. *Nat Commun* **2018,** *9* (1), 842.
53. Grummitt, C. G.; Townsley, F. M.; Johnson, C. M.; Warren, A. J.; Bycroft, M., Structural consequences of nucleophosmin mutations in acute myeloid leukemia. *J Biol Chem* **2008,** *283* (34), 23326-32.
54. Falini, B.; Nicoletti, I.; Martelli, M. F.; Mecucci, C., Acute myeloid leukemia carrying cytoplasmic/mutated nucleophosmin (NPMc+ AML): biologic and clinical features. *Blood* **2007,** *109* (3), 874-85.
55. Emmott, E.; Hiscox, J. A., Nucleolar targeting: the hub of the matter. *EMBO Rep* **2009,** *10* (3), 231-8.
56. Nishimura, Y.; Ohkubo, T.; Furuichi, Y.; Umekawa, H., Tryptophans 286 and 288 in the C-terminal region of protein B23.1 are important for its nucleolar localization. *Biosci Biotechnol Biochem* **2002,** *66* (10), 2239-42.
57. Okuwaki, M.; Iwamatsu, A.; Tsujimoto, M.; Nagata, K., Identification of nucleophosmin/B23, an acidic nucleolar protein, as a stimulatory factor for in vitro replication of adenovirus DNA complexed with viral basic core proteins. *J Mol Biol* **2001,** *311* (1), 41-55.
58. Maggi, L. B., Jr.; Kuchenruether, M.; Dadey, D. Y.; Schwope, R. M.; Grisendi, S.; Townsend, R. R.; Pandolfi, P. P.; Weber, J. D., Nucleophosmin serves as a rate-limiting nuclear export chaperone for the Mammalian ribosome. *Mol Cell Biol* **2008,** *28* (23), 7050-65.
59. Colombo, E.; Alcalay, M.; Pelicci, P. G., Nucleophosmin and its complex network: a possible therapeutic target in hematological diseases. *Oncogene* **2011,** *30* (23), 2595-609.
60. Grisendi, S.; Mecucci, C.; Falini, B.; Pandolfi, P. P., Nucleophosmin and cancer. *Nature reviews. Cancer* **2006,** *6* (7), 493-505.
61. Balusu, R.; Fiskus, W.; Rao, R.; Chong, D. G.; Nalluri, S.; Mudunuru, U.; Ma, H.; Chen, L.; Venkannagari, S.; Ha, K.; Abhyankar, S.; Williams, C.; McGuirk, J.; Khoury, H. J.; Ustun, C.; Bhalla, K. N., Targeting levels or oligomerization of nucleophosmin 1 induces differentiation and loss of survival of human AML cells with mutant NPM1. *Blood* **2011,** *118* (11), 3096-106.
62. Falini, B.; Martelli, M. P.; Bolli, N.; Bonasso, R.; Ghia, E.; Pallotta, M. T.; Diverio, D.; Nicoletti, I.; Pacini, R.; Tabarrini, A.; Galletti, B. V.; Mannucci, R.; Roti, G.; Rosati, R.; Specchia, G.; Liso, A.; Tiacci, E.; Alcalay, M.; Luzi, L.; Volorio, S.; Bernard, L.; Guarini, A.; Amadori, S.; Mandelli, F.; Pane, F.; Lo-Coco, F.; Saglio, G.; Pelicci, P. G.; Martelli, M. F.; Mecucci, C., Immunohistochemistry predicts nucleophosmin (NPM) mutations in acute myeloid leukemia. *Blood* **2006,** *108* (6), 1999-2005.

63. Falini, B.; Mecucci, C.; Tiacci, E.; Alcalay, M.; Rosati, R.; Pasqualucci, L.; La Starza, R.; Diverio, D.; Colombo, E.; Santucci, A.; Bigerna, B.; Pacini, R.; Pucciarini, A.; Liso, A.; Vignetti, M.; Fazi, P.; Meani, N.; Pettirossi, V.; Saglio, G.; Mandelli, F.; Lo-Coco, F.; Pelicci, P. G.; Martelli, M. F.; Party, G. A. L. W., Cytoplasmic nucleophosmin in acute myelogenous leukemia with a normal karyotype. *N Engl J Med* **2005,** *352* (3), 254-66.
64. Okuwaki, M.; Sumi, A.; Hisaoka, M.; Saotome-Nakamura, A.; Akashi, S.; Nishimura, Y.; Nagata, K., Function of homo- and hetero-oligomers of human nucleoplasmin/nucleophosmin family proteins NPM1, NPM2 and NPM3 during sperm chromatin remodeling. *Nucleic Acids Res* **2012,** *40* (11), 4861-78.
65. Di Matteo, A.; Franceschini, M.; Chiarella, S.; Rocchio, S.; Travaglini-Allocatelli, C.; Federici, L., Molecules that target nucleophosmin for cancer treatment: an update. *Oncotarget* **2016,** *7* (28), 44821-44840.
66. Scaloni, F.; Gianni, S.; Federici, L.; Falini, B.; Brunori, M., Folding mechanism of the C-terminal domain of nucleophosmin: residual structure in the denatured state and its pathophysiological significance. *FASEB J* **2009,** *23* (8), 2360-5.
67. Seif, F.; Khoshmirsafa, M.; Aazami, H.; Mohsenzadegan, M.; Sedighi, G.; Bahar, M., The role of JAK-STAT signaling pathway and its regulators in the fate of T helper cells. *Cell Commun Signal* **2017,** *15* (1), 23.
68. Kiu, H.; Nicholson, S. E., Biology and significance of the JAK/STAT signalling pathways. *Growth Factors* **2012,** *30* (2), 88-106.
69. Hebenstreit, D.; Horejs-Hoeck, J.; Duschl, A., JAK/STAT-dependent gene regulation by cytokines. *Drug News Perspect* **2005,** *18* (4), 243-9.
70. Lim, C. P.; Cao, X., Structure, function, and regulation of STAT proteins. *Mol Biosyst* **2006,** *2* (11), 536-50.
71. Baker, S. J.; Rane, S. G.; Reddy, E. P., Hematopoietic cytokine receptor signaling. *Oncogene* **2007,** *26* (47), 6724-37.
72. Yamaoka, K.; Saharinen, P.; Pesu, M.; Holt, V. E., 3rd; Silvennoinen, O.; O'Shea, J. J., The Janus kinases (Jaks). *Genome Biol* **2004,** *5* (12), 253.
73. Springuel, L.; Renauld, J. C.; Knoops, L., JAK kinase targeting in hematologic malignancies: a sinuous pathway from identification of genetic alterations towards clinical indications. *Haematologica* **2015,** *100* (10), 1240-53.
74. Haan, C.; Is'harc, H.; Hermanns, H. M.; Schmitz-Van De Leur, H.; Kerr, I. M.; Heinrich, P. C.; Grotzinger, J.; Behrmann, I., Mapping of a region within the N terminus of Jak1 involved in cytokine receptor interaction. *J Biol Chem* **2001,** *276* (40), 37451-8.
75. Saharinen, P.; Takaluoma, K.; Silvennoinen, O., Regulation of the Jak2 tyrosine kinase by its pseudokinase domain. *Mol Cell Biol* **2000,** *20* (10), 3387-95.
76. Ungureanu, D.; Wu, J.; Pekkala, T.; Niranjan, Y.; Young, C.; Jensen, O. N.; Xu, C. F.; Neubert, T. A.; Skoda, R. C.; Hubbard, S. R.; Silvennoinen, O., The pseudokinase domain of JAK2 is a dual-specificity protein kinase that negatively regulates cytokine signaling. *Nat Struct Mol Biol* **2011,** *18* (9), 971-6.
77. Baxter, E. J.; Scott, L. M.; Campbell, P. J.; East, C.; Fourouclas, N.; Swanton, S.; Vassiliou, G. S.; Bench, A. J.; Boyd, E. M.; Curtin, N.; Scott, M. A.; Erber, W. N.; Green, A. R.; Cancer Genome, P., Acquired mutation of the tyrosine kinase JAK2 in human myeloproliferative disorders. *Lancet* **2005,** *365* (9464), 1054-61.
78. James, C.; Ugo, V.; Le Couedic, J. P.; Staerk, J.; Delhommeau, F.; Lacout, C.; Garcon, L.; Raslova, H.; Berger, R.; Bennaceur-Griscelli, A.; Villeval, J. L.; Constantinescu, S. N.; Casadevall, N.; Vainchenker, W., A unique clonal JAK2 mutation leading to constitutive signalling causes polycythaemia vera. *Nature* **2005,** *434* (7037), 1144-8.
79. Kralovics, R.; Passamonti, F.; Buser, A. S.; Teo, S. S.; Tiedt, R.; Passweg, J. R.; Tichelli, A.; Cazzola, M.; Skoda, R. C., A gain-of-function mutation of JAK2 in myeloproliferative disorders. *N Engl J Med* **2005,** *352* (17), 1779-90.
80. Sanz Sanz, A.; Niranjan, Y.; Hammaren, H.; Ungureanu, D.; Ruijtenbeek, R.; Touw, I. P.; Silvennoinen, O.; Hilhorst, R., The JH2 domain and SH2-JH2 linker regulate JAK2 activity: A detailed kinetic analysis of wild type and V617F mutant kinase domains. *Biochim Biophys Acta* **2014,** *1844* (10), 1835-41.

81. Spivak, J. L.; Barosi, G.; Tognoni, G.; Barbui, T.; Finazzi, G.; Marchioli, R.; Marchetti, M., Chronic myeloproliferative disorders. *Hematology Am Soc Hematol Educ Program* **2003**, 200-24.
82. Rauch, I.; Muller, M.; Decker, T., The regulation of inflammation by interferons and their STATs. *JAKSTAT* **2013,** *2* (1), e23820.
83. Herrington, J.; Smit, L. S.; Schwartz, J.; Carter-Su, C., The role of STAT proteins in growth hormone signaling. *Oncogene* **2000,** *19* (21), 2585-97.
84. Yan, Z.; Gibson, S. A.; Buckley, J. A.; Qin, H.; Benveniste, E. N., Role of the JAK/STAT signaling pathway in regulation of innate immunity in neuroinflammatory diseases. *Clin Immunol* **2018,** *189*, 4-13.
85. Kazi, J. U.; Kabir, N. N.; Flores-Morales, A.; Ronnstrand, L., SOCS proteins in regulation of receptor tyrosine kinase signaling. *Cell Mol Life Sci* **2014,** *71* (17), 3297-310.
86. Cooney, R. N., Suppressors of cytokine signaling (SOCS): inhibitors of the JAK/STAT pathway. *Shock* **2002,** *17* (2), 83-90.
87. Kario, E.; Marmor, M. D.; Adamsky, K.; Citri, A.; Amit, I.; Amariglio, N.; Rechavi, G.; Yarden, Y., Suppressors of cytokine signaling 4 and 5 regulate epidermal growth factor receptor signaling. *J Biol Chem* **2005,** *280* (8), 7038-48.
88. Banks, A. S.; Li, J.; McKeag, L.; Hribal, M. L.; Kashiwada, M.; Accili, D.; Rothman, P. B., Deletion of SOCS7 leads to enhanced insulin action and enlarged islets of Langerhans. *J Clin Invest* **2005,** *115* (9), 2462-71.
89. Trengove, M. C.; Ward, A. C., SOCS proteins in development and disease. *Am J Clin Exp Immunol* **2013,** *2* (1), 1-29.
90. Yin, Y.; Liu, W.; Dai, Y., SOCS3 and its role in associated diseases. *Hum Immunol* **2015,** *76* (10), 775-80.
91. O'Sullivan, L. A.; Noor, S. M.; Trengove, M. C.; Lewis, R. S.; Liongue, C.; Sprigg, N. S.; Nicholson, S. E.; Ward, A. C., Suppressor of cytokine signaling 1 regulates embryonic myelopoiesis independently of its effects on T cell development. *J Immunol* **2011,** *186* (8), 4751-61.
92. Galic, S.; Sachithanandan, N.; Kay, T. W.; Steinberg, G. R., Suppressor of cytokine signalling (SOCS) proteins as guardians of inflammatory responses critical for regulating insulin sensitivity. *Biochem J* **2014,** *461* (2), 177-88.
93. Yoshimura, A.; Suzuki, M.; Sakaguchi, R.; Hanada, T.; Yasukawa, H., SOCS, Inflammation, and Autoimmunity. *Front Immunol* **2012,** *3*, 20.
94. Yoshimura, A.; Yasukawa, H., JAK's SOCS: a mechanism of inhibition. *Immunity* **2012,** *36* (2), 157-9.
95. Babon, J. J.; Nicola, N. A., The biology and mechanism of action of suppressor of cytokine signaling 3. *Growth Factors* **2012,** *30* (4), 207-19.
96. Flowers, L. O.; Subramaniam, P. S.; Johnson, H. M., A SOCS-1 peptide mimetic inhibits both constitutive and IL-6 induced activation of STAT3 in prostate cancer cells. *Oncogene* **2005,** *24* (12), 2114-20.
97. Flowers, L. O.; Johnson, H. M.; Mujtaba, M. G.; Ellis, M. R.; Haider, S. M.; Subramaniam, P. S., Characterization of a peptide inhibitor of Janus kinase 2 that mimics suppressor of cytokine signaling 1 function. *J Immunol* **2004,** *172* (12), 7510-8.
98. Waiboci, L. W.; Ahmed, C. M.; Mujtaba, M. G.; Flowers, L. O.; Martin, J. P.; Haider, M. I.; Johnson, H. M., Both the suppressor of cytokine signaling 1 (SOCS-1) kinase inhibitory region and SOCS-1 mimetic bind to JAK2 autophosphorylation site: implications for the development of a SOCS-1 antagonist. *J Immunol* **2007,** *178* (8), 5058-68.
99. Liau, N. P. D.; Laktyushin, A.; Lucet, I. S.; Murphy, J. M.; Yao, S.; Whitlock, E.; Callaghan, K.; Nicola, N. A.; Kershaw, N. J.; Babon, J. J., The molecular basis of JAK/STAT inhibition by SOCS1. *Nat Commun* **2018,** *9* (1), 1558.
100. Kershaw, N. J.; Murphy, J. M.; Liau, N. P.; Varghese, L. N.; Laktyushin, A.; Whitlock, E. L.; Lucet, I. S.; Nicola, N. A.; Babon, J. J., SOCS3 binds specific receptor-JAK complexes to control cytokine signaling by direct kinase inhibition. *Nat Struct Mol Biol* **2013,** *20* (4), 469-76.
101. Malemud, C. J., The role of the JAK/STAT signal pathway in rheumatoid arthritis. *Ther Adv Musculoskelet Dis* **2018,** *10* (5-6), 117-127.
102. Howell, M. D.; Kuo, F. I.; Smith, P. A., Targeting the Janus Kinase Family in Autoimmune Skin Diseases. *Front Immunol* **2019,** *10*, 2342.

103. Benveniste, E. N.; Liu, Y.; McFarland, B. C.; Qin, H., Involvement of the janus kinase/signal transducer and activator of transcription signaling pathway in multiple sclerosis and the animal model of experimental autoimmune encephalomyelitis. *J Interferon Cytokine Res* **2014,** *34* (8), 577-88.
104. Herrington, W.; Lacey, B.; Sherliker, P.; Armitage, J.; Lewington, S., Epidemiology of Atherosclerosis and the Potential to Reduce the Global Burden of Atherothrombotic Disease. *Circ Res* **2016,** *118* (4), 535-46.
105. Marrero, M. B., Introduction to JAK/STAT signaling and the vasculature. *Vascul Pharmacol* **2005,** *43* (5), 307-9.
106. Tamiya, T.; Kashiwagi, I.; Takahashi, R.; Yasukawa, H.; Yoshimura, A., Suppressors of cytokine signaling (SOCS) proteins and JAK/STAT pathways: regulation of T-cell inflammation by SOCS1 and SOCS3. *Arterioscler Thromb Vasc Biol* **2011,** *31* (5), 980-5.
107. Ortiz-Munoz, G.; Lopez-Parra, V.; Lopez-Franco, O.; Fernandez-Vizarra, P.; Mallavia, B.; Flores, C.; Sanz, A.; Blanco, J.; Mezzano, S.; Ortiz, A.; Egido, J.; Gomez-Guerrero, C., Suppressors of cytokine signaling abrogate diabetic nephropathy. *Journal of the American Society of Nephrology : JASN* **2010,** *21* (5), 763-72.
108. Sun, Y.; Ju, M.; Lin, Z.; Fredrick, T. W.; Evans, L. P.; Tian, K. T.; Saba, N. J.; Morss, P. C.; Pu, W. T.; Chen, J.; Stahl, A.; Joyal, J. S.; Smith, L. E., SOCS3 in retinal neurons and glial cells suppresses VEGF signaling to prevent pathological neovascular growth. *Science signaling* **2015,** *8* (395), ra94.
109. Ortiz-Munoz, G.; Martin-Ventura, J. L.; Hernandez-Vargas, P.; Mallavia, B.; Lopez-Parra, V.; Lopez-Franco, O.; Munoz-Garcia, B.; Fernandez-Vizarra, P.; Ortega, L.; Egido, J.; Gomez-Guerrero, C., Suppressors of cytokine signaling modulate JAK/STAT-mediated cell responses during atherosclerosis. *Arterioscler Thromb Vasc Biol* **2009,** *29* (4), 525-31.
110. Boengler, K.; Hilfiker-Kleiner, D.; Drexler, H.; Heusch, G.; Schulz, R., The myocardial JAK/STAT pathway: from protection to failure. *Pharmacol Ther* **2008,** *120* (2), 172-85.
111. Gharavi, N. M.; Alva, J. A.; Mouillesseaux, K. P.; Lai, C.; Yeh, M.; Yeung, W.; Johnson, J.; Szeto, W. L.; Hong, L.; Fishbein, M.; Wei, L.; Pfeffer, L. M.; Berliner, J. A., Role of the Jak/STAT pathway in the regulation of interleukin-8 transcription by oxidized phospholipids in vitro and in atherosclerosis in vivo. *J Biol Chem* **2007,** *282* (43), 31460-8.
112. Lim, W. S.; Timmins, J. M.; Seimon, T. A.; Sadler, A.; Kolodgie, F. D.; Virmani, R.; Tabas, I., Signal transducer and activator of transcription-1 is critical for apoptosis in macrophages subjected to endoplasmic reticulum stress in vitro and in advanced atherosclerotic lesions in vivo. *Circulation* **2008,** *117* (7), 940-51.
113. Qin, L.; Huang, Q.; Zhang, H.; Liu, R.; Tellides, G.; Min, W.; Yu, L., SOCS1 prevents graft arteriosclerosis by preserving endothelial cell function. *J Am Coll Cardiol* **2014,** *63* (1), 21-9.
114. Taleb, S.; Romain, M.; Ramkhelawon, B.; Uyttenhove, C.; Pasterkamp, G.; Herbin, O.; Esposito, B.; Perez, N.; Yasukawa, H.; Van Snick, J.; Yoshimura, A.; Tedgui, A.; Mallat, Z., Loss of SOCS3 expression in T cells reveals a regulatory role for interleukin-17 in atherosclerosis. *J Exp Med* **2009,** *206* (10), 2067-77.
115. De Vos, J.; Jourdan, M.; Tarte, K.; Jasmin, C.; Klein, B., JAK2 tyrosine kinase inhibitor tyrphostin AG490 downregulates the mitogen-activated protein kinase (MAPK) and signal transducer and activator of transcription (STAT) pathways and induces apoptosis in myeloma cells. *Br J Haematol* **2000,** *109* (4), 823-8.
116. Frank, D. A.; Mahajan, S.; Ritz, J., Fludarabine-induced immunosuppression is associated with inhibition of STAT1 signaling. *Nat Med* **1999,** *5* (4), 444-7.
117. Amit-Vazina, M.; Shishodia, S.; Harris, D.; Van, Q.; Wang, M.; Weber, D.; Alexanian, R.; Talpaz, M.; Aggarwal, B. B.; Estrov, Z., Atiprimod blocks STAT3 phosphorylation and induces apoptosis in multiple myeloma cells. *Br J Cancer* **2005,** *93* (1), 70-80.
118. White, G. E.; Cotterill, A.; Addley, M. R.; Soilleux, E. J.; Greaves, D. R., Suppressor of cytokine signalling protein SOCS3 expression is increased at sites of acute and chronic inflammation. *J Mol Histol* **2011,** *42* (2), 137-51.
119. Sikorski, K.; Czerwoniec, A.; Bujnicki, J. M.; Wesoly, J.; Bluyssen, H. A., STAT1 as a novel therapeutical target in pro-atherogenic signal integration of IFNgamma, TLR4 and IL-6 in vascular disease. *Cytokine Growth Factor Rev* **2011,** *22* (4), 211-9.
120. Chen, Q.; Lv, J.; Yang, W.; Xu, B.; Wang, Z.; Yu, Z.; Wu, J.; Yang, Y.; Han, Y., Targeted inhibition of STAT3 as a potential treatment strategy for atherosclerosis. *Theranostics* **2019,** *9* (22), 6424-6442.

121. Vogelstein, B.; Papadopoulos, N.; Velculescu, V. E.; Zhou, S.; Diaz, L. A., Jr.; Kinzler, K. W., Cancer genome landscapes. *Science* **2013,** *339* (6127), 1546-58.
122. Beaurivage, C.; Champagne, A.; Tobelaim, W. S.; Pomerleau, V.; Menendez, A.; Saucier, C., SOCS1 in cancer: An oncogene and a tumor suppressor. *Cytokine* **2016,** *82*, 87-94.
123. Huang, F. J.; Steeg, P. S.; Price, J. E.; Chiu, W. T.; Chou, P. C.; Xie, K.; Sawaya, R.; Huang, S., Molecular basis for the critical role of suppressor of cytokine signaling-1 in melanoma brain metastasis. *Cancer Res* **2008,** *68* (23), 9634-42.
124. Liu, L.; Li, W.; Wei, X.; Cui, Q.; Lou, W.; Wang, G.; Hu, X.; Qian, C., Potent antitumor activity of oncolytic adenovirus-mediated SOCS1 for hepatocellular carcinoma. *Gene Ther* **2013,** *20* (1), 84-92.
125. Sharma, J.; Larkin, J., 3rd, Therapeutic Implication of SOCS1 Modulation in the Treatment of Autoimmunity and Cancer. *Front Pharmacol* **2019,** *10*, 324.
126. Zhang, X. H.; Yang, L.; Liu, X. J.; Zhan, Y.; Pan, Y. X.; Wang, X. Z.; Luo, J. M., Association between methylation of tumor suppressor gene SOCS1 and acute myeloid leukemia. *Oncol Rep* **2018,** *40* (2), 1008-1016.
127. Raccurt, M.; Tam, S. P.; Lau, P.; Mertani, H. C.; Lambert, A.; Garcia-Caballero, T.; Li, H.; Brown, R. J.; McGuckin, M. A.; Morel, G.; Waters, M. J., Suppressor of cytokine signalling gene expression is elevated in breast carcinoma. *Br J Cancer* **2003,** *89* (3), 524-32.
128. Chikuma, S.; Kanamori, M.; Mise-Omata, S.; Yoshimura, A., Suppressors of cytokine signaling: Potential immune checkpoint molecules for cancer immunotherapy. *Cancer Sci* **2017,** *108* (4), 574-580.
129. Inagaki-Ohara, K.; Kondo, T.; Ito, M.; Yoshimura, A., SOCS, inflammation, and cancer. *JAKSTAT* **2013,** *2* (3), e24053.
130. Chu, Q.; Shen, D.; He, L.; Wang, H.; Liu, C.; Zhang, W., Prognostic significance of SOCS3 and its biological function in colorectal cancer. *Gene* **2017,** *627*, 114-122.
131. Ying, M.; Li, D.; Yang, L.; Wang, M.; Wang, N.; Chen, Y.; He, M.; Wang, Y., Loss of SOCS3 expression is associated with an increased risk of recurrent disease in breast carcinoma. *J Cancer Res Clin Oncol* **2010,** *136* (10), 1617-26.
132. Kim, G.; Ouzounova, M.; Quraishi, A. A.; Davis, A.; Tawakkol, N.; Clouthier, S. G.; Malik, F.; Paulson, A. K.; D'Angelo, R. C.; Korkaya, S.; Baker, T. L.; Esen, E. S.; Prat, A.; Liu, S.; Kleer, C. G.; Thomas, D. G.; Wicha, M. S.; Korkaya, H., SOCS3-mediated regulation of inflammatory cytokines in PTEN and p53 inactivated triple negative breast cancer model. *Oncogene* **2015,** *34* (6), 671-80.
133. Speth, J. M.; Bourdonnay, E.; Penke, L. R.; Mancuso, P.; Moore, B. B.; Weinberg, J. B.; Peters-Golden, M., Alveolar Epithelial Cell-Derived Prostaglandin E2 Serves as a Request Signal for Macrophage Secretion of Suppressor of Cytokine Signaling 3 during Innate Inflammation. *J Immunol* **2016,** *196* (12), 5112-20.
134. Di Natale, C.; Scognamiglio, P. L.; Cascella, R.; Cecchi, C.; Russo, A.; Leone, M.; Penco, A.; Relini, A.; Federici, L.; Di Matteo, A.; Chiti, F.; Vitagliano, L.; Marasco, D., Nucleophosmin contains amyloidogenic regions that are able to form toxic aggregates under physiological conditions. *FASEB J* **2015,** *29* (9), 3689-701.
135. Scognamiglio, P. L.; Di Natale, C.; Leone, M.; Poletto, M.; Vitagliano, L.; Tell, G.; Marasco, D., G-quadruplex DNA recognition by nucleophosmin: new insights from protein dissection. *Biochim Biophys Acta* **2014,** *1840* (6), 2050-9.
136. Russo, A.; Diaferia, C.; La Manna, S.; Giannini, C.; Sibillano, T.; Accardo, A.; Morelli, G.; Novellino, E.; Marasco, D., Insights into amyloid-like aggregation of H2 region of the C-terminal domain of nucleophosmin. *Biochim Biophys Acta Proteins Proteom* **2017,** *1865* (2), 176-185.
137. Scognamiglio, P. L.; Di Natale, C.; Leone, M.; Cascella, R.; Cecchi, C.; Lirussi, L.; Antoniali, G.; Riccardi, D.; Morelli, G.; Tell, G.; Chiti, F.; Marasco, D., Destabilisation, aggregation, toxicity and cytosolic mislocalisation of nucleophosmin regions associated with acute myeloid leukemia. *Oncotarget* **2016,** *7* (37), 59129-59143.
138. Ahmed, C. M.; Larkin, J., 3rd; Johnson, H. M., SOCS1 Mimetics and Antagonists: A Complementary Approach to Positive and Negative Regulation of Immune Function. *Front Immunol* **2015,** *6*, 183.

139. Doti, N.; Scognamiglio, P. L.; Madonna, S.; Scarponi, C.; Ruvo, M.; Perretta, G.; Albanesi, C.; Marasco, D., New mimetic peptides of the kinase-inhibitory region (KIR) of SOCS1 through focused peptide libraries. *The Biochemical journal* **2012,** *443* (1), 231-40.
140. Scognamiglio, P. L.; Doti, N.; Grieco, P.; Pedone, C.; Ruvo, M.; Marasco, D., Discovery of small peptide antagonists of PED/PEA15-D4alpha interaction from simplified combinatorial libraries. *Chem Biol Drug Des* **2011,** *77* (5), 319-27.
141. Madonna, S.; Scarponi, C.; Doti, N.; Carbone, T.; Cavani, A.; Scognamiglio, P. L.; Marasco, D.; Albanesi, C., Therapeutical potential of a peptide mimicking the SOCS1 kinase inhibitory region in skin immune responses. *European journal of immunology* **2013,** *43* (7), 1883-95.
142. Fields, G. B.; Noble, R. L., Solid phase peptide synthesis utilizing 9-fluorenylmethoxycarbonyl amino acids. *Int J Pept Protein Res* **1990,** *35* (3), 161-214.
143. Chen, S.; Wetzel, R., Solubilization and disaggregation of polyglutamine peptides. *Protein Sci* **2001,** *10* (4), 887-91.
144. Sunde, M.; Serpell, L. C.; Bartlam, M.; Fraser, P. E.; Pepys, M. B.; Blake, C. C., Common core structure of amyloid fibrils by synchrotron X-ray diffraction. *J Mol Biol* **1997,** *273* (3), 729-39.
145. Altamura, D.; Lassandro, R.; Vittoria, F. A.; De Caro, L.; Siliqi, D.; Ladisa, M.; Giannini, C., X-ray microimaging laboratory (XMI-LAB). *J Appl Crystallogr* **2012,** *45*, 869-873.
146. Sibillano, T.; De Caro, L.; Altamura, D.; Siliqi, D.; Ramella, M.; Boccafoschi, F.; Ciasca, G.; Campi, G.; Tirinato, L.; Di Fabrizio, E.; Giannini, C., An Optimized Table-Top Small-Angle X-ray Scattering Set-up for the Nanoscale Structural Analysis of Soft Matter. *Sci Rep-Uk* **2014,** *4*.
147. Di Natale, C.; Scognamiglio, P. L.; Cascella, R.; Cecchi, C.; Russo, A.; Leone, M.; Penco, A.; Relini, A.; Federici, L.; Di Matteo, A.; Chiti, F.; Vitagliano, L.; Marasco, D., Nucleophosmin contains amyloidogenic regions that are able to form toxic aggregates under physiological conditions. *FASEB journal : official publication of the Federation of American Societies for Experimental Biology* **2015**.
148. Cascella, R.; Evangelisti, E.; Bigi, A.; Becatti, M.; Fiorillo, C.; Stefani, M.; Chiti, F.; Cecchi, C., Soluble Oligomers Require a Ganglioside to Trigger Neuronal Calcium Overload. *Journal of Alzheimer's disease : JAD* **2017,** *60* (3), 923-938.
149. Griesinger, C.; Otting, G.; Wuthrich, K.; Ernst, R. R., Clean Tocsy for H-1 Spin System-Identification in Macromolecules. *J Am Chem Soc* **1988,** *110* (23), 7870-7872.
150. Kumar, A.; Ernst, R. R.; Wuthrich, K., A two-dimensional nuclear Overhauser enhancement (2D NOE) experiment for the elucidation of complete proton-proton cross-relaxation networks in biological macromolecules. *Biochem Biophys Res Commun* **1980,** *95* (1), 1-6.
151. Bax, A.; Davis, D. G., Practical Aspects of Two-Dimensional Transverse Noe Spectroscopy. *J Magn Reson* **1985,** *63* (1), 207-213.
152. Piantini, U.; Sorensen, O. W.; Ernst, R. R., Multiple quantum filters for elucidating NMR coupling networks. *J Am Chem Soc* **1982,** *104* (24), 6800-6801.
153. Hwang, T. L.; Shaka, A. J., Water Suppression That Works - Excitation Sculpting Using Arbitrary Wave-Forms and Pulsed-Field Gradients. *J Magn Reson Ser A* **1995,** *112* (2), 275-279.
154. Wuthrich, K., *NMR of proteins and nucleic acids*. Wiley: New York, 1986.
155. Herrmann, T.; Guntert, P.; Wuthrich, K., Protein NMR structure determination with automated NOE assignment using the new software CANDID and the torsion angle dynamics algorithm DYANA. *J Mol Biol* **2002,** *319* (1), 209-27.
156. Pettersen, E. F.; Goddard, T. D.; Huang, C. C.; Couch, G. S.; Greenblatt, D. M.; Meng, E. C.; Ferrin, T. E., UCSF Chimera--a visualization system for exploratory research and analysis. *J Comput Chem* **2004,** *25* (13), 1605-12.
157. Koradi, R.; Billeter, M.; Wuthrich, K., MOLMOL: a program for display and analysis of macromolecular structures. *J. Mol. Graphics* **1996,** *14* (1), 51-5, 29-32.
158. Laskowski, R. A.; Rullmannn, J. A.; MacArthur, M. W.; Kaptein, R.; Thornton, J. M., AQUA and PROCHECK-NMR: programs for checking the quality of protein structures solved by NMR. *J Biomol NMR* **1996,** *8* (4), 477-86.

159. Williams, N. K.; Bamert, R. S.; Patel, O.; Wang, C.; Walden, P. M.; Wilks, A. F.; Fantino, E.; Rossjohn, J.; Lucet, I. S., Dissecting specificity in the Janus kinases: the structures of JAK-specific inhibitors complexed to the JAK1 and JAK2 protein tyrosine kinase domains. *Journal of molecular biology* **2009,** *387* (1), 219-232.
160. Waterhouse, A.; Bertoni, M.; Bienert, S.; Studer, G.; Tauriello, G.; Gumienny, R.; Heer, F. T.; de Beer, T. A. P.; Rempfer, C.; Bordoli, L., SWISS-MODEL: homology modelling of protein structures and complexes. *Nucleic acids research* **2018,** *46* (W1), W296-W303.
161. Liau, N. P.; Laktyushin, A.; Lucet, I. S.; Murphy, J. M.; Yao, S.; Whitlock, E.; Callaghan, K.; Nicola, N. A.; Kershaw, N. J.; Babon, J. J., The molecular basis of JAK/STAT inhibition by SOCS1. *Nature communications* **2018,** *9* (1), 1558.
162. Guex, N.; Peitsch, M. C., SWISS - MODEL and the Swiss - Pdb Viewer: an environment for comparative protein modeling. *electrophoresis* **1997,** *18* (15), 2714-2723.
163. Schmid, N.; Eichenberger, A. P.; Choutko, A.; Riniker, S.; Winger, M.; Mark, A. E.; van Gunsteren, W. F., Definition and testing of the GROMOS force-field versions 54A7 and 54B7. *European biophysics journal* **2011,** *40* (7), 843.
164. Pronk, S.; Páll, S.; Schulz, R.; Larsson, P.; Bjelkmar, P.; Apostolov, R.; Shirts, M. R.; Smith, J. C.; Kasson, P. M.; van der Spoel, D., GROMACS 4.5: a high-throughput and highly parallel open source molecular simulation toolkit. *Bioinformatics* **2013,** *29* (7), 845-854.
165. Stewart, J. J. P., SPECIAL ISSUE - MOPAC - A SEMIEMPIRICAL MOLECULAR-ORBITAL PROGRAM. *Journal of Computer-Aided Molecular Design* **1990,** *4* (1), 1-45.
166. Malde, A. K.; Zuo, L.; Breeze, M.; Stroet, M.; Poger, D.; Nair, P. C.; Oostenbrink, C.; Mark, A. E., An Automated Force Field Topology Builder (ATB) and Repository: Version 1.0. *Journal of Chemical Theory and Computation* **2011,** *7* (12), 4026-4037.
167. Hess, B.; Bekker, H.; Berendsen, H. J.; Fraaije, J. G., LINCS: a linear constraint solver for molecular simulations. *Journal of Computational Chemistry* **1997,** *18* (12), 1463-1472.
168. Kumari, R.; Kumar, R.; Consortium, O. S. D. D.; Lynn, A., g_mmpbsa · A GROMACS tool for high-throughput MM-PBSA calculations. *Journal of chemical information and modeling* **2014,** *54* (7), 1951-1962.
169. Russo, A.; Diaferia, C.; La Manna, S.; Giannini, C.; Sibillano, T.; Accardo, A.; Morelli, G.; Novellino, E.; Marasco, D., Insights into amyloid-like aggregation of H2 region of the C-terminal domain of nucleophosmin. *Biochimica et biophysica acta* **2017,** *1865* (2), 176-185.
170. Tokunaga, Y.; Matsumoto, M.; Sugimoto, Y., Amyloid fibril formation from a 9 amino acid peptide, 55th-63rd residues of human lysozyme. *International journal of biological macromolecules* **2015,** *80*, 208-16.
171. Iannuzzi, C.; Borriello, M.; Portaccio, M.; Irace, G.; Sirangelo, I., Insights into Insulin Fibril Assembly at Physiological and Acidic pH and Related Amyloid Intrinsic Fluorescence. *Int J Mol Sci* **2017,** *18* (12).
172. Cohen, S. I.; Vendruscolo, M.; Dobson, C. M.; Knowles, T. P., From macroscopic measurements to microscopic mechanisms of protein aggregation. *J Mol Biol* **2012,** *421* (2-3), 160-71.
173. Cohen, S. I.; Linse, S.; Luheshi, L. M.; Hellstrand, E.; White, D. A.; Rajah, L.; Otzen, D. E.; Vendruscolo, M.; Dobson, C. M.; Knowles, T. P., Proliferation of amyloid-beta42 aggregates occurs through a secondary nucleation mechanism. *Proceedings of the National Academy of Sciences of the United States of America* **2013,** *110* (24), 9758-63.
174. Chan, F. T.; Kaminski Schierle, G. S.; Kumita, J. R.; Bertoncini, C. W.; Dobson, C. M.; Kaminski, C. F., Protein amyloids develop an intrinsic fluorescence signature during aggregation. *The Analyst* **2013,** *138* (7), 2156-62.
175. Campioni, S.; Mannini, B.; Zampagni, M.; Pensalfini, A.; Parrini, C.; Evangelisti, E.; Relini, A.; Stefani, M.; Dobson, C. M.; Cecchi, C.; Chiti, F., A causative link between the structure of aberrant protein oligomers and their toxicity. *Nature chemical biology* **2010,** *6* (2), 140-7.
176. Cardamone, M.; Puri, N. K., Spectrofluorimetric assessment of the surface hydrophobicity of proteins. *The Biochemical journal* **1992,** *282 (Pt 2)*, 589-93.
177. Semisotnov, G. V.; Rodionova, N. A.; Razgulyaev, O. I.; Uversky, V. N.; Gripas, A. F.; Gilmanshin, R. I., Study of the "molten globule" intermediate state in protein folding by a hydrophobic fluorescent probe. *Biopolymers* **1991,** *31* (1), 119-28.

178. Colby, D. W.; Zhang, Q.; Wang, S.; Groth, D.; Legname, G.; Riesner, D.; Prusiner, S. B., Prion detection by an amyloid seeding assay. *Proceedings of the National Academy of Sciences of the United States of America* **2007,** *104* (52), 20914-9.
179. Bieschke, J.; Russ, J.; Friedrich, R. P.; Ehrnhoefer, D. E.; Wobst, H.; Neugebauer, K.; Wanker, E. E., EGCG remodels mature alpha-synuclein and amyloid-beta fibrils and reduces cellular toxicity. *Proceedings of the National Academy of Sciences of the United States of America* **2010,** *107* (17), 7710-5.
180. Wang, S. H.; Dong, X. Y.; Sun, Y., Thermodynamic analysis of the molecular interactions between amyloid beta-protein fragments and (-)-epigallocatechin-3-gallate. *The journal of physical chemistry. B* **2012,** *116* (20), 5803-9.
181. Zhao, Y.; Chen, L.; Yakubov, G.; Aminiafshar, T.; Han, L.; Lian, G., Experimental and theoretical studies on the binding of epigallocatechin gallate to purified porcine gastric mucin. *The journal of physical chemistry. B* **2012,** *116* (43), 13010-6.
182. Bartolini, M.; Naldi, M.; Fiori, J.; Valle, F.; Biscarini, F.; Nicolau, D. V.; Andrisano, V., Kinetic characterization of amyloid-beta 1-42 aggregation with a multimethodological approach. *Analytical biochemistry* **2011,** *414* (2), 215-25.
183. Bernstein, S. L.; Wyttenbach, T.; Baumketner, A.; Shea, J. E.; Bitan, G.; Teplow, D. B.; Bowers, M. T., Amyloid beta-protein: Monomer structure and early aggregation states of A beta 42 and its Pro(19) alloform. *J Am Chem Soc* **2005,** *127* (7), 2075-2084.
184. Lara, C.; Gourdin-Bertin, S.; Adamcik, J.; Bolisetty, S.; Mezzenga, R., Self-assembly of ovalbumin into amyloid and non-amyloid fibrils. *Biomacromolecules* **2012,** *13* (12), 4213-21.
185. Siliqi, D.; De Caro, L.; Ladisa, M.; Scattarella, F.; Mazzone, A.; Altamura, D.; Sibillano, T.; Giannini, C., SUNBIM: a package for X-ray imaging of nano- and biomaterials using SAXS, WAXS, GISAXS and GIWAXS techniques. *J Appl Crystallogr* **2016,** *49,* 1107-1114.
186. Serpell, L. C.; Fraser, P. E.; Sunde, M., X-ray fiber diffraction of amyloid fibrils. *Methods in enzymology* **1999,** *309*, 526-36.
187. Scognamiglio, P. L.; Di Natale, C.; Leone, M.; Cascella, R.; Cecchi, C.; Lirussi, L.; Antoniali, G.; Riccardi, D.; Morelli, G.; Tell, G.; Chiti, F.; Marasco, D., Destabilisation, aggregation, toxicity and cytosolic mislocalisation of nucleophosmin regions associated with acute myeloid leukemia. *Oncotarget* **2016**.
188. Cukalevski, R.; Yang, X. T.; Meisl, G.; Weininger, U.; Bernfur, K.; Frohm, B.; Knowles, T. P. J.; Linse, S., The A beta 40 and A beta 42 peptides self-assemble into separate homomolecular fibrils in binary mixtures but cross-react during primary nucleation. *Chemical science* **2015,** *6* (7), 4215-4233.
189. Bhattacharya, A.; Bhowmik, S.; Singh, A. K.; Kodgire, P.; Das, A. K.; Mukherjee, T. K., Direct Evidence of Intrinsic Blue Fluorescence from Oligomeric Interfaces of Human Serum Albumin. *Langmuir : the ACS journal of surfaces and colloids* **2017,** *33* (40), 10606-10615.
190. Evangelisti, E.; Wright, D.; Zampagni, M.; Cascella, R.; Fiorillo, C.; Bagnoli, S.; Relini, A.; Nichino, D.; Scartabelli, T.; Nacmias, B.; Sorbi, S.; Cecchi, C., Lipid rafts mediate amyloid-induced calcium dyshomeostasis and oxidative stress in Alzheimer's disease. *Current Alzheimer research* **2013,** *10* (2), 143-53.
191. Bekard, I. B.; Dunstan, D. E., Tyrosine autofluorescence as a measure of bovine insulin fibrillation. *Biophysical journal* **2009,** *97* (9), 2521-31.
192. Chattopadhyay, A.; Haldar, S., Dynamic insight into protein structure utilizing red edge excitation shift. *Accounts of chemical research* **2014,** *47* (1), 12-9.
193. Diaferia, C.; Sibillano, T.; Balasco, N.; Giannini, C.; Roviello, V.; Vitagliano, L.; Morelli, G.; Accardo, A., Hierarchical Analysis of Self-Assembled PEGylated Hexaphenylalanine Photoluminescent Nanostructures. *Chemistry* **2016,** *22* (46), 16586-16597.
194. Johansson, P. K.; Koelsch, P., Label-free imaging of amyloids using their intrinsic linear and nonlinear optical properties. *Biomed Opt Express* **2017,** *8* (2), 743-756.
195. Schlenk, R. F.; Dohner, K.; Krauter, J.; Frohling, S.; Corbacioglu, A.; Bullinger, L.; Habdank, M.; Spath, D.; Morgan, M.; Benner, A.; Schlegelberger, B.; Heil, G.; Ganser, A.; Dohner, H., Mutations and treatment outcome in cytogenetically normal acute myeloid leukemia. *The New England journal of medicine* **2008,** *358* (18), 1909-18.

196. Motyckova, G.; Stone, R. M., The role of molecular tests in acute myelogenous leukemia treatment decisions. *Curr Hematol Malig Rep* **2010,** *5* (2), 109-17.
197. Borer, R. A.; Lehner, C. F.; Eppenberger, H. M.; Nigg, E. A., Major nucleolar proteins shuttle between nucleus and cytoplasm. *Cell* **1989,** *56* (3), 379-90.
198. Yun, J. P.; Chew, E. C.; Liew, C. T.; Chan, J. Y.; Jin, M. L.; Ding, M. X.; Fai, Y. H.; Li, H. K.; Liang, X. M.; Wu, Q. L., Nucleophosmin/B23 is a proliferate shuttle protein associated with nuclear matrix. *J Cell Biochem* **2003,** *90* (6), 1140-8.
199. Falini, B.; Martelli, M. P., NPM1-mutated AML: targeting by disassembling. *Blood* **2011,** *118* (11), 2936-8.
200. He, X.; Zhang, J., Why do hubs tend to be essential in protein networks? *PLoS Genet* **2006,** *2* (6), e88.
201. Greiner, J.; Schneider, V.; Schmitt, M.; Gotz, M.; Dohner, K.; Wiesneth, M.; Dohner, H.; Hofmann, S., Immune responses against the mutated region of cytoplasmatic NPM1 might contribute to the favorable clinical outcome of AML patients with NPM1 mutations (NPM1mut). *Blood* **2013,** *122* (6), 1087-8.
202. Greiner, J.; Ono, Y.; Hofmann, S.; Schmitt, A.; Mehring, E.; Gotz, M.; Guillaume, P.; Dohner, K.; Mytilineos, J.; Dohner, H.; Schmitt, M., Mutated regions of nucleophosmin 1 elicit both CD4(+) and CD8(+) T-cell responses in patients with acute myeloid leukemia. *Blood* **2012,** *120* (6), 1282-9.
203. Kuzelova, K.; Brodska, B.; Fuchs, O.; Dobrovolna, M.; Soukup, P.; Cetkovsky, P., Altered HLA Class I Profile Associated with Type A/D Nucleophosmin Mutation Points to Possible Anti-Nucleophosmin Immune Response in Acute Myeloid Leukemia. *PLoS One* **2015,** *10* (5), e0127637.
204. Grummitt, C. G.; Townsley, F. M.; Johnson, C. M.; Warren, A. J.; Bycroft, M., Structural consequences of nucleophosmin mutations in acute myeloid leukemia. *The Journal of biological chemistry* **2008,** *283* (34), 23326-32.
205. Gazit, E., A possible role for pi-stacking in the self-assembly of amyloid fibrils. *Faseb J* **2002,** *16* (1), 77-83.
206. Hauser, C. A.; Deng, R.; Mishra, A.; Loo, Y.; Khoe, U.; Zhuang, F.; Cheong, D. W.; Accardo, A.; Sullivan, M. B.; Riekel, C.; Ying, J. Y.; Hauser, U. A., Natural tri- to hexapeptides self-assemble in water to amyloid beta-type fiber aggregates by unexpected alpha-helical intermediate structures. *Proceedings of the National Academy of Sciences of the United States of America* **2011,** *108* (4), 1361-6.
207. Motta, A.; Reches, M.; Pappalardo, L.; Andreotti, G.; Gazit, E., The preferred conformation of the tripeptide Ala-Phe-Ala in water is an inverse gamma-turn: implications for protein folding and drug design. *Biochemistry* **2005,** *44* (43), 14170-8.
208. Babon, J. J.; Varghese, L. N.; Nicola, N. A., Inhibition of IL-6 family cytokines by SOCS3. *Semin Immunol* **2014,** *26* (1), 13-9.
209. Babon, J. J.; Kershaw, N. J.; Murphy, J. M.; Varghese, L. N.; Laktyushin, A.; Young, S. N.; Lucet, I. S.; Norton, R. S.; Nicola, N. A., Suppression of cytokine signaling by SOCS3: characterization of the mode of inhibition and the basis of its specificity. *Immunity* **2012,** *36* (2), 239-50.
210. Knighton, D. R.; Zheng, J. H.; Ten Eyck, L. F.; Ashford, V. A.; Xuong, N. H.; Taylor, S. S.; Sowadski, J. M., Crystal structure of the catalytic subunit of cyclic adenosine monophosphate-dependent protein kinase. *Science* **1991,** *253* (5018), 407-14.
211. Sasaki, A.; Yasukawa, H.; Suzuki, A.; Kamizono, S.; Syoda, T.; Kinjyo, I.; Sasaki, M.; Johnston, J. A.; Yoshimura, A., Cytokine-inducible SH2 protein-3 (CIS3/SOCS3) inhibits Janus tyrosine kinase by binding through the N-terminal kinase inhibitory region as well as SH2 domain. *Genes Cells* **1999,** *4* (6), 339-51.
212. Babon, J. J.; McManus, E. J.; Yao, S.; DeSouza, D. P.; Mielke, L. A.; Sprigg, N. S.; Willson, T. A.; Hilton, D. J.; Nicola, N. A.; Baca, M.; Nicholson, S. E.; Norton, R. S., The structure of SOCS3 reveals the basis of the extended SH2 domain function and identifies an unstructured insertion that regulates stability. *Mol Cell* **2006,** *22* (2), 205-16.
213. La Manna, S.; Scognamiglio, P. L.; Di Natale, C.; Leone, M.; Mercurio, F. A.; Malfitano, A. M.; Cianfarani, F.; Madonna, S.; Caravella, S.; Albanesi, C.; Novellino, E.; Marasco, D., Characterization of linear mimetic peptides of Interleukin-22 from dissection of protein interfaces. *Biochimie* **2017,** *138*, 106-115.

214. Babon, J. J.; Yao, S.; DeSouza, D. P.; Harrison, C. F.; Fabri, L. J.; Liepinsh, E.; Scrofani, S. D.; Baca, M.; Norton, R. S., Secondary structure assignment of mouse SOCS3 by NMR defines the domain boundaries and identifies an unstructured insertion in the SH2 domain. *FEBS J* **2005,** *272* (23), 6120-30.
215. Giordanetto, F.; Kroemer, R. T., A three-dimensional model of Suppressor Of Cytokine Signalling 1 (SOCS-1). *Protein Eng* **2003,** *16* (2), 115-24.
216. Russo, A.; Manna, S. L.; Novellino, E.; Malfitano, A. M.; Marasco, D., Molecular signaling involving intrinsically disordered proteins in prostate cancer. *Asian J Androl* **2016,** *18* (5), 673-81.
217. Kagawa, T.; Yuasa, K.; Fukunari, F.; Shiraishi, T.; Miwa, K., Quantitative evaluation of vascularity within cervical lymph nodes using Doppler ultrasound in patients with oral cancer: relation to lymph node size. *Dentomaxillofac Radiol* **2011,** *40* (7), 415-21.
218. Mankoff, D. A.; Dunnwald, L. K.; Gralow, J. R.; Ellis, G. K.; Charlop, A.; Lawton, T. J.; Schubert, E. K.; Tseng, J.; Livingston, R. B., Blood flow and metabolism in locally advanced breast cancer: relationship to response to therapy. *J Nucl Med* **2002,** *43* (4), 500-9.
219. Marqus, S.; Pirogova, E.; Piva, T. J., Evaluation of the use of therapeutic peptides for cancer treatment. *J Biomed Sci* **2017,** *24* (1), 21.
220. Croker, B. A.; Krebs, D. L.; Zhang, J. G.; Wormald, S.; Willson, T. A.; Stanley, E. G.; Robb, L.; Greenhalgh, C. J.; Forster, I.; Clausen, B. E.; Nicola, N. A.; Metcalf, D.; Hilton, D. J.; Roberts, A. W.; Alexander, W. S., SOCS3 negatively regulates IL-6 signaling in vivo. *Nat Immunol* **2003,** *4* (6), 540-5.
221. La Manna, S.; Lee, E.; Ouzounova, M.; Di Natale, C.; Novellino, E.; Merlino, A.; Korkaya, H.; Marasco, D., Mimetics of suppressor of cytokine signaling 3: Novel potential therapeutics in triple breast cancer. *International journal of cancer* **2018,** *143* (9), 2177-2186.
222. La Manna, S.; Roviello, V.; Scognamiglio, P. L.; Diaferia, C.; Giannini, C.; Sibillano, T.; Morelli, G.; Novellino, E.; Marasco, D., Amyloid fibers deriving from the aromatic core of C-terminal domain of nucleophosmin 1. *International journal of biological macromolecules* **2019,** *122*, 517-525.
223. La Manna, S.; Scognamiglio, P. L.; Roviello, V.; Borbone, F.; Florio, D.; Di Natale, C.; Bigi, A.; Cecchi, C.; Cascella, R.; Giannini, C.; Sibillano, T.; Novellino, E.; Marasco, D., The acute myeloid leukemia-associated Nucleophosmin 1 gene mutations dictate amyloidogenicity of the C-terminal domain. *The FEBS journal* **2019,** *286* (12), 2311-2328.
224. Andersson, D.; Carlsson, U.; Freskgard, P. O., Contribution of tryptophan residues to the CD spectrum of the extracellular domain of human tissue factor: application in folding studies and prediction of secondary structure. *European journal of biochemistry* **2001,** *268* (4), 1118-28.
225. Vincenzi, M.; Mercurio, F. A.; Leone, M., About TFE: Old and New Findings. *Curr Protein Pept Sci* **2019,** *20* (5), 425-451.
226. Griesinger, C.; Otting, G.; Wuthrich, K.; Ernst, R. R., Clean TOCSY for proton spin system identification in macromolecules, 110, 7870-7872. *Journal of the American Chemical Society* **1988,** *110*, 7870-7872.
227. Wuthrich, K., *NMR of Proteins and Nucleic Acids*. Wiley: New YorK, 1986; p 320.
228. Kumar, A.; Ernst, R. R.; Wuthrich, K., A two-dimensional nuclear Overhauser enhancement (2D NOE) experiment for the elucidation of complete proton-proton cross-relaxation networks in biological macromolecules. *Biochem Biophys Res Commun* **1980,** *95* (1), 1-6.
229. Koradi, R.; Billeter, M.; Wuthrich, K., MOLMOL: a program for display and analysis of macromolecular structures. *J Mol Graph* **1996,** *14* (1), 51-5, 29-32.
230. Kershaw, N. J.; Murphy, J. M.; Liau, N. P.; Varghese, L. N.; Laktyushin, A.; Whitlock, E. L.; Lucet, I. S.; Nicola, N. A.; Babon, J. J., SOCS3 binds specific receptor–JAK complexes to control cytokine signaling by direct kinase inhibition. *Nature structural & molecular biology* **2013,** *20* (4), 469.
231. Recio, C.; Lazaro, I.; Oguiza, A.; Lopez-Sanz, L.; Bernal, S.; Blanco, J.; Egido, J.; Gomez-Guerrero, C., Suppressor of Cytokine Signaling-1 Peptidomimetic Limits Progression of Diabetic Nephropathy. *Journal of the American Society of Nephrology : JASN* **2017,** *28* (2), 575-585.
232. Qin, H.; Niyongere, S. A.; Lee, S. J.; Baker, B. J.; Benveniste, E. N., Expression and functional significance of SOCS-1 and SOCS-3 in astrocytes. *Journal of immunology* **2008,** *181* (5), 3167-76.

233. Ye, S.; Lowther, S.; Stambas, J., Inhibition of reactive oxygen species production ameliorates inflammation induced by influenza A viruses via upregulation of SOCS1 and SOCS3. *Journal of virology* **2015,** *89* (5), 2672-83.
234. Babon, J. J., Quantitative analysis of JAK binding using isothermal titration calorimetry and surface plasmon resonance. *Methods in molecular biology* **2013,** *967*, 57-67.
235. Madonna, S.; Scarponi, C.; Morelli, M.; Sestito, R.; Scognamiglio, P. L.; Marasco, D.; Albanesi, C., SOCS3 inhibits the pathological effects of IL-22 in non-melanoma skin tumor-derived keratinocytes. *Oncotarget* **2017,** *8* (15), 24652-24667.
236. Yasukawa, H.; Misawa, H.; Sakamoto, H.; Masuhara, M.; Sasaki, A.; Wakioka, T.; Ohtsuka, S.; Imaizumi, T.; Matsuda, T.; Ihle, J. N.; Yoshimura, A., The JAK-binding protein JAB inhibits Janus tyrosine kinase activity through binding in the activation loop. *The EMBO journal* **1999,** *18* (5), 1309-20.
237. Kubo, M.; Hanada, T.; Yoshimura, A., Suppressors of cytokine signaling and immunity. *Nat Immunol* **2003,** *4* (12), 1169-76.
238. Qian, Z.; Liu, T.; Liu, Y. Y.; Briesewitz, R.; Barrios, A. M.; Jhiang, S. M.; Pei, D., Efficient delivery of cyclic peptides into mammalian cells with short sequence motifs. *ACS chemical biology* **2013,** *8* (2), 423-31.
239. Roviello, G. N.; Musumeci, D.; Roviello, V., Cationic peptides as RNA compaction agents: a study on the polyA compaction activity of a linear alpha,epsilon-oligo-L-lysine. *International journal of pharmaceutics* **2015,** *485* (1-2), 244-8.
240. Xue, B.; Dunbrack, R. L.; Williams, R. W.; Dunker, A. K.; Uversky, V. N., PONDR-FIT: a meta-predictor of intrinsically disordered amino acids. *Biochim Biophys Acta* **2010,** *1804* (4), 996-1010.
241. La Manna, S.; Lopez-Sanz, L.; Leone, M.; Brandi, P.; Scognamiglio, P. L.; Morelli, G.; Novellino, E.; Gomez-Guerrero, C.; Marasco, D., Structure-activity studies of peptidomimetics based on kinase-inhibitory region of suppressors of cytokine signaling 1. *Biopolymers* **2017**.
242. Oliva, R.; Chino, M.; Pane, K.; Pistorio, V.; De Santis, A.; Pizzo, E.; D'Errico, G.; Pavone, V.; Lombardi, A.; Del Vecchio, P.; Notomista, E.; Nastri, F.; Petraccone, L., Exploring the role of unnatural amino acids in antimicrobial peptides. *Sci Rep* **2018,** *8* (1), 8888.
243. Kelley, L. A.; Gardner, S. P.; Sutcliffe, M. J., An automated approach for clustering an ensemble of NMR-derived protein structures into conformationally related subfamilies. *Protein Eng* **1996,** *9* (11), 1063-5.
244. Hilenski, L. L.; Clempus, R. E.; Quinn, M. T.; Lambeth, J. D.; Griendling, K. K., Distinct subcellular localizations of Nox1 and Nox4 in vascular smooth muscle cells. *Arterioscler Thromb Vasc Biol* **2004,** *24* (4), 677-83.
245. Yoshimura, A.; Naka, T.; Kubo, M., SOCS proteins, cytokine signalling and immune regulation. *Nat Rev Immunol* **2007,** *7* (6), 454-65.
246. Nozaki, Y.; Ri, J.; Sakai, K.; Niki, K.; Kinoshita, K.; Funauchi, M.; Matsumura, I., Inhibition of the IL-18 Receptor Signaling Pathway Ameliorates Disease in a Murine Model of Rheumatoid Arthritis. *Cells* **2019,** *9* (1).
247. Qin, M. Z.; Qin, M. B.; Liang, Z. H.; Tang, G. D., Effect of SOCS3 on lung injury in rats with severe acute pancreatitis through regulating JAK2/STAT3 signaling pathway. *European review for medical and pharmacological sciences* **2019,** *23* (22), 10123-10131.
248. Marin-Royo, G.; Rodriguez, C.; Le Pape, A.; Jurado-Lopez, R.; Luaces, M.; Antequera, A.; Martinez-Gonzalez, J.; Souza-Neto, F. V.; Nieto, M. L.; Martinez-Martinez, E.; Cachofeiro, V., The role of mitochondrial oxidative stress in the metabolic alterations in diet-induced obesity in rats. *FASEB journal : official publication of the Federation of American Societies for Experimental Biology* **2019,** *33* (11), 12060-12072.
249. He, C.; Yu, C. R.; Mattapallil, M. J.; Sun, L.; Larkin Iii, J.; Egwuagu, C. E., SOCS1 Mimetic Peptide Suppresses Chronic Intraocular Inflammatory Disease (Uveitis). *Mediators of inflammation* **2016,** *2016*, 2939370.
250. Hernandez, C.; Bogdanov, P.; Gomez-Guerrero, C.; Sampedro, J.; Sola-Adell, C.; Espejo, C.; Garcia-Ramirez, M.; Prieto, I.; Egido, J.; Simo, R., SOCS1-Derived Peptide Administered by Eye Drops Prevents Retinal Neuroinflammation and Vascular Leakage in Experimental Diabetes. *International journal of molecular sciences* **2019,** *20* (15).
251. Recio, C.; Oguiza, A.; Lazaro, I.; Mallavia, B.; Egido, J.; Gomez-Guerrero, C., Suppressor of cytokine signaling 1-derived peptide inhibits Janus kinase/signal transducers and activators of transcription pathway

and improves inflammation and atherosclerosis in diabetic mice. *Arteriosclerosis, thrombosis, and vascular biology* **2014,** *34* (9), 1953-60.
252. Russo, A.; Aiello, C.; Grieco, P.; Marasco, D., Targeting "Undruggable" Proteins: Design of Synthetic Cyclopeptides. *Curr Med Chem* **2016,** *23* (8), 748-62.
253. Bruzzoni-Giovanelli, H.; Alezra, V.; Wolff, N.; Dong, C. Z.; Tuffery, P.; Rebollo, A., Interfering peptides targeting protein-protein interactions: the next generation of drugs? *Drug Discov Today* **2018,** *23* (2), 272-285.
254. Lee, A. C.; Harris, J. L.; Khanna, K. K.; Hong, J. H., A Comprehensive Review on Current Advances in Peptide Drug Development and Design. *Int J Mol Sci* **2019,** *20* (10).
255. Chang, Y. S.; Graves, B.; Guerlavais, V.; Tovar, C.; Packman, K.; To, K. H.; Olson, K. A.; Kesavan, K.; Gangurde, P.; Mukherjee, A.; Baker, T.; Darlak, K.; Elkin, C.; Filipovic, Z.; Qureshi, F. Z.; Cai, H.; Berry, P.; Feyfant, E.; Shi, X. E.; Horstick, J.; Annis, D. A.; Manning, A. M.; Fotouhi, N.; Nash, H.; Vassilev, L. T.; Sawyer, T. K., Stapled alpha-helical peptide drug development: a potent dual inhibitor of MDM2 and MDMX for p53-dependent cancer therapy. *Proc Natl Acad Sci U S A* **2013,** *110* (36), E3445-54.
256. Lau, J. L.; Dunn, M. K., Therapeutic peptides: Historical perspectives, current development trends, and future directions. *Bioorg Med Chem* **2018,** *26* (10), 2700-2707.